THESIS

This is to certify that the

thesis entitled

LEPTONICALLY PRODUCED MULTIMUON FINAL STATES
IN MUON SCATTERING AT 270 GEV

presented by

Daniel Adams Bauer

has been accepted towards fulfillment
of the requirements for

Ph.D. degree in Physics

K W Chen

Major professor

Date 11-13-79

O-7639

LEPTONICALLY PRODUCED MULTIMUON FINAL STATES IN MUON SCATTERING AT 270 GEV

By

Daniel Adams Bauer

A DISSERTATION

Submitted to
Michigan State University
in partial fulfillment of the requirements
for the degree of

DOCTOR OF PHILOSOPHY

Department of Physics

1979

ABSTRACT

LEPTONICALLY PRODUCED MULTIMUON FINAL STATES

IN MUON SCATTERING AT 270 GEV

By

Daniel Adams Bauer

This dissertation summarizes the multimuon data of Fermilab experiment E319. In particular, a search has been made for possible heavy lepton signals and for other non-hadronic sources of muon-induced multimuon events. Conventional explanations for such events are also discussed.

The experiment employed 270 GeV tagged muons incident on a long iron-scintillator target/calorimeter which sampled the energy of the absorbed final-state hadrons. The scattered and produced muons propagated through a magnetic spectrometer made of toroidal iron magnets and wire spark chambers. Hodoscope counters and small-angle vetos formed the experimental triggers.

A new analysis program MULTIMU was developed to reconstruct muon tracks. This was used to filter the 8.2×10^5 triggers down to about 1.6×10^4 multimuon candidates. These events were visually scanned resulting in a true multimuon event sample of 449 dimuons and 64 trimuons. Detailed checks established finding efficiencies of (70 ± 8) percent for dimuons and (89 ± 8) percent for triumons giving

rates per deep-inelastic scatter of $(6.3 \pm 0.6) \times 10^{-4}$ dimuons and $(4.1 \pm 0.4) \times 10^{-5}$ trimuons, uncorrected for produced muon acceptance.

Monte Carlo methods were employed to model the most likely multimuon processes including associated charm production, π/k decay, hadronic final state interactions and QED tridents. Rate estimates from these calculations as well as general characteristics of the data implied that charmed meson production dominated the dimuon sample with small contributions from other hadronic sources. Histograms of produced muon kinematics for data and Monte Carlo were compared and hadronic model calculations subtracted. The resulting tiny signals appear in reasonable agreement with Monte Carlo calculations of QED tridents. Using kinematic cuts to supress both hadronic and electromagnetic processes leaves no statistically significant signal attributable to the weak production of heavy leptons. Upper limits derived from this process were consistent with the best published numbers. The much smaller trimuon sample was adequately explained by a roughly equal mixture of hadronic sources and trident production. A few very high transverse momentum produced muons remain unexplained.

ACKNOWLEDGMENTS

It is a pleasure to acknowledge the many people who have contributed to this work. All modern high energy physics experiments require the cooperative efforts of many physicists. Members of our small, but dedicated, collaboration included: Bob Ball, C. Chang, K. W. Chen, Mehdi Ghods, Jim Kiley, Adam Kotlewski, Larry Litt, and Phil Schewe from Michigan State University and A. Van Ginneken from Fermilab.

In addition to these physicists, the experiment relied on a whole host of additional people. During the design and construction phase of E319, the following people were essential: Dave Chapman, Frank Early, Mehdi Ghods, Sten Hansen, Ken Holtzmann, Bob Mills, and Ed Reyna. Furthermore, taking the data at Fermilab would have been much more difficult without the generous help of Sten Hansen and Kevin Beard. The assistance of the Fermilab staff, particularly from members of the Neutrino Department, was also vital.

In the data analysis phase, Larry Litt provided encouragement and assistance in track reconstruction. The multimuon search relied on the graphics software developed by Paul Bander and John Hoeckzema. Special appreciation is due the many patient scanners who actually found the multimuon events. My principal aides in this effort were: Mary Brake, Mary Beth Kazanski, and Bill Spero.

Two people provided much of the Monte Carlo code for E319. We used the basic methods and programs of Dr. A. Van Ginneken to calculate several processes in detail at M.S.U. Wai-Yee Keung from the University of Wisconsin checked many other multimuon processes with his own Monte Carlo. Both of them were very helpful in the interpretation of our data.

I have certainly benefitted from physics discussions with Professors Wayne Repko and Bill Francis at M.S.U. Other people who have contributed to my training in high energy physics are K. W. Chen, Dick Hartung, and Larry Litt. I would also like to thank the members of my guidance committee, especially Professors M. Abolins and J. Kovacs for their aid in the absence of Dr. Chen.

Finally, I must acknowledge the efforts and friendship of my fellow graduate students Bob Ball, Jim Kiley, and Phil Schewe. Discussions among Bob, Jim, and me sustained all of us through the long analysis. I also want to thank Bob and Phil for the use of several figures and tables.

Two special people played a prominent role in the preparation of this thesis. Dr. Mehdi Ghods, the able administrator of our NSF grant, provided invaluable assistance with good humor throughout the experiment. Mrs. Nancy Heath combined great patience with friendliness in the long struggle to type this thesis.

While many friends at M.S.U. contributed to my emotional well-being, two stand out as people to whom I will always be indebted. Jim Hylen, a fellow graduate student, was always willing to spend time

talki

the

parer

talking and to assist with anything. Karen Stricker was, and is, the person I could always count on to listen and to care.

Finally, I want to thank my family and, in particular, my parents to whom I owe the determination needed to achieve this goal.

TABLE OF CONTENTS

Table

LIST OF TABLES

Table

Figure

LIST OF FIGURES

Figure

TH

1.1 Introduction: and interactions

Physics can
order and simplicity
that all natural phe
frequently, though, t
and the limitations o
patterns. Careful ex
plify natural behavio
then employed to gene
The primary task (anc
properties in a large
classification into a
to other data or to a

Thus from the
particle physics, pat
of particles and forc
enduring, of such cla
particles into two gr
lighter particles) ar
properties between th

CHAPTER 1

THEORY AND EXPERIMENTAL BACKGROUND

1.1 Introduction: Particles and Interactions

Physics can be broadly defined as the search for underlying order and simplicity in nature. Physicists share a common belief that all natural phenomena can be explained by a few universal laws. Frequently, though, the sheer scale or complexity of such phenomena and the limitations of human senses combine to obscure underlying patterns. Careful experiments must be performed to isolate and simplify natural behavior, with insight, logic, and even speculation then employed to generalize the measured behavior to new regions. The primary task (and satisfaction) of a physicist is to recognize properties in a large and complex set of data that allow its classification into a few simple groups, which can be interrelated to other data or to already existing theories.

Thus from the early days of what is now called elementary particle physics, patterns have been sought in the growing number of particles and forces discovered. One of the first, and most enduring, of such classifications was the division of all known particles into two groups: leptons (consisting initially of the lighter particles) and hadrons. While there are many distinguishing properties between these two classes (e.g., spin and internal

structure), the mos
feel the strong (nu
ence remains even i
particles. There h
universe, or over v
but no concrete evi
many other symmetry
of the particle fam
useful in isolating

A similar t
mental forces goverr
forces were thought
charges and nuclear
among these phenomer
fundamental interact
weak force (responsi
(nuclear) force. In
theories combining e
electroweak interact
force and gravity ma
The mathematical bea
most compelling stin
further effort.

This dissert
involved in the proc
nucleon interactions

structure), the most fundamental distinction is that leptons never feel the strong (nuclear) force and hadrons always do. This difference remains even if it is postulated that hadrons are composite particles. There has been some recent speculation that in the early universe, or over very long time scales, some intermixing may occur, but no concrete evidence exists at present. Of course, there are many other symmetry properties which contribute to our understanding of the particle families, but the lepton/hadron split is particularly useful in isolating certain processes.

A similar trend has been followed in the study of the fundamental forces governing particle motion. Historically, many different forces were thought necessary to explain specific behaviors of masses, charges and nuclear dynamics. Recognition of the interrelationships among these phenomena has led to the current belief that only four fundamental interactions are needed: gravity, electromagnetism, the weak force (responsible for radioactive decays), and the strong (nuclear) force. In fact, the reduction continues still, with current theories combining electromagnetism and the weak force into a single electroweak interaction. It is even conceivable that the strong force and gravity may be eventually included within one framework. The mathematical beauty of such a unified field theory is itself a most compelling stimulus to both theorists and experimentalists for further effort.

This dissertation represents a study of the leptonic processes involved in the production of multimuon final states from muon-nucleon interactions. The data originated from a muon scattering

experiment E319, co
this work are (a) to
many current gauge t
magnetic multimuon p
theoretical predicti
The advantages of us
matic determination
easily recognizable
acceptance and event
E319 apparatus was n
remaining sections o
background for this
descriptions of the
rise to multimuons a
relative rates to ju

1.2 Background

The first tr
made its debut just
electron was also th
subsequent discovery
later.[2] No other ch
of matter and almost
the next lepton to be
confusion at the time
today. The muon bel

experiment E319, conducted at Fermilab in 1976. The primary goals of this work are (a) to search for possible heavy leptons predicted by many current gauge theories, and (b) to attempt to isolate electromagnetic multimuon production processes allowing comparison with theoretical predictions at higher energies than previously studied. The advantages of using inclusive muon scattering include good kinematic determination for all leptons, large incident energy, and an easily recognizable event signature. The disadvantages of low acceptance and event rates are due primarily to the fact that the E319 apparatus was not optimized for multimuon detection. In the remaining sections of this chapter, the theoretical and experimental background for this work will be discussed. I will present brief descriptions of the most likely specific processes which could give rise to multimuons and make order of magnitude estimates of their relative rates to justify the attempt to isolate leptonic processes.

1.2 Background

The first truly elementary particle discovered, the electron, made its debut just prior to the onset of the 20th century.[1] The electron was also the first and only lepton until the prediction and subsequent discovery of its antiparticle, the positron, thirty years later.[2] No other charged leptons are necessary to explain the nature of matter and almost all natural phenomena. Partly for that reason the next lepton to be discovered, now called the muon, caused great confusion at the time,[3] and indeed its raison d'etre is still a mystery today. The muon behaves exactly like a heavy electron, yet it

cannot decay into ar
to an almost ephemer
neutral(and probably
to conserve momentum
they can interact wi
experimentally disco
realized that each c
This sequential patt
to the lepton family
1974.[7] Since nobody
ence of leptons, the
massive additions to
suggest that nonseque
readily visible as mu
properties of the cur

The first hac
the electron and aga
nember, the neutron,
the electron, are sut
processes. However,
veritable explosion c
for ordinary matter.
this assortment of pa
themselves were not e
stituents came to be

cannot decay into an electron without transferring its "muonness" to an almost ephemeral particle, the neutrino. Neutrinos are neutral (and probably massless) leptons, originally invented by Pauli to conserve momentum in nuclear beta decay.[4] Due to the fact that they can interact with matter only via the weak force, they were not experimentally discovered until the 1950s.[5] Soon after it was realized that each charged lepton had its own special neutrino.[6] This sequential pattern appears to be preserved in the newest addition to the lepton family, the tau, which was discovered at SLAC in 1974.[7] Since nobody has yet uncovered the pattern behind the existence of leptons, there is no reason not to expect further, more massive additions to the family. Some recent gauge theories even suggest that nonsequential heavy leptons may exist which might be readily visible as multimuon events.[8] Table 1.1 summarizes the properties of the current lepton family.

The first hadron, the proton, was discovered shortly after the electron and again several decades followed before the next member, the neutron, was added. These two hadrons, together with the electron, are sufficient to describe virtually all atomic processes. However, unlike leptons, the next few decades saw a veritable explosion of new hadrons, most of which seemed unnecessary for ordinary matter. Gradually, however, patterns were detected in this assortment of particles which led to the notion that hadrons themselves were not elementary but composite particles whose constituents came to be called quarks or partons.[9] Although quarks

TABLE 1.1.--Leptons

Particle (Antiparticle)	Mas (Me
ν_e ($\bar{\nu}_e$)	0(<
e^- (e^+)	0.5
ν_μ ($\bar{\nu}_\mu$)	0 (<
μ^- (μ^+)	105.
ν_τ ($\bar{\nu}_\tau$)	0 (<
τ^- (τ^+)	17

TABLE 1.2.--Quarks an

Quark (Antiquark)	Lowes $J^P = 0^-$ (pseudos
u ($\bar{u}$)	} π^0(135
d ($\bar{d}$)	
s ($\bar{s}$)	η' (958)
c ($\bar{c}$)	η_c (?)
b ($\bar{b}$)	?
t ($\bar{t}$)	Not Ye

TABLE 1.1.--Leptons

Particle (Antiparticle)	Mass (Mev/c^2)	Decay width (MeV)	Predominant Decay Modes	Branching Ratios
ν_e ($\bar{\nu}_e$)	$0(<6\times10^{-5})$	Stable	--	--
e^- (e^+)	0.511	Stable	--	--
ν_μ ($\bar{\nu}_\mu$)	0 (< .57)	Stable	--	--
μ^- (μ^+)	105.659	3×10^{-16}	$\mu^- \rightarrow e^- \bar{\nu}_e \nu_\mu$	98.6%
ν_τ ($\bar{\nu}_\tau$)	0 (<250)	Not Yet Detected Experimentally		
τ^- (τ^+)	1782	$>2.8\times10^{-10}$	$\tau^- \rightarrow l^- \bar{\nu}_l \nu_\tau$	~36%
			$\rightarrow h^-$ neutrals	~33%
			$\rightarrow (\geq 3h^{\pm})$neutrals	~32%
			$l^- = e^-$ or μ^-	
			h = hadrons	

TABLE 1.2.--Quarks and Hadrons

Quark (Antiquark)	Lowest Lying Meson Bound States		Branching Ratios of vector meson to lepton pairs
	$J^P = 0^-$ (pseudoscalar)	$J^P = 1^-$ (vector)	
u ($\bar{u}$)	} $\pi^0(135)$, $\eta^0(549)$	} $\rho^0(770)$, $\omega^0(783)$	} ~.01%
d ($\bar{d}$)			
s ($\bar{s}$)	η' (958)	ϕ (1020)	~ .05%
c ($\bar{c}$)	η_c (?)	J/ψ (3100)	~ 14%
b ($\bar{b}$)	?	γ (9460)	~ 5%
t ($\bar{t}$)	Not Yet Detected Experimentally		

have never been see
proper combinations
quarks can account
Since their concept
experiments has beer
three quarks. Furth
experiments have dis
ence of at least two
carriers of the stro
there is no convinci
not be found and aga
signals. Table 1.2
family.

Because of t
phenomena have been
were usually treated
seemed to have no cor
century were all of t
electromagnetism.[12]
preceding this unific
actions have been des
electromagnetism, one
electromagnetic field
distribution of the r
theory, it became nec

have never been seen directly (and some believe they cannot be), proper combinations of just three kinds of quarks and their anti-quarks can account for all naturally-occurring hadronic matter.[10] Since their conception, much indirect evidence from scattering experiments has been found to support the existence of the original three quarks. Furthermore, recent electron-positron annihilation experiments have discovered new hadrons[11] which suggest the presence of at least two more quarks and the appearance of the actual carriers of the strong force, called gluons. As with leptons, there is no convincing reason to believe that heavier quarks will not be found and again these may produce characteristic multimuon signals. Table 1.2 describes the known constituents of the hadron family.

Because of their ubiquity in nature, electric and magnetic phenomena have been known to humans for centuries. However, these were usually treated as isolated, albeit useful, curiosities which seemed to have no connection with each other. Not until the 19th century were all of these phenomena united into a single theory of electromagnetism.[12] The rapid development of mathematical techniques preceding this unification supplied the form in which all interactions have been described since, namely the field theory.[13] For electromagnetism, one speaks of an interaction of a charge with the electromagnetic field, defined at all spacetime points by the charge distribution of the rest of the universe. With the advent of quantum theory, it became necessary to treat both forces and matter as "lumpy"

instead of continuo
interact via the ex
force, the photon,
strength of the int
niques and the famo
perturbative calcul
pleted the transform
to quantum electrody
all other field theo
have confirmed its v
24 orders of magnitu

In sharp con
phenomena, the very
discovery of nuclear
The first theoretica
by Fermi in the 1930
description of the b
magnetic leptonic in
ling constant for su
clear why this is ca
more potent electroma
worked reasonably we
failed badly for othe
times, a much more p
mathematical formali

instead of continuous. As visualized by Dirac,[14] discrete charges interact via the exchange of the carrier of the electromagnetic force, the photon, with coupling constant $\alpha \approx 1/137$ describing the strength of the interaction. The invention of calculational techniques and the famous Feynman diagrams, as well as proof that such perturbative calculations made sense for all orders essentially completed the transformation from classical Maxwellian electromagnetism to quantum electrodynamics (QED).[15] QED is still the prototype for all other field theories and by far the most successful. Experiments have confirmed its validity over spatial distances spanning at least 24 orders of magnitude.[16]

In sharp contrast to our familiarity with electromagnetic phenomena, the very existence of the weak force was unknown until the discovery of nuclear beta decay in the early part of this century.[17] The first theoretical understanding of such radioactivity was supplied by Fermi in the 1930s.[18] His approach was a purely phenomenological description of the beta decay dynamics, generalized to all nonelectromagnetic leptonic interactions (e.g., muon decay). Since the coupling constant for such processes was found to be about 10^{-5}, it is clear why this is called the weak interaction in comparison with the more potent electromagnetic and strong forces. The Fermi theory worked reasonably well for some weak processes at low energy, but failed badly for others and diverged at high energies.[19] In recent times, a much more promising approach has been found within the mathematical formalism of gauge theories,[20] somewhat similar to QED

in form, but with d
gauge groups seem t
forces into a singl
possible at all ene
have been built upo
dard version is tha
group SU(2) x U(1).
leptons to a left-ha
also having a right-
boson which carries
($W^{\pm}$ and Z^0) act as t
allows, in a natural
The coupling constan
experiment via the s
simplest electroweak
cated models exist w
leptons (i.e., massi
ing neutrino).[22] Thu
help reduce the numbe

Finally, ment
responsible for holdi
was discovered early
first performed.[23] A
overwhelms all others
strong interactions w

in form, but with different symmetries. The so-called non-Abelian gauge groups seem to be able to unite the weak and electromagnetic forces into a single electroweak interaction, with calculations possible at all energies for all processes. Although many models have been built upon these basic mathematical foundations, the standard version is that of Glashow, Weinberg, and Salam based on the group SU(2) x U(1).[21] This model assigns each sequential pair of leptons to a left-handed weak isospin doublet with the charged lepton also having a right-handed piece. Preserving the photon as the gauge boson which carries the electromagnetic force, three new bosons ($W^{\pm}$ and Z^{0}) act as the propagators of the weak interactions. This allows, in a natural way, both charged and neutral weak currents. The coupling constants and masses of this model can be related to experiment via the single parameter $\sin^2\theta_w$. Although this is the simplest electroweak theory consistent with experiment, more complicated models exist which require the existence of nonsequential heavy leptons (i.e., massive charged or neutral leptons with no corresponding neutrino).[22] Thus an experimental search for such particles may help reduce the number of contending models.

Finally, mention must be made of the strong force which is responsible for holding nuclei together. Like the weak force, it was discovered early in this century when nuclear experiments were first performed.[23] Although it is very short range, the strong force overwhelms all others within nuclear distances. Until very recently, strong interactions were discussed mostly in phenomenological terms,

using such ideas as

The explosion of ne

of accelerators, wh

stand strong intera

terns which appeare

try properties led

of quarks.[25] Subse

conception of "colo

colored gluons, with

ability to be affect

ture built on these

Although QCD calcula

have been made seem

lepton scattering an

culated in QCD is th

gluon fusion.[28] As

important hadronic s

Before pursu

cesses, it is useful

of this work. Lepto

tool in high energy

details the kinemati

nucleus simply to abs

reactions are no long

ies in higher energy

interactions can be a

using such ideas as virtual pion clouds or nuclear potentials.[24] The explosion of newly-discovered hadrons accompanying the advent of accelerators, while threatening to overwhelm any attempts to understand strong interactions, also provided important clues. The patterns which appeared when hadrons were grouped using certain symmetry properties led Gell-Mann and others to postulate the existence of quarks.[25] Subsequent theoretical work has led to our current conception of "colored" quarks bound together by the exchange of colored gluons, with color being the quantum number denoting the ability to be affected by the strong force. The gauge group structure built on these ideas is called quantum chromodynamics (QCD).[26] Although QCD calculations are quite complicated, the predictions which have been made seem to agree well with experimental results from lepton scattering and annihilation.[27] One process that has been calculated in QCD is the interaction of photons and gluons called photon-gluon fusion.[28] As we shall see later, this mechanism may be an important hadronic souce of multimuon events.

Before pursuing the description of specific multimuon processes, it is useful to briefly review the experimental background of this work. Lepton-nucleus scattering has long been a favorite tool in high energy physics for two types of tests. (Figure 1.1 details the kinematics of this process.) Firstly, by using the nucleus simply to absorb momentum, several interesting QED and weak reactions are no longer forbidden and shed new light on these theories in higher energy regimes. Perhaps more importantly, the leptonic interactions can be assumed to be understood and the virtual photon

θ = $\cos^{-1}[(\vec{p}_0 \cdot \vec{p}_1$

= polar angle of

$q^2 = 4E_0E_1 \sin^2(\theta/2)$

= 4-momentum trans

$\nu = E_0 - E_1$

= energy transfer

$x = q^2/2m_p\nu$

= Bjorken scaling

$y = \nu/E_0$

= fractional ener

$W = [2m_p\nu + M^2_p - q^2$

= center of momen

Figure 1.1.--Deep In

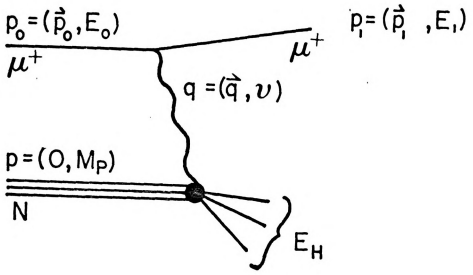

$\theta = \cos^{-1}[(\vec{p}_0 \cdot \vec{p}_1)/|\vec{p}_0|\,|\vec{p}_1|]$

= polar angle of scattered muon relative to incident muon

$q^2 = 4E_0E_1 \sin^2(\theta/2)$

= 4-momentum transfer to nucleus squared

$\nu = E_0 - E_1$

= energy transfer to nucleus squared

$x = q^2/2m_p\nu$

= Bjorken scaling variable

$y = \nu/E_0$

= fractional energy transfer

$W = [2m_p\nu + M^2_p - q^2]^{\frac{1}{2}}$

= center of momentum frame energy

Figure 1.1.--Deep Inelastic Scattering Kinematics

produced can be tr
of the nucleus, or
1950s an exhaustiv
began to detail nu
experiments now em
into the nucleus.

It was in
multimuon events w
diagram and releva
various event types
detectors were not
number of such ever
clear that the ever
pion decay. Specu
decay of either hea
provided the major
and analysis effort
and neutrino scatte

1.3 Specific Multi

Before proc
is necessary to exa
in some detail. Th
nates and some idea
which may allow le
those of hadronic c

produced can be treated as a probe of the electromagnetic structure of the nucleus, or even individual nucleons. Beginning in the late 1950s an exhaustive set of electron scattering experiments at SLAC began to detail nuclear structure.[29] At higher energies, most such experiments now employ muons and heavy targets to probe more deeply into the nucleus.

It was in such experiments at Fermilab that lepton-induced multimuon events were first detected.[30,31] (Figure 1.2 shows the Feynman diagram and relevant kinematic variables while Table 1.3 defines the various event types.) Unfortunately, the first generation detectors were not at all optimized to detect extra muons, and the number of such events was quite small. Even so, it quickly became clear that the events could not be from conventional sources such as pion decay. Speculation centered around the possible production and decay of either heavy quarks or heavy leptons. This uncertainty has provided the major impetus for increasing the detection efficiency and analysis effort for multimuons in the second generation of muon and neutrino scattering detectors, including those used for E319.

1.3 Specific Multimuon Processes

Before proceeding with a description of the experiment, it is necessary to examine the most likely sources of multimuon events in some detail. The aim is to obtain order of magnitude rate estimates and some idea of notable kinematic features, especially those which may allow leptonically produced events to be separated from those of hadronic origin. Detailed Monte Carlo calculations for

$\theta_i = \cos^{-1}[\hat{q} \cdot \vec{p}_i$
= polar angle
simply θ for

$p_{Ti} = E_i \sin\theta_i$
= transverse m
(p_L for dimu

$\Delta\theta_{ij} = \cos^{-1}[\hat{p}_i \cdot \vec{p}$
= polar angle

$\Delta\phi_{ij} = \phi_i - \phi_j$
= azimuthal an

$M_{ij} = 4E_iE_j \sin^2 (\Delta$
= apparent mass

$\eta = (E_o - \Sigma E_i)/E$
= inelasticity

$E_M = \eta E_o - E_H$
= missing energ

$a_{ij} = (E_i - E_j)/(E_i$
= asymmetry of

Figure 1.2.--Multim

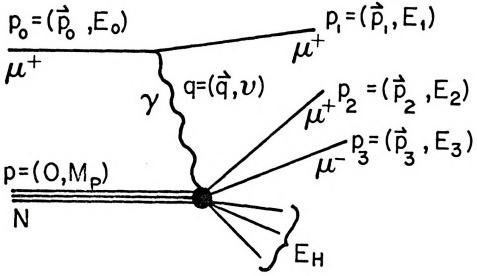

θ_i = $\cos^{-1}[\vec{q} \cdot \vec{p}_i)/|\vec{q}||\vec{p}_i|]$

= polar angle between virtual photon and ith muon (written as simply θ for dimuons where it refers to the produced muon)

$p_{\perp i}$ = $E_i \sin\theta_i$

= transverse momentum of ith muon relative to virtual photon ($p_\perp$ for dimuons where it refers to the produced muon)

$\Delta\theta_{ij}$ = $\cos^{-1}[\vec{p}_i \cdot \vec{p}_j)/|\vec{p}_i||\vec{p}_j|]$

= polar angle between ith and jth muons ($\Delta\theta$ for dimuon events).

$\Delta\phi_{ij}$ = $\phi_i - \phi_j$

= azimuthal angle between ith and jth muons ($\Delta\phi$ for dimuon events)

M_{ij} = $4E_iE_j \sin^2(\Delta\theta_{ij}/2)$

= apparent mass of the (i, j)th muon pair ($M_{\mu\mu}$ for dimuon events)

η = $(E_o - \Sigma_i E_i)/E_o$, i means final state muons

= inelasticity of the event

E_M = $\eta E_o - E_H$

= missing energy of the event

α_{ij} = $(E_i - E_j)/(E_i + E_j)$

= asymmetry of (i,j)th muon pair (α for dimuons)

Figure 1.2.--Multimuon Kinematics.

TABLE 1.3.--Multim

Type of Multimuon
1. Dimuon
a. Leading Particle
b. OSP
c. SSP
2. Trimuon
3. Exotic
4. Vertex
a. Hadronic
b. Leptonic

TABLE 1.3.--Multimuon Definitions

Type of Multimuon	E 319 Definition
1. Dimuon	Two muons detected downstream of the target
a. Leading Particle	For electromagnetic and hadronic processes, one of the muons must be the scattered muon. We define this as the one with highest energy and call it the leading particle
b. OSP	Opposite sign (charge) muon pair
c. SSP	Same Sign (charge) muon pair
2. Trimuon	Three muons detected downstream of the target
3. Exotic	Events with more than three muons detected
4. Vertex	The z (beam) position of the 1st calorimeter counter of a hadron shower or the z position where the muon tracks come closest to each other if no shower exists.
a. Hadronic	The calorimeter shower has at least 5 GeV
b. Leptonic	Less then 5 GeV deposited in the calorimeter

many of these proc

for the event rate

to be 50 1/pb per

The electr

muons, as shown in

(Bethe-Heitler tri

tridents), and cha

These fourth-order

diagrams without t

servation. Since

we immediately expe

to be reduced from

The process

more explicitly, l

coulomb field has b

However, the triple

cult to evaluate fo

sharply on kinemati

meaningless. Withi

experimental intere

evaluating the invo

We have utilized th

this process as wil

a qualitative under

referring to Figure

involve propagators

many of these processes are presented in Chapter 4. As a rough guide for the event rates that follow, we take the proposed E319 luminosity to be 50 1/pb per nucleon.

The electromagnetic processes which can give rise to multimuons, as shown in Figure 1.3, are muo-production of a muon pair (Bethe-Heitler tridents), photo-production of a muon pair (pseudo-tridents), and charged heavy lepton pair production and decay. These fourth-order processes are the lowest allowed because all diagrams without the nuclear vertex are forbidden by momentum conservation. Since deep-inelastic scattering is a second order process, we immediately expect multimuon rates from electromagnetic sources to be reduced from the single muon rates by α^2, or around 10^{-4}.

The process called Bethe-Heitler trident production, or more explicitly, leptoproduction of lepton pairs in the nuclear coulomb field has been theoretically understood for several decades.[32] However, the triple coincidence differential cross-section is difficult to evaluate for a given experiment because the result depends sharply on kinematic acceptance, making a straightforward integration meaningless. Within the last twenty years, renewed theoretical and experimental interest in tridents has stimulated novel methods for evaluating the involved trace sums with the aid of computers.[33] We have utilized these techniques in a Monte Carlo calculation of this process as will be seen in Chapter 4. However, one can get a qualitative understanding of the kinematics of these events by referring to Figure 1.4 and noticing that all of the trident diagrams involve propagators like $1/q^2$, $1/q_n^2$ for the photons, or $1/(p^2 + m^2)$

a. Bethe-Heitl

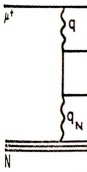

c. Heavy Lepton

Figure 1.3.--QED M

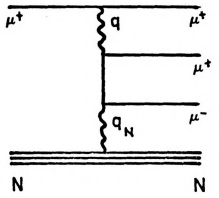

a. Bethe-Heitler Tridents

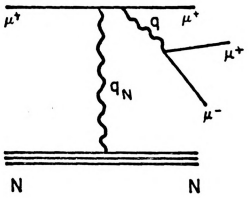

b. Bremsstrahlung/ Pair Prod.

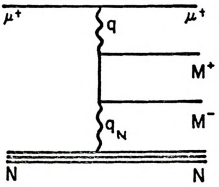

c. Heavy Lepton Pair Prod.

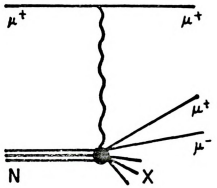

d. Deep Compton

Figure 1.3.--QED Multimuon Diagrams.

a. time-li

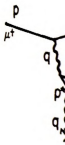

c. space-

Figure 1.4.--Contr
Calcu

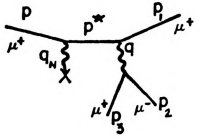

a. time-like

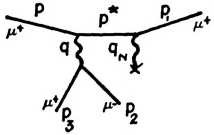

b. time-like

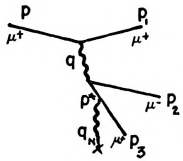

c. space-like

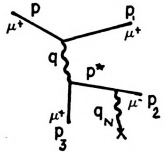

d. space-like

Figure 1.4.--Contributing Diagrams to Bethe-Heitler Trident Calculations.

for the excited mu
only when at least
nomentum transfers
at low angles will
realistic calculat
Carlo techniques.
sections[35] to the
of about 15 nb/nuc
apparatus, the acc
not to represent a
Although the situa
still not expected

The Feynma
pair production of
is essentially the
virtual photons is
transfer to zero ca
and therefore in ra
plying the bremsstr
(see Appendix C for
section at the aver
ence work of Tsai,[3
nucleon, leading to
Although this is do
rates, both are com
It may be that the

for the excited muon.[34] These imply that the cross section is large only when at least two of the leptons are nearly collinear (small momentum transfers). An experiment with poor acceptance for muons at low angles will have difficulty detecting these tridents and realistic calculations of the rates are impossible without Monte Carlo techniques. However, blind extrapolation of measured cross sections[35] to the E319 incident energy (270 GeV) gives a trimuon rate of about 15 nb/nucleon. In the previous experiment[36] with a similar apparatus, the acceptance losses were so large that tridents seemed not to represent a significant contribution to the event rate. Although the situation was somewhat improved for E319, tridents were still not expected to dominate.

The Feynman diagram for bremsstrahlung followed by photo-pair production of muons (sometimes called the pseudotrident process) is essentially the same as that for tridents, except that one of the virtual photons is now real. This restriction of one four-momentum transfer to zero causes a large reduction in available phase space and therefore in rate. A crude rate estimate can be made by multiplying the bremsstrahlung probability, estimated to be about 4×10^{-5} (see Appendix C for this calculation) by the pair production cross section at the average photon energy. Using the very complete reference work of Tsai,[37] the latter is calculated to be about 400nb/nucleon, leading to a raw trimuon event rate of around 20 pb/nucleon. Although this is down by three orders of magnitude from the trident rates, both are completely dominated by the experimental acceptance. It may be that the kinematics of pseudotridents are more favorable

than for tridents.

such as target bre

all thought to be

The same p

charged heavy lept

of these leptons w

dimuon or even trir

Tsai, the photo-pa

lepton are around

photoproduction us

$$\frac{7}{9}\frac{\alpha}{2\pi}\ln$$

with the resulting

further reduction f

doubtful that such

However, the striki

future, high-statis

Now let us

or intermediate vec

the weak processes

4th order electroma

involve particles w

charged heavy lepto

not in the standard

of masses and cross

literature that det

than for tridents. Note that other similar electromagnetic processes such as target bremsstrahlung and inelastic Compton scattering are all thought to be negligible compared to the trident mechanisms.[38]

The same processes described above can be used to produce charged heavy lepton pairs (e.g., $\tau^+\tau^-$). Occasionally, one or both of these leptons will decay into a muon (and neutrinos) leading to dimuon or even trimuon events. Again employing the calculations of Tsai, the photo-pair production cross sections for a 2 GeV heavy lepton are around 100 pb/nucleon. This can be converted to virtual photoproduction using the well-known factor[37]

$$\frac{7}{9}\frac{\alpha}{2\pi}\ln\frac{E^2}{m^2}$$

with the resulting event rate being about 1 pb/nucleon. Given the further reduction from low branching ratios and acceptance, it is doubtful that such heavy lepton signals could be detected in E319. However, the striking kinematic features of such events may enable future, high-statistics muon experiments to see them.

Now let us consider processes involving the weak interaction or intermediate vector bosons, as shown in Figure 1.5. Note that the weak processes are second order and thus comparable in rate to the 4th order electromagnetic processes. However, all of the weak diagrams involve particles whose existence is unproven. Neutral or doubly charged heavy leptons are required in some gauge theories, but not in the standard model. Unfortunately, there is such a range of masses and cross sections quoted for these processes in the literature that detailed calculations are difficult to perform

a).

b).

c)

Figure 1.5.--Multi
Lepto

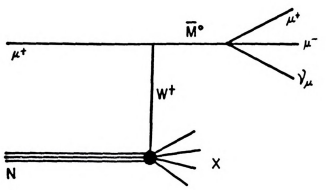

a). Heavy Neutral Muon Production and Decay

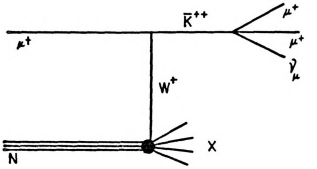

b). Hepton Production and Decay

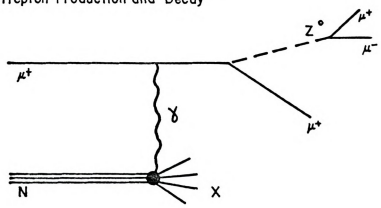

c). Weak Vector Boson Production

Figure 1.5.--Multimuon Diagrams Involving Production of Heavy Leptons or Weak Bosons.

at present. Inste
of multimuons proc
will be distinct f

A recent p
model independent
under various quar
(a) only opposite
around .1-.3 pb/nu
energies and angle
hadronic sources.
to see a few such
cuts is reserved f

Heptons, o
by Wilczek and Zee
electrons. Howeve
could give rise to
production cross se
ISR energies, assu
rates and kinematic
neutral heavy lepto

Finally, th
vector boson Z^0 ele
the cross sections
assuming M_Z = 5 GeV
However, other expe

at present. Instead, I have concentrated on the kinematic features of multimuons produced via these mechanisms, in the hope that they will be distinct from those seen in other processes.

A recent publication by Albright and Shrock[39] gives some model independent features of neutral heavy lepton production by muons under various quark couplings. Briefly, their conclusions are that (a) only opposite sign diumons can occur, (b) the raw rates are around .1-.3 pb/nucleon, and (c) several kinematic cuts on muon energies and angles can enhance this signal over electromagnetic and hadronic sources. While this rate is very low, it may be possible to see a few such events. A full discussion of the possible kinematic cuts is reserved for Chapter 5.

Heptons, or doubly charged heavy leptons, were first proposed by Wilczek and Zee[40] to allow rare radiative decays of muons into electrons. However, it is clear that the weak decay of these leptons could give rise to same-sign multimuons. A crude integration of their production cross section leads to a rate of about .2 pb/nucleon at E319 energies, assuming a 10% branching ratio. Clearly, both the rates and kinematic features are comparable with those from the neutral heavy lepton process.

Finally, there is the possibility of producing the intermediate vector boson Z^0 electromagnetically. Brown, et al.[41] have calculated the cross sections for this process with several boson masses. Assuming M_Z = 5 GeV, the rates for E319 would be about .3 pb/nucleon. However, other experiments have made it clear that the mass is much

larger and so the
small. No furthe
the related pair
For comple
hadronic sources
then out kinematic
The previous muon
isms were probably
As with the electr
have been calculat
be more thoroughly
If the sol
turned out to be t
events would have
of pion decay favo
shower energy, whi
observed distribut
rate short of Monta
contributed no more
experiment.[30]
The recomb
state can also lead
have attempted to e
hadron scattering
raw rates for E319

larger and so the cross sections for this process become negligibly small. No further effort need be made to calculate this process (or the related pair production of $W^{\pm}$).

For completeness, it is necessary to consider the "background" hadronic sources of multimuons in order to understand how to screen them out kinematically. Figure 1.6 shows the most likely processes. The previous muon experiment had suggested that some of these mechanisms were probably responsible for the majority of dimuon events. As with the electromagnetic processes, many of these hadronic sources have been calculated by Monte Carlo techniques and the results will be more thoroughly described in Chapter 4.

If the sole source of the second muon in dimuon events had turned out to be the decay of one of the shower pions (kaons), such events would have engendered little interest. However, the kinematics of pion decay favor very low transverse momentum and large hadron shower energy, which seemed to fit very poorly with the previously observed distributions.[30] There is no simple way to estimate this rate short of Monte Carlo calculations which suggested that this contributed no more than a third of the dimuons in the previous muon experiment.[30]

The recombination of soft quarks into muon pairs in the final state can also lead to dimuon or trimuon events. Several authors[38] have attempted to estimate the contribution of this process by using hadron scattering data and vector dominance arguments. The resulting raw rates for E319 have been estimated to be about 4 nb/nucleon.

a). π/K Dec

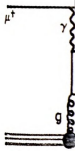

c). Associated

Figure 1.6.--Multi

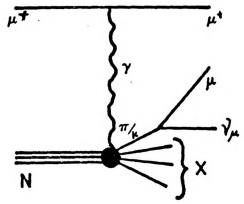

a). π/K Decay

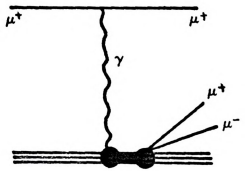

b). Quark Recombination

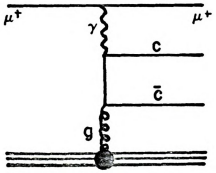

c). Associated Charm Prod.

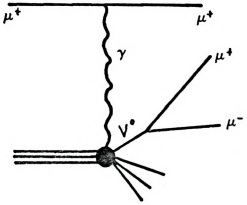

d). Vector Meson Prod.

Figure 1.6.--Multimuon Diagrams for Hadronic Processes.

However, again th
surely suffer dra

Another u
decays in time wi
Excellent vertex
low beam pion cont
happening.

One hadron
is vector meson pr
acceptance of this
low or high mass c
date. Muoproducti
for the Ψ giving a
1 pb/nucleon, assu
pair mass distribu
if this process co

Finally, t
associated product
dress as mesons and
Previous muon[43] and
production could ad
process may interfe
multimuons due to t
similar kinematic f
estimate for charme

However, again these events favor low transverse momentum and will surely suffer drastic acceptance losses.

Another uninteresting possibility may be that a beam pion decays in time with a scattered muon event, making an apparent dimuon. Excellent vertex resolution, good time resolution, and the inherently low beam pion contamination (5×10^{-5}) make this a very unlikely happening.

One hadronic process that has been studied in some detail is vector meson production. As will be obvious later, the mass acceptance of this experiment effectively prevents detection of either low or high mass objects, leaving only the Ψ as a potential candidate. Muoproduction cross section measurements have been published[42] for the Ψ giving a trimuon event rate at our energy of around 1 pb/nucleon, assuming a 7% branching ratio. Clearly, the apparent pair mass distributions for trimuon events will show a distinct peak if this process contributes significantly.

Finally, there is the very interesting process known as the associated production of heavy quarks (either charm or bottom), which dress as mesons and decay semi-leptonically to provide extra muons. Previous muon[43] and neutrino[44] experiments have claimed that charm production could account for the majority of their dimuon events. This process may interfere with the search for leptonically produced multimuons due to the relatively higher rate expected and somewhat similar kinematic features. A recent publication[38] gives a rate estimate for charmed quark associated production of 0.5 nb/nucleon and

for bottom quarks
lations have been
distributions to
samples, hopefull
electromagnetic o

Table 1.4
siderations discu
istics in mind th
the experimental
cedure (Chapter 3
lations in Chapte
and comparisons w
to isolate the le
tion and suggests
of the apparatus,
for the Appendices

for bottom quarks of about 1 pb/nucleon. Again Monte Carlo calculations have been made and I will rely on the resulting kinematic distributions to subtract such hadronic events from the multimuon samples, hopefully leaving those more likely to be of weak or electromagnetic origin.

Table 1.4 summarizes the rate estimates and kinematic considerations discussed in this chapter. Keeping these event characteristics in mind throughout, the next topics to be discussed will be the experimental apparatus (Chapter 2) and the data analysis procedure (Chapter 3). After presentation of the Monte Carlo calculations in Chapter 4, the data itself will be discussed in Chapter 5 and comparisons will be made with the calculations in the attempt to isolate the leptonic signals. Chapter 6 concludes the dissertation and suggests future improvements. Detailed treatment of parts of the apparatus, analysis, and theoretical calculations are reserved for the Appendices.

TABLE 1.4.--Multi

Process	B (e p
Bethe-Heitler Muon Tridents	~ (~
Pseudo-Tridents	1 (3
$\tau^+ \tau^-$ pair production	0. (3
Deep Compton Scattering	~ (~
Neutral Heavy Lepton	≤ 0 (3
Doubly-Charged Heavy Lepton	≤ 0 (3
Weak Bosons (Assume M = 5GeV)	.0 (1
Assoc. Charmed Mesons	~ ~
η_c Decay	
λ/λ_0 production	~ ~
Soft Hadron Recombinations	~ (~
Upsilon Production	≤ (~

TABLE 1.4.--Multimuon Rate Estimates

Process	$B\sigma$ (per nucleon) (event rate with perfect acceptance)	Characteristics
Bethe-Heitler Muon Tridents	~15000 pb (~4×10^5 trimuons)	Mostly at very small angles, drastic acceptance reduction expected
Pseudo-Tridents	10-30 pb (300-800 trimuons)	Also at low angles, but not so much
$\tau^+ \tau^-$ pair production	0.1 → 1.0 pb (3-30 dimuons)	Should give large apparent masses, transverse momenta and missing energies.
Deep Compton Scattering	~1.5 pb (~40 trimuons)	Look like tridents, but at a negligible rate
Neutral Heavy Lepton	≤ 0.1 - 0.3 pb (3-8 OSPs)	Only OSPs produced. Expect large $p_\perp$ and missing energy $E_1/E_2 \approx 1$
Doubly-Charged Heavy Lepton	≤ 0.1 - 0.3 pb (3-8 SSPs)	Only SSPs. Otherwise similar to neutral lepton characteristics
Weak Bosons (Assume M = 5GeV)	.03 - .3 pb (1-8 dimuons)	Actually expect much larger weak boson masses making rates infinitesimal
Assoc. Charmed Mesons	~500 pb (~1400 dimuons)	Dominant dimuon hadronic process. Produces large apparent masses, transverse momenta and missing energies
π/κ Decay	--	Mostly at low masses and transverse momenta.
J/ψ production	~.85 pb (~24 trimuons)	Should give obvious mass peak as signature.
Soft Hadron Recombinations	~4000 pb (~1×10^5 dimuons)	Similar to π/k results except expect lower rate
Upsilon production	≤ 1 pb (~30 trimuons)	Again mass peak expected. Acceptance probably too small to see this.

2.1 Overview of

The purpo

tape sufficient s

matics of muon sc

within a large ra

be divided into s

provided target n

deposited in the

detect beam and s

chambers which me

magnetic spectrom

used to determine

ics to record det

write the results

which supply the

Much of th

was constructed f

and has been fully

only how this equi

plete description

CHAPTER 2

EXPERIMENTAL APPARATUS

2.1 Overview of the Apparatus

The purpose of the E319 apparatus was to record on magnetic tape sufficient spatial and timing information so that the kinematics of muon scattering events could be completely reconstructed within a large range of energy and polar angle. The equipment can be divided into six types: (1) the hadron sampling calorimeter which provided target nucleons and measured the hadron shower energy deposited in the interaction; (2) scintillation counters used to detect beam and scattered muons and reject halo; (3) proportional chambers which measure the incident muon momentum vector; (4) a magnetic spectrometer with toroidal magnets and wire spark chambers used to determine the kinematics of final state muons; (5) electronics to record detector information, make fast trigger decisions and write the results on tape; and (6) the accelerator and muon beam which supply the incident muons.

Much of this equipment (3, 4, and parts of 2 and 5 above) was constructed for use in the first generation muon experiment E26 and has been fully described in several theses.[1] I will discuss only how this equipment was tested and used for E319. A more complete description of construction and operation is necessary for the

rest of the appar
feature of this e
but full detail i
overview of the E

2.2 The Calorime

The hadron
elements) of mach
nucleons) sandwic
the passage of ch
hadron showers.
of sampling calor
use in cosmic ray
that when a charge
iron nucleus), one
kaons) are produce
then interact agai
resulting shower l
and nuclear absorp
charged particles
the total energy i
hadrons has previo
light proportional
then which is, in
ionizing charged p
converted into elec

rest of the apparatus. The calorimeter, which was the major new feature of this experiment, will be summarized in the next section, but full detail is reserved for Appendix A. Figure 2.1 shows an overview of the E319 apparatus.

2.2 The Calorimeter

The hadron calorimeter consisted of a long sequence (110 elements) of machined steel plates (which supply most of the target nucleons) sandwiched with plastic scintillation counters to measure the passage of charged particles and thus the energy deposited in hadron showers. The theory, design principles, and actual operation of sampling calorimeters have been adequately established by their use in cosmic ray and neutrino experiments.[2] The essential point is that when a charged particle scatters off a nucleon (or the whole iron nucleus), one or more high energy hadrons (mostly pions and kaons) are produced in the re-combination of quarks. These hadrons then interact again producing more hadrons and electrons. The resulting shower length is a complex function of both the radiation and nuclear absorption lengths of iron. By sampling the number of charged particles at frequent intervals, one obtains a measure of the total energy in the shower if the response to mono-energetic hadrons has previously been determined. The scintillators produce light proportional to the amount of radiation energy deposited in them which is, in turn, proportional to the number of minimum-ionizing charged particles which have passed through. The light is converted into electrical signals by photomultiplier tubes. The


WSC →
9
8
M1
7
M2
6
M3 M4
5
M5 M6
4
M7 M8
3
2
1

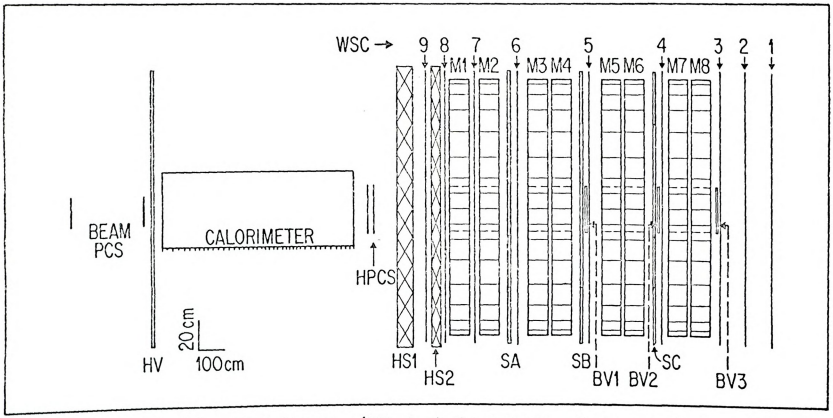

Figure 2.1.--E319 Experimental Apparatus. (PCS stands for proportional chambers; HV is the halo-veto hodoscope; HS means hadron shields; WSC refers to wire spark chambers; M stands for magnets; SA, SB, and SC are the trigger hodoscopes; and BV refers to beam veto counters).

signals are then
analog-to-digital
proportional to t
non-linearities we
calorimeter was ha
target, gain shift
cal interference (
chamber noise. Al
resolved, although
data taking. The
tool for establish
muons before and a
obtained with the h
with spectrometer e
level. Exhaustive
provided in Appendi

2.3 E319 Counters

Several diffe
E319. Signals obta
hodoscopes (BH) sup
was defined by two
the target hodoscope
ing of the beam at t
target, the halo-vet
taining "live" (i.e.

signals are then amplified and finally converted into digital form by analog-to-digital converters (ADCs). The resulting numbers will be proportional to the number of particles in each counter assuming all non-linearities were corrected in calibration. Actual use of the calorimeter was hampered by non-containment of the shower in the target, gain shifts at any stage of the counter system, and electrical interference (especially with the sensitive ADCs) due to spark chamber noise. All of these problems were at least partially resolved, although the noise effects occurred through most of the data taking. The calorimeter has proven to be a very successful tool for establishing event vertices and determining the number of muons before and after the interaction. Moderate success has been obtained with the hadron energy measurement although discrepancies with spectrometer energy determination persist at the few percent level. Exhaustive detail on all aspects of the E319 calorimeter is provided in Appendix A.

2.3 E319 Counters

Several different scintillation counter systems were used in E319. Signals obtained from the upstream experiment (E98)[3] beam hodoscopes (BH) supplied beam momentum information. Beam location was defined by two sets of three counters each, labeled B and C, while the target hodoscope (TH) defined the spatial distribution and timing of the beam at the front of the target. Also, upstream of the target, the halo-veto (HV) bank of counters rejected triggers containing "live" (i.e., within 25ns of a beam signal) particles

outside of the be

counters placed w

of the spark cham

record of timing

covered the toroi

triggers with a "

counters provided

All scintil

light, produced by

scintillator, is p

face of a photomul

trons are focused

electrons produced

charge, producing

was "hit." Each s

foil and black pla

tube from light.

high voltage is co

bases) and a plate

until the counter

to have passed thr

by the type of phot

uniformity of respo

useful only for ver

The actual construc

outside of the beam radius defined by B and C. Trigger bank (TBC) counters placed within the spectrometer allowed flexible triggering of the spark chambers for desired event types and also provided a record of timing for final-state muons. Beam veto (BV) counters covered the toroidal holes near the back of the spectrometer to reject triggers with a "live" unscattered muon. Several miscellaneous counters provided efficiency checks and calibration beam definition.

All scintillator counters work on the same basic principles: light, produced by the passage of a charged particle in the plastic scintillator, is piped by internal reflection to a cathode at the face of a photomultiplier tube where it ejects electrons. The electrons are focused and accelerated down a chain of dynodes with more electrons produced at each successive step. The anode collects the charge, producing an electronic pulse signalling that the counter was "hit." Each such counter must be carefully wrapped in aluminum foil and black plastic or tape to shield the scintillator and phototube from light. After insuring that the counter is light-tight, high voltage is connected to the phototube (via resistor chain tube bases) and a plateau curve is taken, (i.e., the voltage increased until the counter sees with excellent efficiency a cosmic ray known to have passed through it.) The plateau voltage is mostly determined by the type of phototube used. Finally, if desired, the spatial uniformity of response can be mapped out by the same method. This is useful only for very large counters where light piping is difficult. The actual construction of our counters follows the general procedure

described in App

the function of

for all E319 cou

There wer

(two upstream and

bank consisted of

in the y (bend) d

scopes allows bea

basis, their overa

our events with u

only in the final

properly timed (se

The three

the last beam line

inherently sensiti

required for these

counters were not

which gave output

for such small cou

(one at the front

tus) constituting

arm of B and C thus

The C counters were

fairly low noise le

array of eight over

described in Appendix A for the calorimeter. I shall concentrate on the function of the counter systems here. A summary of the parameters for all E319 counters is given in Table 2.1.

There were three E98 beam hodoscopes available for our use (two upstream and one downstream of the last beamline dipole). Each bank consisted of eight 0.75" wide counters, arranged with no overlap in the y (bend) direction. Although the granularity of these hodoscopes allows beam energy determination of ~ 1% on an event-by-event basis, their overall efficiency was somewhat low, leaving 10-15% of our events with undetermined beam energy. This problem was corrected only in the final data runs when the E98 proportional chambers were properly timed (see 2.4).

The three small rectangular B counters were situated within the last beam line magnets to define the beam. Since phototubes are inherently sensitive to magnetic fields, thick iron shields were required for these counters. Due to their inaccessibility, the B counters were not separately plateaued but simply set at voltages which gave output signals at levels known to represent high efficiency for such small counters. There were also three circular C counters (one at the front of the lab and two at the front of the E319 apparatus) constituting the other half of beam definition. The long lever arm of B and C thus selects muons near the center of the beam line. The C counters were plateaued and showed efficiences > 99% with fairly low noise levels. The target hodoscope was a 2-dimensional array of eight overlapping rectangular counters designed to cover

TABLE 2.1.--E319 Counter Systems

Symbol	Function	Number	Area	Phototube	Experiment	Location
BH	Determine beam momentum	3 banks 8 per	3/4" wide except 1" on east edge	Amperex 56AVP	E98, E398	Beam Enclosures 103, 104
B	Beam definition within magnet	3 bank	3 1/2" horiz. 2 1/2" vert. 1/4" thick	Amperex 56AVP	E26	Beam Enclosure 104

TABLE 2.1.--E319 Counter Systems

Symbol	Function	Number	Area	Phototube	Experiment	Location
BH	Determine beam momentum	3 banks 8 per bank	3/4" wide except 1" on east edge	Amperex 56AVP	E98, E398	Beam Enclosures 103, 104
B	Beam definition within magnet apertures	3	3 1/2" horiz. 2 1/2" vert. 1/4" thick	Amperex 56AVP	E26	Beam Enclosure 104
C	Beam definition in muon lab	3	7 1/2" diam. 1/4" thick	Amperex 56AVP	E26	C1-Front of Lab C2, C3--Target front
TH	Multiple beam separation	8	7 1/2" long by 2" wide by 3/8" thick	Amperex 56AVP	E319	Front of target
HV	Veto events with live non-beam muons	7	Similar to TBC except hole diam. 7"	Amperex 56AVP	E26, E319	Front of target
Calori-meter	Hadron shower measurements	110	20" x 20" x 3/8"	RCA 6342A	E319	Target
TBC	Triggering on scattered muons	3 banks 12 per bank	See Fig. 2.2	Amperex 56AVP	E26, E319	Spectrometer
BV	Veto events with low angle muons	3	12.5" diam. 3/8" thick	Amperex 56AVP	E319	Spectrometer
Tele-scope	Efficiency monitors for TBCS, WSCS	4	8" x 8" x 1/4"	RCA 7850	E26	HVTEL on HV bank STEL on TBCS
Misc.	Telescopes and Plateauing	Several	Small (typically 1" by 4")	RCA 6655A and others	E26, E319	Around target

the area of the C
between beam muon
that this turned
have been ignored

The halo-
outside of the C
counters. This i
quite broad with
bank, a leftover
phototubes attache
special (56AVP) ph
cal OR of all 14 c
very high and very
and accidental vet
falling to ~90% ne

Three sets
middle of the E319
counters stacked i
counters in the Y
counter of each se
magnet toroids and
to the size of the
only on muons scat
requirement is disc
of the TBC's was t

the area of the C counters. The object was to be able to distinguish between beam muons if more than one were detected in an event. Note that this turned out to be rare (< 2% of the events) and these events have been ignored in most of the analysis.

The halo-veto bank rejects potential triggers if a muon passes outside of the C counters within ~20ns of the muon inside the C counters. This is necessary because the FNAL muon beam (see. 2.7) was quite broad with "halo" muons often outnumbering "beam" muons. This bank, a leftover from E26, was in poor condition with very noisy phototubes attached. To increase the efficiency and reduce the noise, special (56AVP) phototubes were mounted. Furthermore, since the logical OR of all 14 counters supplied the veto signal, the rates were very high and very fast electronics was needed to prevent dead time and accidental vetoing. The efficiency of this bank averaged > 98%, falling to ~90% near some of the edges.

Three sets of trigger banks were situated roughly in the middle of the E319 spectrometer. Each consisted of five (E26) counters stacked in the X (vertical) direction and five (E319) counters in the Y (horizontal) direction (Figure 2.2). The middle counter of each set left a hole slightly bigger than that in the magnet toroids and the overall dimensions of the banks corresponded to the size of these toroids since we wanted to trigger the apparatus only on muons scattered into the magnetic field (the triggering requirement is discussed in Section 2.6). Although the main function of the TBC's was triggering, the hits in each counter were recorded

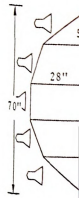

Figure 2.2.--Trigg
were
banks
the s

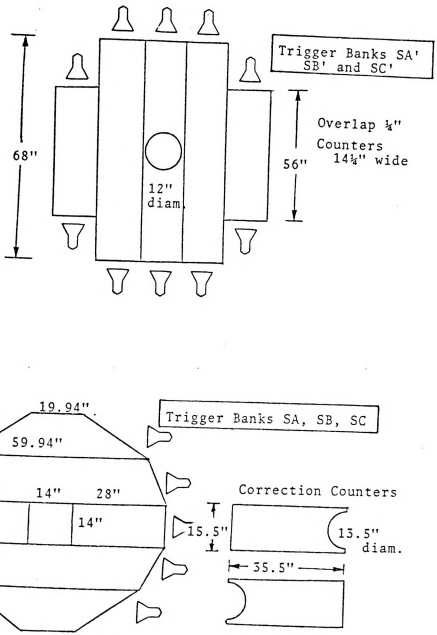

Figure 2.2.--Trigger Hodoscope Counters. (The old (unprimed) banks were positioned slightly upstream of the new (primed) banks and the correction counters were used to convert the square holes to round ones on the old banks).

for each event, a

tion on all muon

able in light of

counters from t

operated during

were especially

flexibility and

similar to those

gest problem bein

counters in a ver

56AVP phototubes

bases and cables

were three circul

than the magnet h

centered visually

preventing any of

from triggering th

events to be reco

crucial and each

rate-dependent eff

ics dead-time) wer

muons/spill.

3.4 Proportional

Proportion

due to their well-

for each event, and this provided timing and crude position information on all muons within the spectrometer (which is especially valuable in light of the long memory time of spark chambers). The counters from the previous experiment were simply plateaued and operated during E319 with efficiencies all > 95%. The E319 TBCs were especially built for this experiment to provide greater trigger flexibility and redundancy. The construction techniques were very similar to those used for the calorimeter (Appendix A) with the biggest problem being support of the very large and somewhat fragile counters in a vertical position. Note that all of the TBCs used 56AVP phototubes on both ends to insure high efficiency (the tube bases and cables were largely built by the E319 group also). There were three circular beam-veto counters (diameter slightly bigger than the magnet holes) mounted near the back of the spectrometer and centered visually on the magnets. These have the difficult task of preventing any of the enormous number ($\sim 10^5$) of unscattered muons from triggering the apparatus so as to allow mostly deep-inelastic events to be recorded. Thus, the efficiency of these counters is crucial and each was plateaued to > 99.5% efficiency. Furthermore, rate-dependent effects (e.g., tube base voltage sagging or electronics dead-time) were carefully eliminated up to intensities of 10^6 muons/spill.

2.4 Proportional Chambers

Proportional chambers were used for beam measurement in E319 due to their well-known high rate capacity and short memory time. The

principle of ope
charged particle
large (several k
and a set of clo
the wires. When
gas further, lea
of negative char
in the electric
charges even reac
"proportional" to
particle within
the particle mass
problem is to des
gas mixture and v
caused by photons
ing dead times of
pulses on the wir
tor level, are al
electronics for th
resolution of arou
tional chambers us
experiments (E98 a
able in several th
minor repairs, wer
responded and then

principle of operation is relatively simple:[4] the passage of a charged particle in a gas produces ion pairs. Application of a large (several kV) potential difference between a high-voltage plane and a set of closely spaced wires causes the ions to drift toward the wires. When they gain enough energy, they begin to ionize the gas further, leading to the formation of an avalanche. The movement of negative charges toward, and positive charges away from, the wires in the electric field induces a current flow in them (before the charges even reach the wires). The size of the resulting pulse is "proportional" to the amount of ionization produced by the passing particle within limits (which in turn depend in a known manner on the particle mass, energy, and properties of the gas). The crucial problem is to design the geometry and use an appropriate "magic" gas mixture and voltage such that breakdown (sparks and streamers caused by photons emitted from the ionized gas) is prevented, insuring dead times of less than 200ns and high-rate capacities. The pulses on the wires are amplified and, if above a pre-set discriminator level, are allowed to set latches (Figures 2.3 and 2.4 show this electronics for the E319 PCS). This gives position information with resolution of around one wire spacing (1-2mm). Both sets of proportional chambers used for E319 were built and operated in the previous experiments (E98 and E26) with construction and test details available in several theses.[1,3] For our experiment, the chambers, after minor repairs, were tested in the beam to make sure all wires responded and then used in the same manner as in the old experiments.


1/4 MC1030
1+5+9+13
2+5+9+12
3+4+10+11
4.3K
CHARPAK DISCRIMINATOR
MC1035

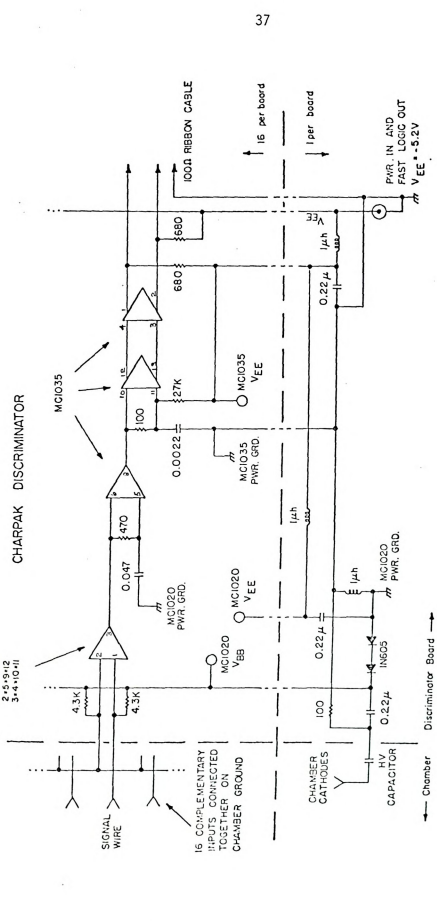

Figure 2.3.--Discriminator Electronics for E319 Proportional Chambers.


100 R RIBBON CABLE
CHANNEL N (N-16)
I/4 MC1020
I/4 MC1089
I/4 SN7408
CAMAC
BUS
ENABLE FIRST CONVERSION
RESET
ENABLE WRITE
FROM CHANNEL N+1
110
0001
430

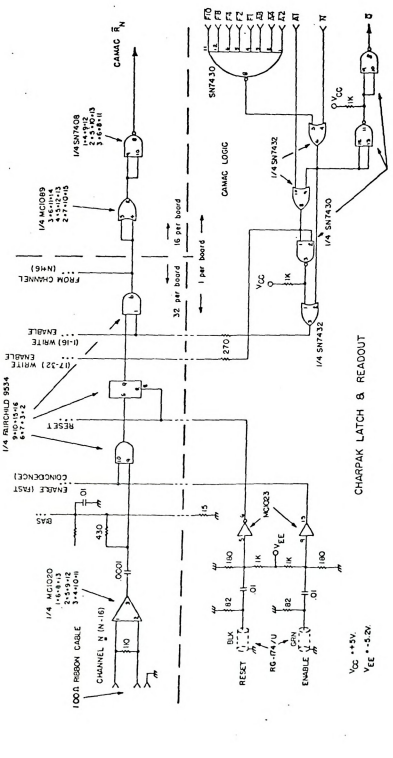

Figure 2.4.--Latch and Readout Electronics for E319 Proportional Chambers.

Of the s

which measured t

momentum). We s

mitting and reco

Unfortunately, t

had to be jury-r

improper timing

not discovered u

of these chamber

much of the data

correct and the c

hodoscope method

measure of the be

The E319

versity,consisted

(hadron) modules.

at 60° relative t

C counters in the

spatial resolutio

hadron chambers e

modules were at a

state muons prompt

lution and to supp

proportional chamb

the chambers are r

Of the six available E98 PC planes, we used only the four which measured the bend direction of the beam (and thus the beam momentum). We supplied the ribbon cable and latches needed for transmitting and recording the signals for the wires of each plane. Unfortunately, the signals were incompatible with the latches, which had to be jury-rigged to work properly. A further problem, involving improper timing of the signal arrival relative to the latch gate, was not discovered until the last set of data runs and has prevented use of these chambers for event-by-event beam momentum determination on much of the data. However, the average distribution was still correct and the chambers have provided a valuable check on the beam hodoscope method of finding beam momentum, as well as a finer-grained measure of the beam spread.

The E319 proportional chambers, on loan from Cornell University, consisted of three small (beam) chambers and two larger (hadron) modules. The beam chambers each had three planes oriented at 60° relative to each other and occupied the same positions as the C counters in the Muon lab. Their function was to record, with good spatial resolution, the passage of the triggering beam muon. The hadron chambers each had two planes at right angles, and the two modules were at a 45° angle. The idea here was to detect the final state muons promptly after leaving the target to improve vertex resolution and to supply good timing information (the memory time of the proportional chambers is ~100ns). Two problems with this were that the chambers are not quite wide enough to cover the calorimeter area

and, occasional

saturates the w

chambers were p

97-99%, with pro

wires. The para

found in Table 2

2.5 The Magneti

The purp

to measure the k

target. The mag

provided by eigh

of ~17 kG. Actua

spark chambers in

the correct signa

large steel slabs

chambers from had

aided by the pres

holes to prevent

muons. The spect

the same as that

for E319. Again,

of these devices

spectrometer was

Toroidal

concentrating max

and, occasionally, the hadron shower "leaks" from the target and saturates the wires of the hadron chambers. The E319 proportional chambers were plateaued (just like counters) at efficiencies of 97-99%, with problems coming mostly from a few dead or oscillating wires. The parameters of both sets of proportional chambers can be found in Table 2.2.

2.5 The Magnetic Spectrometer

The purpose of the magnetic spectrometer used in E319 was to measure the kinematics of all final-state muons coming from the target. The magnetic field needed for momentum determination was provided by eight steel toroidal-shaped magnets with average fields of ~17 kG. Actual particle detection was accomplished by nine wire-spark chambers interleaved with the magnets, and triggered only when the correct signal is obtained from the counter electronics. Two large steel slabs at the front of the spectrometer shield the spark chambers from hadrons spilling out of the target. This was also aided by the presence of the iron magnets (with concrete plugs in the holes to prevent hadron punch-through) since we wanted to detect only muons. The spectrometer was, with the exception of the hadron shields, the same as that used in E26, although more magnets were energized for E319. Again, I will refer detail of the construction and testing of these devices to theses from E26[1] and describe only how the spectrometer was used in E319.

Toroidal magnets represent an inexpensive and compact way of concentrating maximum magnetic field over a relatively small region

TABLE 2.2.--Proportional Chambers

Parameter	E319 Chambers			E98 Chambers
	PC5	PC3, 4	HPCS	

TABLE 2.2.--Proportional Chambers

Parameter	E319 Chambers			E98 Chambers
	PC5	PC3, 4	HPCS	
No. Chambers	1	2	2	6
Views/Chamber	2 (x,y)	3 (u,v,w)	2 (x,y or u,v)	1 (4y, 2x)
Wires/View	96	160	192	96
Wire Spacing	2 mm	2 mm	2mm	2.12 mm
Wire Type	20 micron ——	Gold Plated ——	Tungsten ——	?
Gas	20% Isobutane + .3% 13B1 Freon +	3.9% Methylal Balance Argon	——	75% Argon, 25% CO_2 .5% 13B1 Freon
Voltages	- 4200V ——→	-5000 V ——		-3200← -3500V
Location	Front of muon lab	Front of Target	End of Target	Beam enclosures 103, 104, μlab

to produce measu
disadvantage is
scattering and e
only muons will
tected (as oppos
can detect final-
slabs of low-carb
to allow for wate
flowed when the m
provided notice o
the magnets were m
tracks to allow e

Since iro
(hysteresis), the
taken. This was
slowly reducing th
eral hours. Witho
the field shape (w
since there was in
their very detaile
obtained for E319
performed by windi
measuring the curr
capacitor $Q = \int I dt$
(changing the magn

to produce measurable bending for high energy muons. Their primary disadvantage is the limit on momentum resolution due to multiple scattering and energy loss within the iron and the fact that, since only muons will penetrate, all other final state particles are undetected (as opposed to E98 with an air-gap magnet and LH_2 target which can detect final-state hadrons). The toroids consisted of welded slabs of low-carbon steel wrapped radially with hollow copper wire to allow for water cooling since currents of ~35 A continuously flowed when the magnets were on. Temperature monitors on each coil provided notice of overheating. As with all spectrometer elements, the magnets were mounted on Thompson bearings which rode on railroad tracks to allow easy mobility if desired.

Since iron can retain very complex magnetization patterns (hysteresis), the magnets were de-gaussed before any muon data was taken. This was accomplished by alternating the direction (and slowly reducing the amount) of current flow in many steps over several hours. Without doing this, we would have had no assurance that the field shape (when the magnets were on) was the same as in E26, since there was insufficient time and manpower available to repeat their very detailed studies of the field.[1] The average field was obtained for E319 currents by flux loop measurements. These were performed by winding a single coil of wire around a magnet and measuring the current (or better, the total charge on an integrating capacitor $Q = \int I dt$) induced by varying the magnetic field by ΔB (changing the magnet current). By Faraday's law we expect

RQ = $\Delta\phi$ = $A\Delta B$,
tance in the mea
the capacitor C

$$V = Q/C$$

So, if the field
ing V gives

$$B_o = \frac{RCV}{A}$$

The result of th
E26 for similar c
dependence should

Spark cha
outgrowth of Geig
principles are st
a noble gas mixtu
pairs. A properl
of the chamber ca
pairs producing a
from recombinatio
the channel. Ear
the position of t
to rapid computer
wires inside the
position. The di

$RQ = \Delta\phi = A\Delta B$, where A = area of the wire loop, and R is the resistance in the measuring circuit. The voltage which appears across the capacitor C is then

$$V = Q/C = \Delta BA/RC$$

So, if the field is varied from 0 up to its normal value B_o, measuring V gives

$$B_o = \frac{RCV}{A}$$

The result of this for E319 agreed closely with the measurements of E26 for similar currents, giving us confidence that the radial dependence should also be the same. Table 2.3 summarizes the toroids.

Spark chambers, invented in the late 1950's, were a natural outgrowth of Geiger and proportional counter techniques. The working principles are straightforward:[5] passage of the charged particle in a noble gas mixture (standard 90% Neon, 10% Helium) creates ion pairs. A properly shaped high voltage pulse applied between plates of the chamber causes rapid propagation and further creation of pairs producing a conducting ion channel. Aided by photons emitted from recombination of the ionized gas, a spark discharge occurs in the channel. Early spark chambers used photographic means to record the position of the sparks, but this is cumbersome and not amenable to rapid computer analysis. Placing a plane of closely-spaced fine wires inside the chamber allows electronic detection of the spark position. The discharge induces a small electric pulse in the wire

TABLE 2.3.--Iro

--172.7 cm outer
--Lengths vary t
--Saturation cur
--Average field

--Residual "dega

--Each magnet =
--Spectrometer =
--Field measured

--Radial dependen

B(r) = A/r

Magnet	
1,3,5,7	
2,4,6,8	

--Transverse momen
--RMS transverse
per magnet = .1

TABLE 2.3.--Iron Toroid Magnets

--172.7 cm outer diameter, 30.5 cm inner diameter

--Lengths vary between 78.1 and 79.2 cm

--Saturation current ~35 A, 450 turns

--Average field = $\frac{\int B(r)\, dr}{\int dr}$ = 17.09 Kg magnet 1,3,5,7 at 34.5A

= 17.27 KG magnet 2,4,6,8 at 36.6A

--Residual "degaussed" field = 134 gauss magnet 1,3,5,7
244 gauss magnet 2,4,6,8

--Each magnet = 7.87 gm/cm^3 x 80 cm = 629.6 gm/cm^2

--Spectrometer = 8 magnets x 629.6 = 5036 gm/cm^2

--Field measured using (i) B-H curve was measured for a smaller toroid of the same type, and scaled up

(ii) B(r) measured directly using a coil wound around one slab of the toroid; coil passed through the center of the toroid and small holes drilled in the body of the toroid slab

--Radial dependence of the field known to within 1%

$B(r) = A/r + C + Dr + Fr^2$ $\quad \frac{B(KG)}{r(cm)}$

Magnet	A	C	D	F
1,3,5,7	12.20	19.92	-.08357	.0004346
2,4,6,8	12.07	19.71	-.0827	.0004301

--Transverse momentum "kick" due to one magnet = .4 GeV/c

--RMS transverse momentum "kick" from multiple scattering per magnet = .1 GeV/c

nearest to it, w
strictive wire [6]
wires. In our s
removal and is p
prevent corrosio
wires causes an
wire which propa
edge. The change
change in magnet
amplifier, and ze
Along with wires
sparked every tim
pulses (fiducial
sent to special
which were previo
position of the f
were easily conve
must be used at s
dimensional (X-Y)
dancy, each of ou
oriented at 45° w
particularly usef
able in each plan
ment.

It is ver
spark chambers in

nearest to it, which is sensed in our chambers via a special magnetostrictive wire[6] (called a wand) stretched perpendicular to the grid wires. In our system, the wand is mounted separately for easy removal and is packed in a small tube, flushed with Argon gas to prevent corrosion. The electromagnetic pulse in one of the grid wires causes an acoustic stress pulse in the magnetostrictive wand wire which propagates at a known constant speed to the chamber edge. The change in permeability of the polarized wire causes a change in magnetic flux, which is sensed by a pick-up coil, preamplifier, and zero-crossing discriminator (Figures 2.5 and 2.6). Along with wires fired by particles, two special fiducial wires are sparked every time the chamber is triggered. Thus, a sequence of pulses (fiducial 1, up to seven fired wires, and fiducial 2) are sent to special devices called time digitizer converters (TDCs), which were previously started by the trigger. Since the spatial position of the fiducials was accurately known, the times of arrival were easily converted into spatial coordinates. Two wire planes must be used at some angle (90° in our chambers) to give two-dimensional (X-Y) coordinates for the sparks. To give added redundancy, each of our spark chambers had another set of two wire planes oriented at 45° with the first (measuring U-V coordinates). This was particularly useful in view of the limited number of sparks allowable in each plane and the failure of several planes during the experiment.

It is very important to achieve the correct gas mixture in spark chambers in order to have good spatial resolution and efficiency.

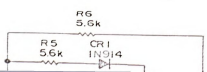
R6
5.6k
R5
5.6k
CR1
IN914

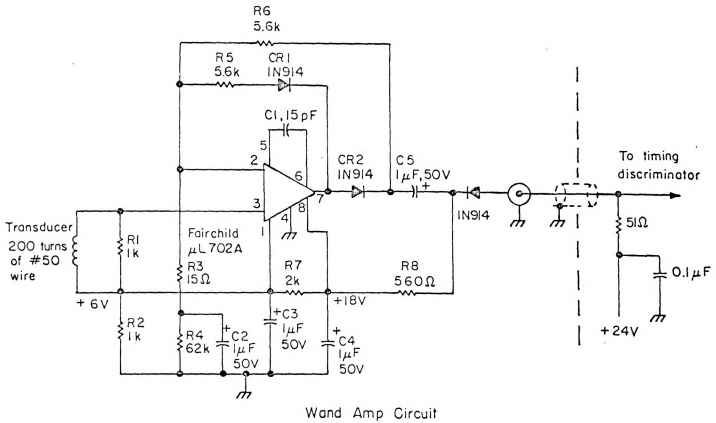

Figure 2.5.--Magnetostrictive Wand Amplifier Electronics for E319 Spark Chambers.

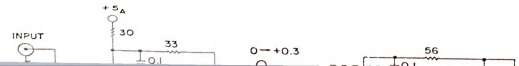
+5A
INPUT
30
33
0.1
0—+0.3
56
0.1

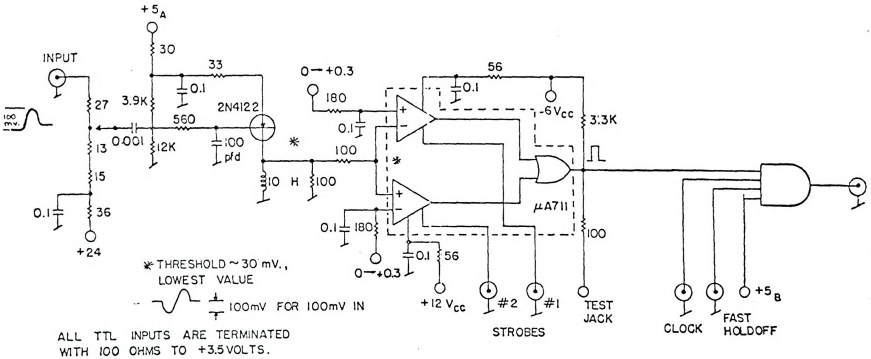

ZERO CROSSING PEAK DETECTOR

Figure 2.6.--Zero-Crossing Discriminator Electronics for E319 Spark Chambers.

A specially desi
distribute the r
cold traps, addi
constituent (~82
spark discharge
the chamber edge
limits spark cur
for the wands an
(to prevent spur

The firi
a hydrogen thyra
high voltage pul
break down, they
onto the chamber
shape of the high
altering the spar
time of these bar
times the chamber
that more secure
thyratrons for ea
for E319.

Since par
ing a beam spill,
disperse quickly
sparks. To keep

A specially designed (Berkeley) gas cart was borrowed to mix and distribute the neon-helium gas and purify the returning gases within cold traps, adding traces of alcohol and argon. Neon is the main constituent (~82%) because of its high ionization potential and spark discharge shape. The helium and argon suppress breakdown at the chamber edges and lower the high voltage needed, while alcohol limits spark currents and improves multi-track efficiency. Argon for the wands and pressurized nitrogen for the chamber spark gaps (to prevent spurious breakdown) were also dispensed by the gas cart.

The firing circuit for the spark chambers (Figure 2.7) used a hydrogen thyratron which, when pulsed by the trigger logic, sends high voltage pulses to all chamber spark gaps. When these gaps break down, they switch high voltage stored in large capacitor banks onto the chamber planes, allowing spark formation to begin. The shape of the high voltage pulse is crucial and can be varied by altering the spark gap pressure or the capacitor banks (the charging time of these banks is around 30-40 ms which limits the number of times the chambers can be fired to < 50 per two-second spill). Note that more secure firing of the chambers would require independent thyratrons for each gap, but lack of money and time prevented this for E319.

Since particles are always passing through the chambers during a beam spill, ion channels are constantly formed and would not disperse quickly enough if left alone, leading to many spurious sparks. To keep the memory time of the chamber low (~1 μs), a

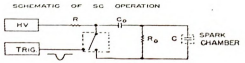
SCHEMATIC OF SC OPERATION
HV
TRIG
R
C_D
R_D
C
SPARK CHAMBER

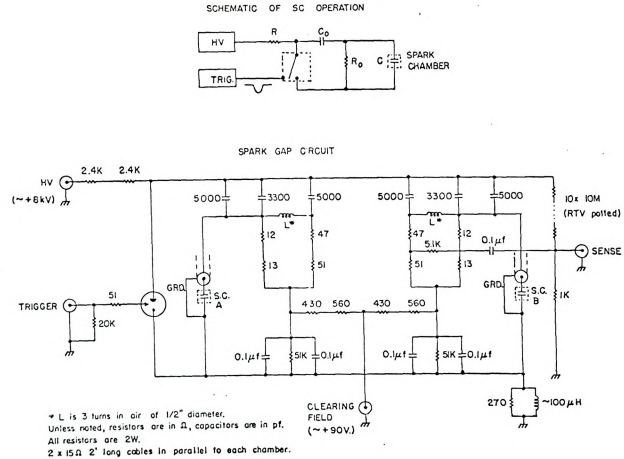

Figure 2.7.--Spark Gap Firing Electronics for E319 Spark Chambers.

constant clearin

sweeps the ions

clearing field w

sparks).

To ready

to their final p

gaps cleaned. Th

with a special ji

thoroughly flushe

were made to opti

(a) high voltage

(c) gas mixture (

(30-40 V) and (e)

chamber. The resu

cation and alcoho

ject to frequent b

non-optimum at tim

graph). Furthermo

to multitrack effi

Temperature and hu

caused some time-d

Finally, several p

useless due to con

and wand problems.

and efficiency han

constant clearing field of ~40 V is applied to the planes, which sweeps the ions to their respective plates (note that too large a clearing field would disrupt the ion channels which give desired sparks).

To ready the spark chambers for E319, they had to be moved to their final positions, leak tested (using helium) and the spark gaps cleaned. The wands also had to be polarized and checked out with a special jig to test their response. After the chambers were thoroughly flushed with the Ne-He mixture, a sequence of beam tests were made to optimize the following parameters for each chamber: (a) high voltage (~8-9 kV); (b) N_2 pressure on gaps (~5-15 PSI); (c) gas mixture (particularly alcohol); (d) clearing field voltage (30-40 V) and (e) delay time between trigger and application of HV to chamber. The results are listed in Table 2.4. We note that the purification and alcohol distributing functions of the gas cart were subject to frequent breakdown leaving the quality of the gas mixture non-optimum at times (it was monitored with the use of a gas chromatograph). Furthermore, the chambers performed unevenly with respect to multitrack efficiency, especially when the halo rate was high. Temperature and humidity (most of the running was done in the summer) caused some time-dependent problems with the spark gap system. Finally, several planes (specifically 6XY, 8XY, and 9Y) were often useless due to continuous breakdown at some places within the chamber, and wand problems. Due to problems like these and the general rate and efficiency handicaps, all second generation muon experiments[7]

TABLE 2.4.--Spark

--Each module has
relative to each
--25 mil Al plates
--Active area = 73"
--Be-Cu wires .005"
--Wire spacing = .7
--Distance between

--High voltage for

Chamber	
Voltage (kV)	

--From time of trig
--Recovery time of
--Memory time = 1 μ
--Gas mixture: Ne
Ar
Al
--Ar in wand cathet
--$\frac{1}{2}$ gap pressures

Chamber	1
Pressure	15

TABLE 2.4.--Spark Chamber Properties

--Each module has two pairs of orthogonal wire planes at 45 degrees relative to each other

--25 mil Al plates 80" x 80" outer dimension

--Active area = 73" x 73"

--Be-Cu wires .005" in diameter

--Wire spacing = .7 mm

--Distance between fiducial wires = 184.15 cm for ch's 1,2,3,4,5
= 182.88 cm for ch's 6,7,8,9

--High voltage for each chamber module:

Chamber	1	2	3	4	5	6	7	8	9
Voltage (kV)	8.6	8.4	8.4	7.6	7.6	8.6	7.6	7.8	8.4

--From time of trigger signal to spark gap breakdown - 220 ns.

--Recovery time of charging capacitor in spark gap box = 40 ms.

--Memory time = 1 μ sec (a clearing field sweeps out stale ions)

--Gas mixture:

Ne-He	78-80 %	gas purified in
Ar	2-3 %	"Berkeley" purifier
Alcohol	.7 SCFH @ 80°F	and recirculated

--Ar in wand catheters, N_2 in spark gaps

--N_2 gap pressures (PSI):

Chamber	1	2	3	4	5	6	7	8	9
Pressure	15	10	18	7	6	9	13	15	15

now use large p
expensive, can
bility.

In E26,
which were upst
by hadrons leak
much of the ana
two chambers, t
installed. The
and the small or
covering the act
well at stopping
one shield is <
complication of
This has made po
ithms which star
described in Cha

2.6 Electronics

All mode
amount of electr
nature of the de
to take and anal
ubiquitous: powe
along with distr
increase the usua

now use large proportional or drift chambers which, while much more expensive, can handle higher rates with excellent multi-track capability.

In E26, it was found that their front four spark chambers, which were upstream of the iron magnets, were frequently saturated by hadrons leaking from the target, making them nearly useless for much of the analysis. To prevent this from happening to our front two chambers, two large iron plates (called hadron shields) were installed. The largest (61.6 cm thick) was upstream of chamber 9 and the small one (37.5 cm thick) between chambers 9 and 8, with both covering the active area of the spark chambers. They worked very well at stopping hadrons (the probability for a pion to penetrate one shield is $< 3\%$ and both shields is $< 0.5\%$), adding only the small complication of multiple scattering and energy loss in the iron. This has made possible the development of new reconstruction algorithms which start at the front of the spectrometer as will be described in Chapter 3.

2.6 Electronics

All modern high energy physics experiments have an enormous amount of electronics associated with them due to the indirect nature of the detection process and the fact that computers are used to take and analyze data. A few basic types of circuits are ubiquitous: power supplies for high and low voltage applications (along with distribution circuits for these), fast amplifiers to increase the usually small detector signal sizes, discriminators

which accept on
level pulses, lo
count signals, t
length of time b
verters (ADC) to
the measured cha
has arrived or n
detectors, make
and to convert t
form for the com
ing already desc
section concentr
major decision t
the event) is wh
detector reading
The triggering de
C and HV), trigge
good beam muon is
time of 15-20 ns.
and the absence o
$B \cdot C \cdot \overline{HV}$). Nex
the beam veto (de
BV_3 with either o
some combination
trigger S require

which accept only signals of certain sizes and produce standard (NIM) level pulses, logic circuits to make limited decisions, scalers to count signals, time digitizer converters (TDC) which digitize the length of time between pulses of interest, analog to digital converters (ADC) to convert voltage pulses to numbers proportional to the measured charge, and latches (DCR) which record whether a pulse has arrived or not. The purposes of all this are to: operate the detectors, make electronic choices of which events will be recorded, and to convert the output of the detectors into recognizable (digital) form for the computer to process and write onto magnetic tape. Having already described most of the detector-related electronics, this section concentrates on triggering and recording functions. The major decision to be made by the electronics (within 50-100 ns of the event) is whether the spark chambers are to be triggered and the detector readings recorded for later processing by the mini-computer. The triggering decision is determined by information from beam (B, C and HV), trigger bank (SA, SB, SC) and beam veto (BV) counters. A good beam muon is signalled by the presence, within a coincidence time of 15-20 ns, of pulses from all three B and all three C counters and the absence of a signal from the HV bank (symbolically Beam $\equiv$ $B \cdot C \cdot \overline{HV}$). Next, the trigger requires the absence of a signal from the beam veto (defined by the coincidence of the downstream counter BV_3 with either of the two upstream, $BV = [(BV_1 + BV_2) \cdot BV_3]$). Finally, some combination of trigger counters must have been hit. The main trigger S requires a hit in each of the three banks (the old and new

banks are added

trigger is Beam

requiring two (

$(SA \geq 2) \cdot (SB \geq$

because, frequer

trigger bank or

select high angl

or inner segment

included is unli

free-running pul

this pulser trig

unbiased by the

simulation progr

type.

Actual f

counter signals

Desired combinat

the two ends of

each of these ou

bank). The trig

priate combinati

the signals is c

Muon lab, and elec

travel in coaxial

which take advant

banks are added together) written S = SA • SB • SC so that the full trigger is Beam • S • $\overline{BV}$. A dimuon trigger SD was also formed by requiring two (or more) hits in the first two trigger banks SD = (SA $\geq$ 2) • (SB $\geq$ 2). This did not select multimuon events very well because, frequently, one of the muons is within the hole at the SA trigger bank or has left the spectrometer before SB. Other triggers select high angle (SH) or low angle (SL) events by choosing the outer or inner segments of the last (SC) trigger bank. The final trigger included is unlike the others in that only the random overlap of a free-running pulser with a Beam signal is required. The purpose of this pulser trigger was to select a random sample of beam muons, unbiased by the apparatus acceptance, for later use with Monte Carlo simulation programs. About 5% of the triggers on tape were of this type.

Actual formation of triggers began with discriminating all counter signals to reject noise and provide standard NIM pulses. Desired combinations of counters are achieved by logic circuits (e.g., the two ends of each trigger bank counter are ORed together and then each of these outputs is combined in one master OR for the trigger bank). The trigger is made by forming the coincidence of the appropriate combinations as described above. Note that the timing of the signals is crucial since the counters were placed all over the Muon lab, and electrical signals take roughly 1 ns for every foot of travel in coaxial cable. Timing is accomplished with delay cables, which take advantage of this travel time, and must be done to within

a few nano-seco

19 ns. The big

long distance f

they arrive so

this job can be

Figures 2.8 and

Besides

output of all de

read. Three set

recording of suc

tronics during t

FNAL supplies be

to cosmic rays a

logic after ever

chambers to reco

Finally, trigger

to prevent alter

or other electri

event gate is re

The reco

basic types: (1

pulses to digita

to numbers and a

(3) DCRs or latch

criminator thresh

a few nano-seconds since the FNAL beam structure allows muons every 19 ns. The biggest problem encountered in our experiment was the long distance from the apparatus to the B counters which, because they arrive so late, must determine the timing. The complexity of this job can be appreciated by examining the trigger logic in Figures 2.8 and 2.9.

Besides forming the trigger, the electronics must record the output of all detectors in a form suitable for the mini-computer to read. Three sets of gates are generated to control the flow and recording of such information. The spill gate activates the electronics during the time (usually about 2 sec. every 15-20 secs.) when FNAL supplies beam (see sec. 2.7) to prevent accidental triggers due to cosmic rays and/or noise. An event gate suppresses the trigger logic after every good trigger for about 40 ms to allow the spark chambers to recover and the mini-computer to process the event. Finally, trigger veto gates are supplied to all recording electronics to prevent alteration of the stored event data due to spark chamber or other electrical noise and to reject additional signals until the event gate is restored. The full gate logic is shown in Figure 2.10.

The recording circuits for the E319 detectors are of four basic types: (1) ADCs used to convert the calorimeter counter pulses to digital form; (2) TDCs for changing the spark arrival times to numbers and also employed to record some counter signal timing; (3) DCRs or latches which simply record 0 if no signal above a discriminator threshold arrives within a gate and 1 if a signal is

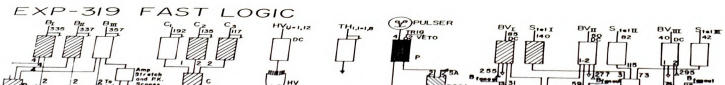
EXP-319 FAST LOGIC
PULSER
TRIG
VETO
HV
P
2LE
DC

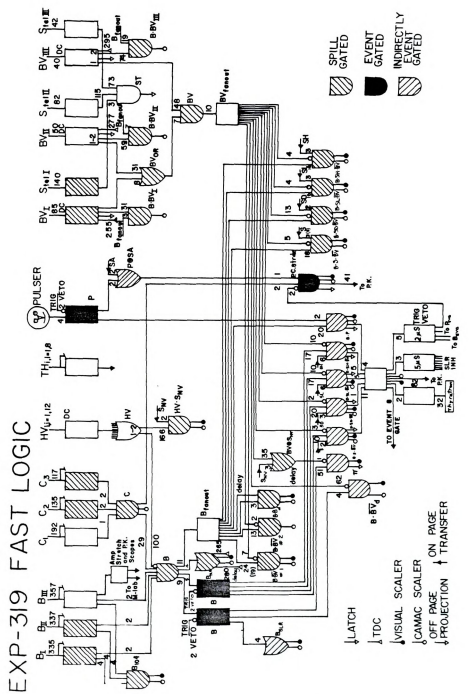

Figure 2.8.--E319 Trigger Logic Diagram.

EXP-319 FAST LOGIC

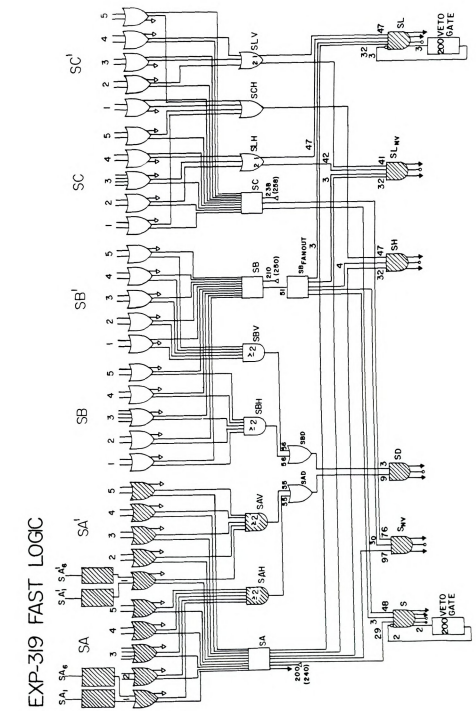

Figure 2.9.--E319 Hodoscope Logic Diagram.

E-319 GATE LOGIC

E-319 GATE LOGIC

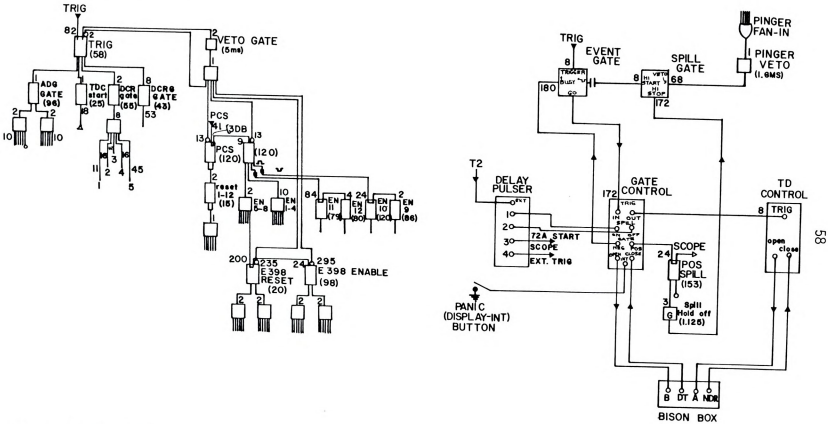

Figure 2.10.--E319 Gate Logic Diagram.

present (these
(4) scalers to
ADCs used were
basic function
within a short
number which ca
was 0-256 pC ((
fold overloads.
pulses were not
we found that s
and distort the
a LeCroy repres
developed for a
runs. Since th
the gate ground

Time di
the start signa
timed arrives.
time, which is
TDCs (built spe
Figure 2.11) th
trigger and eac
sent to a shift
TDCs were start
(e.g., BV count
late in the exp

present (these are used to record hit PC wires and counters); and (4) scalers to count signals for counter and logic modules. The ADCs used were LeCroy 2249A 12 channel linear response devices whose basic function is to accurately store the total incoming charge within a short gate time (100 ns) and later convert it to a channel number which can be fed to the computer. The range of these devices was 0-256 pC (Channels 1-1024) and they claimed to reject up to 1000-fold overloads. This turned out to be true only if large noise pulses were not induced in the ground lines. During the experiment, we found that spark chamber noise was able to re-open the input gates and distort the ADC digitizing for some modules. In cooperation with a LeCroy representative, special ferrite core transformers were developed for all ADC inputs to damp the noise problems for our later runs. Since the conclusion of our experiment, LeCroy has re-designed the gate grounding to avoid this difficulty.

Time digitizer converters work by starting a fast clock when the start signal is received and stopping it when the signal to be timed arrives. Knowing the constant clock rate gives the elapsed time, which is converted to digital form. For the spark chamber TDCs (built specially for these chambers and schematically shown in Figure 2.11) the start comes via a special controller from the trigger and each of the up to eight sparks has its scaler reading sent to a shift register to be read later by the computer. Counter TDCs were started by a beam signal and stopped by counter signals (e.g., BV counters). These latter TDCs were not properly timed until late in the experiment so that little use has been made of them.


bit #1
bit #1

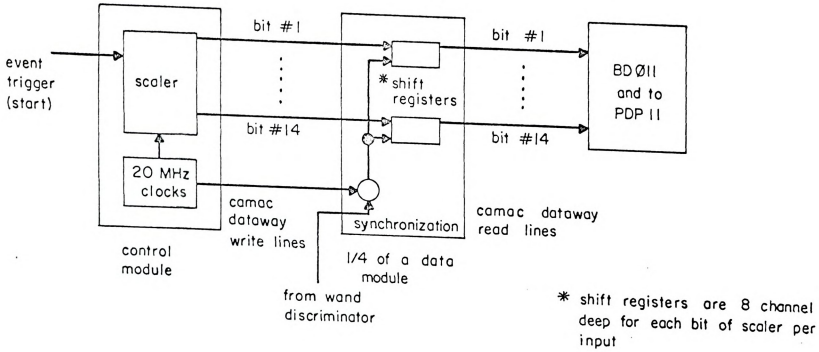

Simplified Schematic of Time Digitizer System

Figure 2.11.--Schematic of Spark Chamber Time Digitizer System.

The s
every good tr
clear separati
state dependir
are reset just
to receive sig
located so far
latches. Thus
PCS = C • (SA
pulser. The t
so far upstrea
experiment, so
The DCRs used
PC latches, alt
because of the
particular). T
Chapter 3. T
experiment; the
manually copied
kind (LeCroy 25
redundancy was
scalers is vita
Furthermore, th
and apparatus m

The min
was a DEC PDP 1

The status of each proportional chamber wire is recorded (for every good trigger) in a latch, which discriminates the signal for clear separation from noise and then sets itself into a "no" or "yes" state depending on whether the wire was missed or hit. The latches are reset just prior to the expected signal arrivals and then enabled to receive signals for 100 ns. Note that because the B counters are located so far upstream, they would arrive too late to open the latches. Thus, the strobe signal is a subset of the actual trigger PCS = C • (SA + P) where SA is the first trigger bank and P is the pulser. The timing problem is worst for the E98 PCS since they are so far upstream and, indeed, it was incorrectly done for most of the experiment, so that the wrong beam track was latched for every event. The DCRs used for latching counter signals (LeCroy 2340) work like the PC latches, although the gate width must be kept short (~40 ns) because of the very high rates in some of the counters (B and BV in particular). The list of signals latched in E319 will be shown in Chapter 3. Two sets of scalers were used to count signals for this experiment; the first kind employed an LED readout and readings were manually copied into logbook records after every run while the second kind (LeCroy 2551) were read by the computer at each event. The redundancy was necessary mostly because the flux information on these scalers is vital to determining normalization of the experiment. Furthermore, the visual scalers were the principal beam-tuning tool and apparatus monitor during data taking.

The mini-computer used to control the data recording for E319 was a DEC PDP 11/45 on loan from FNAL. Equipped with 32k words of

memory (core)
the computer w
the data onto
tasks within th
the electronics
nationally star
controls the ti
and crate contr
electronic modu
network with in
transfer functi
driver which ca
what of a limit
would like to ha

Once the
store the block
written per reco
360) as 9-track
the format of th
analysis, with t
problem with the
drive, requiring
two to change ta
preliminary on-l
the performance
chamber ineffici

memory (core) and a specially designed disk-resident operating system, the computer was able to supervise all data recording devices, write the data onto magnetic tape, and perform some on-line monitoring tasks within the 40 ms dead time for each event. Interaction with the electronics occurs through a BD011 branch driver using the internationally standard CAMAC data transfer system. The branch driver controls the timing of data flow to the computer from each CAMAC crate, and crate controllers, which reside in each crate, control individual electronic modules. These are all connected by the branch highway network with individual wires assigned to timing, power, and data transfer functions. The crates are read serially by the branch driver which can handle up to seven of them (this proved to be somewhat of a limitation for us since there were other counters which we would like to have latched or scaled).

Once the computer received the data, its main priority was to store the block for writing to magnetic tape. Four events were written per record, although these tapes were then copied (via an IBM 360) as 9-track tapes with two events per record. (Table 2.5 details the format of the event block.) The copies have been used for all analysis, with the actual data tapes stored at FNAL. The only real problem with the tape writing was that we had just a single tape drive, requiring a down-time of roughly five minutes every hour or two to change tapes. The second function of the operating system was preliminary on-line analysis of the data. It was essential to monitor the performance of the detection systems to spot problems like spark chamber inefficiency, dead channels in the proportional chambers or

Table

Words
1-15
16-87
88-179
180-215
216-220
221-228
229-456
457-464
465-761
762-768

Table 2.5.-- Primary data tape format

Words	Contents	# words used
1-15	I.D. block	15
16-87	24-bit scalers	72
88-179	E319 PC's	92
180-215	E398 PC's	36
216-220	DCR's	5 packed
221-228	TDC's	8 packed
229-456	ADC's	228 packed
457-464	unused	8
465-761	WSC digitizers	297
762-768	unused	7
		768 words/event

calorimeter, e
being written
made for every
important duri
computer check
and software ca

2.7 Fermilab a Beam Line

Fermila
west of Chicago
accelerators (t
calling for 10^{1}
upgraded to ope
protons/spill (
performance).
with the pre-ac
beam of protons
accelerator to
for injection i
reached. At th
intensity) is i
circumference o
to 400 GeV and,
experimental ar

calorimeter, etc., and to get an idea of the character of the events being written to tape. Paper outputs of these on-line analyses were made for every run in the experiment. These tasks became especially important during calibration runs when time was too short for off-line computer checks. A description of the mini-computer operating system and software can be found in the thesis of R. Ball.[8]

2.7 Fermilab and the Muon Beam Line

Fermilab (located in Batavia, Illinois, roughly 40 miles west of Chicago) is the site of one of the world's largest proton accelerators (the other is at CERN). Built in 1969 with a design calling for 10^{12} protons/spill at 200 GeV, the accelerator has been upgraded to operation at 400 GeV with intensities up to 2×10^{13} protons/spill (although often at the expense of rather unstable performance). The accelerator contains four major stages beginning with the pre-accelerator, which is designed to produce a very intense beam of protons at 750 KeV. This beam is steered into a linear accelerator to boost the energy up to 200 MeV. This is sufficient for injection into a small synchrotron (the booster) where 8 GeV is reached. At the appropriate time the beam (now somewhat reduced in intensity) is injected into the main synchrotron ring, which has a circumference of over 4 km. Here the beam is boosted to energies up to 400 GeV and, every 15-20 seconds, switched out to the three main experimental areas (Figure 2.12). During our runs, the accelerator

Figure 2.12.--

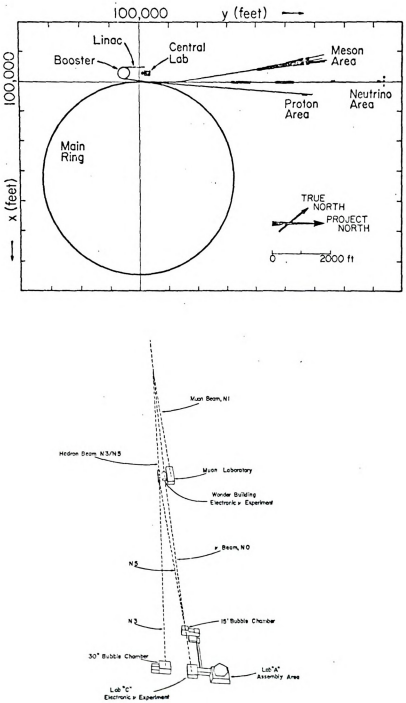

Figure 2.12.--Layout of Fermilab (top) and Detail of the Neutrino Area (bottom). (E319 was located in the Muon Laboratory).

proved quite te
(requiring eigh
tion problems.
8-10 x 10^{12} pro
caused the elim
planned with di
priority at Fer
order of magnit
time.

The muo
Figure 2.12, bo
aluminum cylind
Neutrino area.
kaons) is guide
magnets called
beam dump. Aft
long, evacuated
to yield muons
enclosure (100)
type dipoles (1
ring quadrupoles
through the eart
again focused (1
momentum selecti
bends the beam b

proved quite temperamental with frequent main ring magnet failures (requiring eight or more hours to repair) and severe power distribution problems. Suffice it to state that our promised intensity of 8-10 x 10^{12} protons per spill really averaged around 3-5 x 10^{12}. This caused the elimination of valuable calibration time and the runs planned with different target materials. However, we did enjoy top priority at Fermilab during our main data runs, which represented an order of magnitude increase in statistics on muon scattering at the time.

The muon (N1)[9] and neutrino beams, schematically shown in Figure 2.12, both stem from protons smashing into targets (a 12" aluminum cylinder for muons) in the first enclosure (99) of the Neutrino area. The resulting shower of hadrons (mostly pions and kaons) is guided through an initial set of focusing and steering magnets called the triplet train, while the protons continue on to a beam dump. After the mesons pass the triplet train, they enter a long, evacuated decay pipe where the decays $\pi \rightarrow \mu\nu$ and $K \rightarrow \mu\nu$ begin to yield muons and neutrinos. When the beam reaches the next enclosure (100) the charged particles are bent (west) by main ring type dipoles (1W0), vertically trimmed (1V0), and focused by main ring quadrupoles (1F0, 1D0), while the neutrinos sail on unaffected through the earth berm covering the beam lines. The π/μ beam is again focused (1Q1), and bent back east (1E1) in enclosure 101, thus momentum selecting only part of the beam. Enclosure 102 trims and bends the beam back west (1V2 and 1W2), again momentum selecting.

At this point,
ethylene blocks
rons leaving a
in a dispersion
of halo further
are obtained by
The spreading b
with quadrupole
(1F3, 1D3). Th
water randomly.
enclosure 104 w
(Figure 2.13 sh
shimmed main rin
which, when push
GeV muons. The
the field (i.e.,
tine so as to mi
lens). However,
caused so we set
GeV. Since thes
we carefully mea
and spatial posi
/ B · dl needed
angle of the dip
results, shown i

At this point, the still partly-pion beam can be filtered by polyethylene blocks in the beam pipe and magnet apertures to remove hadrons leaving a "pure" muon beam. This does result, unfortunately, in a dispersion (due to multiple scattering) which is a prime source of halo further downstream. Note that hadron beams for calibration are obtained by removing the CH_2 blocks (a several hour exercise). The spreading beam passes through a final focus in enclosure 103 with quadrupoles salvaged from the old Cambridge electron accelerator (1F3, 1D3). These magnets showed their age by overheating and leaking water randomly. Final momentum selection is performed in the last enclosure 104 with dipoles (1E4) bending the beam eastward again. (Figure 2.13 shows the full muon beam line.) These magnets were shimmed main ring dipoles (to increase the field and bending angle) which, when pushed to their current limits, would handle up to 300 GeV muons. The normal solution employed with such magnets is to ramp the field (i.e., bring it up to maximum only during actual beam spill time so as to minimize the average current and reduce heating problems). However, the shims were too unstable for the stresses this caused so we settled for d.c. running at the reduced energy of 270 GeV. Since these magnets constituted the final momentum selection, we carefully measured their magnetic field as a function of current and spatial position (so as to derive the total field integral $F = \int B \cdot dl$ needed to determine momentum $P = \frac{.03}{\theta} F$, where θ is the bend angle of the dipoles) using an NMR probe and a gaussmeter. The results, shown in Figure 2.14, were used in our beam energy routine

Muc
Lab

Figure 2.13.--Muon

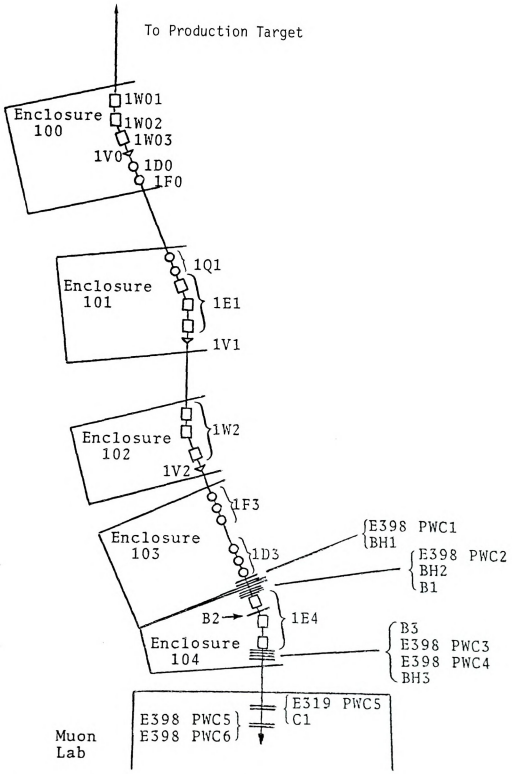

Figure 2.13.--Muon (N1) Beam Transport and Detectors.

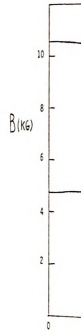

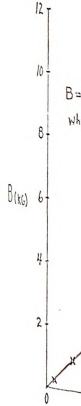

Figure 2.14.--C

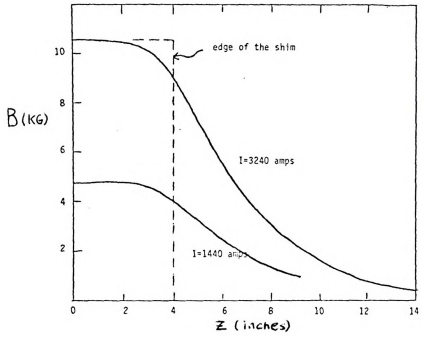

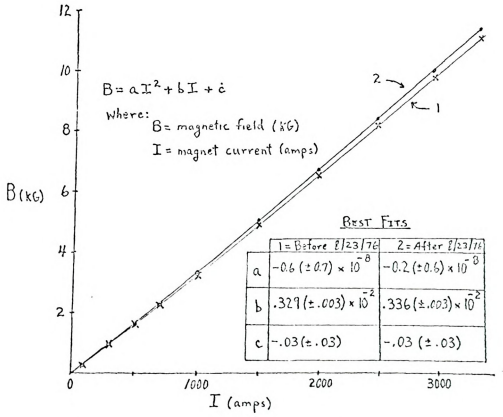

Best Fits

	1 = Before 8/23/76	2 = After 8/23/76
a	$-0.6\ (\pm 0.7) \times 10^{-8}$	$-0.2\ (\pm 0.6) \times 10^{-8}$
b	$.329\ (\pm .003) \times 10^{-2}$	$.336\ (\pm .003) \times 10^{-2}$
c	$-.03\ (\pm .03)$	$-.03\ (\pm .03)$

Figure 2.14.--Characteristics of Dipole Magnets in Beam Enclosure E104.

(Chapter 3).

the extracted

Neutrino depar

and muons down

beam is monito

bers (when the

each bend. Cor

ments by remote

As the beam was

of quality were

(b) minimize th

(c) achieve rea

chambers, parti

The main data r

the calibration

cal tune is sho

Althoug

and balky to op

intense (up to

muons, then ava

better muon bea

new muon beam d

(Chapter 3). The Fermilab control room is responsible for tuning the extracted proton beam into the Neutrino area. From there, Neutrino department physicists worked with us to propagate the hadrons and muons down the N1 beam line to the front of our apparatus. The beam is monitored at each enclosure by counters and ionization chambers (when they work), allowing one to optimize the shape before each bend. Control of magnet settings was available to the experiments by remote consoles connected to a mini-computer (MAC) system. As the beam was gradually tuned toward our apparatus, three measures of quality were used: (a) maximize the rate in the B and C counters; (b) minimize the halo (monitored by the coincidence HV · S); and (c) achieve reasonable shapes and spot sizes in the beam proportional chambers, particularly avoiding scraping the beam on magnet edges. The main data runs achieved quite adequate tunes, although many of the calibration runs were sloppier because of lack of time. A typical tune is shown in Table 2.6.

Although this muon beam was old, somewhat hastily designed, and balky to optimize, it did supply a relatively small (~4" square), intense (up to 10^6 muons/spill), high energy (270 GeV) source of muons, then available nowhere else. CERN has since developed a much better muon beam,[10] putting Fermilab muon physics in limbo until a new muon beam designed to work with the Tevatron[11] can be build.

TABLE 2.6.--Ty

Magnet	Typ Pur
QUT	Targ
QVT	Targ
QHT	Targ
QFT1	Focu
QFT2	Focu
QDT	Focu
QPT	Bend
QPT3	Bend
TWQ1	Firs
TWQ2	Firs
TWQ3	Firs
TVQ	Vert.
TFQ	Focus
TDQ	Focus
TQ1	Focus
TE1	2nd B
TV1	Vert.
TW2	3rd B
TV2	Vert.
TF3	Final
TD3	Final
TE41	Final
TE42	Final

TABLE 2.6.--Typical N1 Beam Line Tune for 270 GeV

Magnet	Type or Purpose	Location	Set Value (amps)	Read Back Value (amps)
OUT	Targeting	E99 (Neuhall)	110.0	111.2
OVT	Targeting	E99 (Neuhall)	15.0	15.2
OHT	Targeting	E99 (Neuhall)	121.0	117.5
OFT1	Focus	E99 (Neuhall)	96.2	92.7
OFT2	Focus	E99 (Neuhall)	95.6	92.4
ODT	Focus	E99 (Neuhall)	2777.0	2690
OPT	Bend	E99 (Neuhall)	3102.0	2978
OPT3	Bend	E99 (Neuhall)	3177.0	3060
1WO1	First Bend	E100	Slave	4625-4636
1WO2	First Bend	E100	4332.0	4180-4200
1WO3	First Bend	E100	4832.0	4630-4640
1VO	Vert. Trim	E100	25.0	1.06
1FO	Focus. Quads	E100	370.0	361.5
1DO	Focus. Quads	E100	370.0	353.4
1Q1	Focus. Quads	E101	4175.0	4000-4048
1E1	2nd Bend	E101	3862.0	3715-3730
1V1	Vert. Trim	E101	120.0	7.62
1W2	3rd Bend	E102	3712.0	3550-3560
1V2	Vert. Trim	E102	off	0.0
1F3	Final Focus	E103	970.0	947.5
1D3	Final Focus	E103	1000.0	975.0
1E41	Final Bend	E104	4320.0	4237.5
1E42	Final Bend	E104	Slave	4223.7

2.8 Riding th
Apparatus

By way

the whole appa

and focused fo

enclosures 103

whose signals

enclosure 104,

signals to the

E98 detectors

supplying the

Passing through

the front of th

beam PCs, as we

bank (unless th

this informatio

trigger logic,

Although the pr

to be detected

muon does inter

of the muon and

ing the target,

proportional ch

hadrons, if any

chambers and ma

radially inward

2.8 Riding the Muon Through the Apparatus

By way of summary, let us follow the path of a muon through the whole apparatus. Born by the decay of a pion, the muon is bent and focused four times as it travels through the beam line. At enclosures 103 and 104 it registers on the E98 PCS and hodoscopes, whose signals race downstream towards the electronics. Also in enclosure 104, the B counters are hit and fast cables send these signals to the trigger logic. As the muon enters the lab, the final E98 detectors as well as our upstream PCS and counter C1 are struck, supplying the final information needed to determine the momentum. Passing through the upstream apparatus of E398, the muon arrives at the front of the E319 target, hitting the remaining C counters and beam PCs, as well as the target hodoscope and missing the halo-veto bank (unless this muon is outside of the beam radius). While all of this information is making its way to the recording devices and trigger logic, the muon plows into the iron target/calorimeter. Although the probability of an interaction at a large enough angle to be detected by the spectrometer is quite small, we assume our muon does interact. The calorimeter counters register the passage of the muon and the hadron shower produced in the interaction. Leaving the target, the now scattered muon(s) register in the hadron proportional chambers and pass into the spectrometer with accompanying hadrons, if any, stopped in the hadron shields. Traversing the spark chambers and magnets, the muons leave ion trails, while bending radially inward (outward) if their charge is the same (opposite) as

that of the b

arrive at the

muons sail ou

the spark char

the detector

the mini-compu

display, if de

next muon to c

this recorded

muon interacti

that of the beam. Eventually, trigger banks are hit, and the signals arrive at the electronic logic to complete the trigger. While the muons sail out of the end of the apparatus to decay, the logic fires the spark chambers and all recording modules are gated on to receive the detector information. For the next 40 ms, this data is read by the mini-computer, written to tape, and processed for immediate display, if desired. Then all of the electronics is readied for the next muon to come along. The next chapter will discuss how all of this recorded information is analyzed to reconstruct the physics of muon interactions.

3.1 Summary o

The or

ment with Ferm

target) to be

90 GeV). The

ratio of beam

designed to el

different ener

useful in the

Also, to maxim

most of the da

a short run at

the beam was p

higher intensit

check possible

runs with incid

$\pi N \rightarrow \mu X$ and πN

reactions), run

possible system

numerous calori

CHAPTER 3

DATA ANALYSIS

3.1 Summary of Data Taken

The original plans for E319 (as outlined in the formal agreement with Fermilab)[1] called for 500 hours of beam time (protons on target) to be run at three incident muon energies (240, 150, and 90 GeV). The apparatus was to be rescaled in length by $\sqrt{\lambda}$ where λ = ratio of beam energies for each different energy. This scaling, designed to eliminate most systematic errors when data samples at different energies were compared, turned out to be only marginally useful in the analysis of the E26 data and was not employed in E319. Also, to maximize high q^2 and multimuon production, we decided to run most of the data at the maximum muon energy available (270 GeV) with a short run at 150 GeV to check energy dependence. The polarity of the beam was positive for most of the runs (since the $\mu+$ beam has higher intensity) although a run with negative polarity was made to check possible weak interaction effects. Other data taken included runs with incident hadrons instead of muons (to allow study of $\pi N \rightarrow \mu x$ and $\pi N \rightarrow \mu\mu x$ within the same apparatus as comparable muon reactions), runs with reduced (1/3) target density (to understand possible systematic effects and compare to the E26 data), as well as numerous calorimeter and spectrometer calibration runs and various

tests and syst

data taken.

3.2 Data Deco
Initial Proces

This s

was retrieved

for the comput

line analysis

PDP records (c

records (60-bi

the CDC machin

CERN library u

LL7660) to rea

block (EVBLK)

(GETRUN) could

run or event o

10,000 events)

run number (wo

12) and words

data transfer s

have proven to

Next ir

typical numbers

ing. Although

of counters and

B/HV . S ratios

tests and systematic studies. Table 3.1 summarizes the experimental data taken.

3.2 Data Decoding and Initial Processing

This section will describe how the data taken during E319 was retrieved from magnetic tape and converted into a form suitable for the computer algorithms which reconstruct the events. Such off-line analysis began with software routines to decode the two event PDP records (containing 768 16-bit words) into single event CDC records (60-bit words), since all of our data has been processed on the CDC machines at MSU and Fermilab. This task was done using the CERN library unpacking routine UBYTE[2] with driver routines (LLREAD, LL1660) to read the tapes and place the decoded words into a common block (EVBLK) for transfer to all other software. Another routine (GETRUN) could be used if one quickly wanted to select a particular run or event on a tape (most tapes contain a single run with about 10,000 events). Of the first 15 words in each event block, only the run number (word 2), event number (word 3), beam spill number (word 12) and words 13-15 (which, if nonzero, signal an error in the CAMAC data transfer system telling off-line programs to ignore the event) have proven to be useful in analysis.

Next in order are the scalers listed in Table 3.2 with some typical numbers and ratios shown in Table 3.3 along with their meaning. Although all of these scaled numbers were valuable as monitors of counters and electronics during the experiment (e.g., the B/C and B/HV • S ratios were vital beam quality indicators) and as data

TABLE 3.1.--E3

Run Numbers	Tape (9
1- 28	002-0
29- 40	023-0
41- 53	034-0
54- 62	042-0
63- 73	050-0
74- 80	058-0
81- 90	063-0
91-104	071-0
105-112	078-0
113-132	081-0
133-141	070
142-146	084
147-162	085-0
163-172	094-0
173-177	099-1
178-221	102-1
222-394	118-2
395-426	253-2
427-466	268-2
467-478	297-3
479-542	305-3
543-566	346-3
567-583	357-3
584-590	369-3
591-594	371-3

TABLE 3.1.--E319 Data

Run Numbers	Tapes (9___)	Type of Data	Beam	Analysis Uses
1- 28	002-022	Equipment Tests	μ^+	None
29- 40	023-033	Hadron Calib. Tests	π^+	None
41- 53	034-041	Hadron Calib., Full Fe	π^+	None (E_0?)
54- 62	042-049	Hadron Calib., 2/3 Fe	π^+	None
63- 73	050-057	Hadron Calib., 1/3 Fe	π^-	None
74- 80	058-062	Hadron Calib., 2/3 Al	π^+	Calorimetry Studies
81- 90	063-069	Hadron Calib., Full Al	π^+	Calorimetry Studies
91-104	071-077	Hadron Calib., Full CH_2	π^+	Calorimetry Studies
105-112	078-080	Hadron Calib., No target	μ^+,π^+	Calorimetry Studies
113-132	081-084	Spark Chamber Tests	μ^+	None
133-141	070	Amplifier tests	--	Determines relative gains
142-146	084	Spark Ch. Batwings	μ^+	Alignment
147-162	085-093	KB Spectrometer Calib.	μ^+	Alignment
163-172	094-098	Hadron Calib. 2/3 Fe	π^+	Calorimeter Calib.
173-177	099-101	Hadron Calib., Full Fe	π^+	Calorimeter Calib.
178-221	102-117	Initial data tests	μ^+	Few tests useful
222-394	118-253	270 GeV data	μ^+	Main data runs
395-426	253-268	270 GeV, 1/3 target	μ^+	Data, but low statistics
427-466	268-297	150 GeV, 1/3 target	μ^+	Low energy data
467-478	297-305	CCM runs	μ^+	Spectrometer Calib.
479-542	305-346	270 GeV data	μ^-	Data runs
543-566	346-356	Hadron Calib. & Tests	π^+,π^-	Calorimeter Calib.
567-583	357-368	$\pi \rightarrow \mu$, $\mu\mu$ runs	π^+	Multimuons (Vector mesons)
584-590	369-370	Calorimeter tests	π^+	Uniformity
591-594	371-372	$\pi \rightarrow \mu$,$\mu\mu$ runs	π^+	Multimuons

TABLE 3.2.--E3

Word	Scaler
16-17	$B \cdot BV_1$
18-19	$B \cdot BV_2$
20-21	$B \cdot BV_3$
22-23	$(B \cdot B\overline{V})$
24-25	B_{spg}
26-27	$B \cdot B\overline{V}_{sp}$
28-29	B_{evg}
30-31	T_{evg} =
32-33	$(B \cdot S \cdot \overline{BV}$
34-35	$(B \cdot SD \cdot \overline{B}$
36-37	$(B \cdot SL \cdot \overline{B}$
38-39	$(B \cdot SH \cdot \overline{B}$

TABLE 3.2.--E319 Scaler Assignments

Word	Scaler	Word	Scaler	Word	Scaler
16-17	$B \cdot BV_1$	40-41	$(B \cdot S \cdot B\bar{V})_{spg}$	64-65	$(SL)_{NV}$
18-19	$B \cdot BV_2$	42-43	$(B \cdot SD \cdot B\bar{V})_{spg}$	66-67	$(S)_{NV}$
20-21	$B \cdot BV_3$	44-45	$(B \cdot SL \cdot B\bar{V})_{spg}$	68-69	SEM (protons)
22-23	$(B \cdot B\bar{V})_{evg}$	46-47	$(B \cdot SH \cdot B\bar{V})_{spg}$	70-71	SPILLS
24-25	B_{spg}	48-49	$(B \cdot B\bar{V})_{evg}$	72-73	$(B104)_{spg}$
26-27	$B \cdot B\bar{V}_{spg}$	50-51	--	74-75	C_{spg}
28-29	B_{evg}	52-53	--	76-77	$B \cdot B_{D60}$
30-31	$\pi_{evg} = B \cdot \bar{B_V} \cdot S\bar{A}$	54-55	$(B \cdot P)_{evg}$	78-79	PCS
32-33	$(B \cdot S \cdot \bar{B}V)_{evg}$	56-57	S_{spg}	80-81	$(HV \cdot S)_{NV}$
34-35	$(B \cdot SD \cdot \bar{B}V)_{evg}$	58-59	SD_{spg}	82-83	TRIGS
36-37	$(B \cdot SL \cdot \bar{B}V)_{evg}$	60-61	SL_{spg}	84-85	ADC Gates
38-39	$(B \cdot SH \cdot \bar{B}V)_{evg}$	62-63	SH_{spg}	86-87	PC Resets

TABLE 3.3.--Sc

Scaler
$B \cdot S \cdot \overline{BV}_{evg}$ + $B \cdot SD \cdot BV_{evg}$ + $B \cdot P$
BDERR
$B \cdot \overline{BV}_{delay}$
$B \cdot S \cdot \overline{BV}_{evg}$
$B \cdot SD \cdot \overline{BV}_{evg}$
$B \cdot P_{evg}$
$\frac{B \cdot S \cdot \overline{BV}_{evg}}{B_{evg}}$
$HV \cdot S_{nv}/B_{spg}$
B_{spg}/SEM
B_{spg}/no. ofspil
B_{evg}/B_{spg}
$B_{spg}/B_{spg}(104)$
Average flux x # targets/cm2

TABLE 3.3.--Scaler Averages for a Single Run

Scaler	Interpretation	Average per run
$B \cdot S \cdot \overline{BV}_{evg}$ + $B \cdot SD \cdot \overline{BV}_{evg}$ + $B \cdot P$	Standard trigger	7838
BDERR	Branch driver errors	111.6
$B \cdot \overline{BV}_{delay}$	Effective incident flux	7.831×10^{7} μ's
$B \cdot S \cdot \overline{BV}_{evg}$	Single muon trigger	7383
$B \cdot SD \cdot \overline{BV}_{evg}$	Dimuon trigger	865
$B \cdot P_{evg}$	Pulser trigger	376.7
$\frac{B \cdot S \cdot \overline{BV}_{evg}}{B_{evg}}$	Event rate	$.90536 \times 10^{-4}$
$HV \cdot S_{nv}/B_{spg}$	Halo	102.53%
B_{spg}/SEM	μ/p yield	5.44×10^{-8}
B_{spg}/no. ofspills	Incident μ's per spill	$.50272 \times 10^{6}$
B_{evg}/B_{spg}	Dead time	46.56%
$B_{spg}/B_{spg}(104)$	Beam tune	68.38%
Average flux x # targets/cm^2	Average luminosity per run	2.0×10^{35} cm^{-2}

quality monit
line analysis
dead time, th
beam particle
there are seve
scalers must
too, are event
(except pulse
within a singl
good event. T
$\overline{\text{BVd}}$ signal (3
rate and defin
panied by an a
fully monitore
(cross section
presence of in
that acceptabl
(total trigs -
total trigs].

The DC
where each bit
fired, and 0 i
counters which
tion process b
spectrometer.
to work proper

quality monitors in the analysis, the most important scaler for off-line analysis is the flux [(B • $\overline{BV}$d)evg]. In an apparatus with no dead time, the flux of incident muons would be just the count of beam particles (i.e., the scaler for BEAM = B • C). In real life, there are several effects which must be accounted for: (a) the scalers must count only when the experiment is "live" meaning they, too, are event gated (e.g., Bevg); (b) since all of the triggers (except pulser) contain $\overline{BV}$, accidental counts or multiple beam muons within a single beam bucket (19ns) may sometimes inadvertently veto a good event. The flux can be corrected for this by forming a delayed $\overline{BV}$d signal (3 beam buckets after the trigger) to sample the accidental rate and defining flux = (B • $\overline{BV}$d)evg (i.e., all beam muons not accompanied by an accidental beam veto signal later). Flux was so carefully monitored because it must be known to determine absolute rates (cross sections). Further corrections to the flux account for the presence of incorrect (BDERR) and pulser triggers and the requirement that acceptable events have only one beam muon [correction factor = (total trigs - BDERR - pulser trigs - triggers with 0 or > 1 beam)/ total trigs]. The flux for each set of data is included in Table 3.4.

The DCRs used to record counter hits are shown in Table 3.5, where each bit of the original 16-bit PDP word is 1 if that counter fired, and 0 if not. The first two latches contain the trigger bank counters which were originally supposed to aid the track reconstruction process by signalling the path of the "live" muons in the spectrometer. However, the efficiency must be very high for this to work properly and, unfortunately, there were two problems with

TABLE 3.4.--Fl

Data Sample
270 GeV μ^+
Full Target
150 GeV μ^+
1/3 Target
270 GeV μ^-
Full Target

TABLE 3.4.--Fluxes for Data Samples

Data Sample	$(B \cdot \overline{BV}_d)$ evg	Corrected Flux
270 GeV μ^+		
Full Target	1.2834×10^{10}	1.0974×10^{10}
150 GeV μ^+		
1/3 Target	1.5915×10^{9}	1.3772×10^{9}
270 GeV μ^-		
Full Target	3.4457×10^{9}	3.0847×10^{9}

TABLE 3.5.--DC

Word	Bi
216	1-
	6-
	11-
217	1-
	6-
	11-
218	1
	2
	3
	4
	5
	6
	14
219	1-
	9-
220	1-
457	1
	2-
	12
	13
	14
	15

TABLE 3.5.--DCR Assignments

Word	Bits	Latch	Meaning
216	1-5	SAV	Vertically measuring (E26)
	6-10	SBV	Trigger bank counters
	11-15	SCV	
217	1-5	SAH	Horizontally measuring (E319)
	6-10	SBH	Trigger bank counters
	11-15	SCH	
218	1	B•P	
	2	B•S•$\overline{BV}$	Trigger Bits
	3	B•SD•$\overline{BV}$	
	4	B•SL•$\overline{BV}$	
	5	B•SH•$\overline{BV}$	
	6	π	
	14	PC Reset	Reset for PC Latches
219	1-8	E98 BH 2	E98 Beam
	9-16	E98 BH 3	Hodoscope Counters
220	1-8	E98 BH 4	
457	1	PC Strobe	Enable for PC Latches
	2-9	TH	Target Hodoscope
	12	STEL	Efficiency Telescope
	13	BV 1	
	14	BV 2	Beam veto counters
	15	BV 3	

the DCRs duri

criminators w

seem ineffici

meaning that

trigger may s

since their r

used only qua

halo from live

The ne

and PC start s

hoped that one

selecting ever

trigger banks

tive. Again,

certain small

Since

hodoscope latc

ever, were vit

information ne

tion of DCR an

events having

least until th

described in S

Spark

stitute a set

each of the 36

the DCRs during part of the running: (a) the thresholds on the discriminators were set too high for some of the DCRs making the counters seem inefficient; (b) gate widths were too wide for part of the runs meaning that muons passing through counters well after (40-50ns) the trigger may still set the latches (especially for the beam vetos since their rate is very high). Thus, the trigger bank DCRs were used only qualitatively for special (multimuon) events to separate halo from live muons.

The next latch contains information on the types of trigger and PC start signals generated for the event. Initially, it was hoped that one could find multimuons, or high q^2 events, by simply selecting events with those triggers, but the geometry of the trigger banks and inefficiency in the latches have made this ineffective. Again, these trigger hits were used in a qualitative manner on certain small event samples.

Since multiple beam events were not analyzed, the target hodoscope latch has been largely ignored. The last two latches, however, were vitally important since they contain the beam hodoscope information needed to determine incident muon momentum. A combination of DCR and counter inefficiency contributes to ~10% of the events having insufficient information to determine beam momentum (at least until the E98 PCs were fixed). The algorithm for this is described in Section 3.3.

Spark chamber time digitizer readings (words 465-761) constitute a set of eight integers (most of which are usually 0) for each of the 36 wands (four views for each of nine chambers). At

least one (usu

whose spatial

readings were

1000 triggers.

propagation al

the analysis r

digitizer read

and v = (y - x

X = al

R = (s

f

The only diffi

sparks (neighb

sparks being b

being so close

assigning a si

The co

to some arbitr

as the center

coordinates mu

cated by the m

and the preser

degaussed (see

relatively unc

were aligned u

least one (usually two) of the integers represent fiducial sparks, whose spatial position is accurately known and whose time digitizer readings were determined for each run by averaging the values over 1000 triggers. Using this correspondence (and the known speed of propagation along each wand wire if only one fiducial is available), the analysis routine (LLWANDS) must convert the rest of the time digitizer readings into spatial coordinates x, y, $u = (x + y)/\sqrt{2}$, and $v = (y - x)/\sqrt{2}$ via the formulae:

$$X = \text{alignnment} \pm (\text{chamber } 1/2 \text{ width}) \times (1 - 2R),$$

$$R = (\text{spark integer} - \text{1st fiducial})/(\text{2nd fiducial} - \text{1st fiducial})$$

The only difficult part of this process is handling clusters of sparks (neighboring wires hit). Since these tend to occur due to sparks being between wires far more often than actual particle tracks being so close (.7 mm), we chose to simply average clustered sparks, assigning a single spark to the midpoint.

The coordinates of the sparks were initially found relative to some arbitrary axis shifted and rotated from our true axis (taken as the center of the toroidal magnets). Thus, the spark chamber coordinates must be aligned to this magnet axis. This was complicated by the magnetic field and multiple scattering in the toroids and the presence of the massive iron target. So the magnets were degaussed (see Chapter 2) and the target removed, giving muons a relatively unobscured passage through the chambers. The front four were aligned using straightahead muons from run 130 (the proportional

chambers were
the back five
retain memory
out of the cen
the front four

The ac
chambers rela
projected into
actual and pre
scattering in
statistics to
each chamber
coordinates an
by-view basis
matched coord
see Figure 3.
aligned relat
axis. This f
magnets and th
Section 3.5 an
a shift or ro
opposite quadr
calibration ru
rotated (real
rants all bala
final alignmen

chambers were also aligned with this data, see Figure 3.1). However, the back five spark chambers were deadened in the center so as not to retain memory of "stale" beam tracks. The beam had to be deflected out of the center (by the 104 dipoles) to align these chambers with the front four. Runs 113-120 provided muons for this purpose.

The actual alignment procedure began by aligning all of the chambers relative to each other. Straight lines in one group were projected into another set of chambers and the difference between actual and predicted spark positions histogramed (note that multiple scattering in the magnets smears these distributions requiring high statistics to determine the mean). The means of the histograms in each chamber being aligned were then subtracted from actual spark coordinates and the procedure was iterated. This was done on a view-by-view basis. Alignment of the separate views required histogramming matched coordinates (e.g., actual x minus calculated $x = (U-V)/\sqrt{2}$; see Figure 3.2). The completion of this procedure left all chambers aligned relative to each other, but still not fixed to the magnet axis. This final step exploited the cylindrical symmetry of the magnets and the full momentum fitting algorithm (to be described in Section 3.5 and Appendix B). Since the field varied only radially, a shift or rotation of axis causes momentum differences between opposite quadrants for the mono-energetic muons of the spectrometer calibration runs (also Section 3.5). Thus, the axis is shifted and rotated (really just changes in alignment constants) until the quadrants all balance to the same mean momentum (within 2-3%). The final alignment constants are shown in Table 3.6.

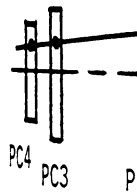

Fi

F

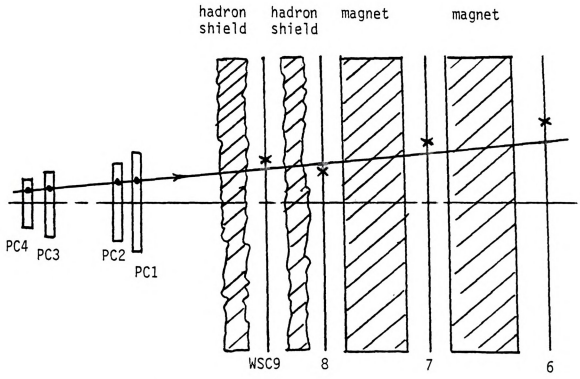

Figure 3.1 Aligning PC2,PC1, and the front spark chambers

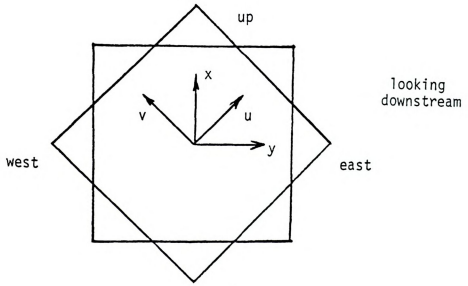

Figure 3.2 Conventions for spark chamber coordinate axes

WSC 1

2

3

4

5

6

7

8

9

E319 PC 1

2

3

4

5

Table 3.6

Final E319 Alignment Constants in cm.

Wands

		x	y	u	v
WSC	1	.211	.742	.953	.521
	2	.324	.557	.508	.148
	3	.111	.611	.663	.391
	4	.341	.606	.375	.136
	5	.034	.190	.429	.189
	6	.140	.069	.036	-.142
	7	-.124	.057	.144	.122
	8	-.020	.206	.255	.316
	9	-.034	1.122	.590	.327

		x	y
E319 PC	1	0.637	0.688
	2	1.073	-0.115
	3	0.438	0.324
	4	-0.090	1.284
	5	0.151	1.918

E398 PC	1	0.0
	2	0.054
	3	0.476
	4	0.0
	5	-0.435
	6	0.0

Sever

dure. Firstl

alignment anc

the algorithr

field of 100-

line of up to

reconstructio

slightly diff

shifts of up

must be consi

The

sisted of a s

wires. The d

the correct o

were unnecess

the wire spac

spatial coord

X = A

P

Again, the cl

All of the ex

manner to this

of planes, so

E319 PCS since

Several potential problems exist with this alignment procedure. Firstly, the chambers worked rather erratically for the early alignment and calibration runs with extra sparks possibly misleading the algorithms. Also, the degaussed magnets still carried a residual field of 100-200 Gauss which could cause deviations from a straight line of up to 2mm if all the fields were aligned. Finally, the old reconstruction and momentum fitting routines used for alignment give slightly different momenta than the final algorithm. Thus, alignment shifts of up to 2mm are possible and their effect on data analysis must be considered.

The latched proportional chamber wires (words 88-215) consisted of a sequence of 1's and 0's corresponding to hit and missed wires. The decoding routines index the wires to their chambers in the correct order and then search each chamber for hits. Fiducials were unnecessary here since each wire has its own unique latch, and the wire spacing is accurately known. Hit wires were converted into spatial coordinates according to the formula:

$$X = \text{Alignment} + (\text{wire spacing}) \times (\text{hit wire number}) - \text{PC } 1/2 \text{ width}$$

Again, the cluster ambiguity was resolved by averaging the positions. All of the experiment's proportional chambers are handled in the same manner to this point. However, the chambers have different numbers of planes, so that matching to produce x-y coordinates (only done for E319 PCS since the x planes of the E98 PCS were not used) was

different fo
thermore, th
difficult fo
were aligned
with the tar
alignment pr
removed at t
at the front
(363) with a
1E4 dipoles
runs could a
upstream. Da
timed correct
The final co

The f
Each of the 2
which is a me
entering the
was proportio
calorimeter c
used. After
application o
ings are stor
(note that th
consecutive a
the ADC algor

different for each chamber (Figure 3.3 details the matching). Furthermore, the long distances separating the various PCs made alignment difficult for some of the chambers. The downstream E319 PCs (1 → 4) were aligned along with the front four spark chambers using run 130 with the target removed (note that any two chambers can start the alignment process since arbitrary initial shifts or rotations were removed at the final step of pinning the axis to the magnets). PC5 at the front of the Muon lab was aligned using a regular data run (363) with all E98 absorbers out of the way. Since the field in the 1E4 dipoles (and their bend angle) was accurately determined, data runs could also be used to align the E98 proportional chambers upstream. Data from the final runs when the E98 PCs were finally timed correctly, was used to align both these and the beam hodoscopes. The final constants are listed in Table 3.6.

The final decoding task involves the ADCs (words 229-456). Each of the 220 ADC words contains a single integer channel number which is a measure of the total charge (pulse amplitude times width) entering the ADC during the 100 ns gate time. This charge itself was proportional to the number of particles passing through the calorimeter counter for that ADC scaled by the gain of the amplifier used. After correction for the zero (pedestal) level of the ADCs and application of muon and hadron shower calibration data, the ADC readings are stored in their correct order from upstream to downstream (note that the first counter uses ADC words 324,325 and the rest are consecutive around this gap on the primary tapes). Full detail on the ADC algorithms and calibration is supplied in Appendix A.

PC3

$u = -y$

$w = (\sqrt{3}\,x + y$

$v = (y - \sqrt{3}\,x$

$u + v + w = 0$

PC4

$u' = x$

$w' = (\sqrt{3}\,y -$

$v' = -(x + \sqrt{3}$

$u' + v' + w'$

Figure 3.3.--

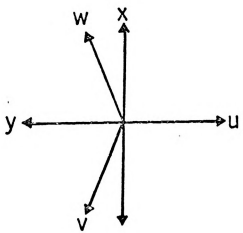

PC3

$u = -y$

$w = (\sqrt{3}\, x + y)/2$

$v = (y - \sqrt{3}\, x)/2$

$u + v + w = 0$

$x = (w-v)/\sqrt{3}$

$y = (v + w - u)/2$

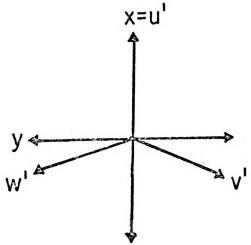

PC4

$u' = x$

$w' = (\sqrt{3}\, y - x)/2$

$v' = -(x + \sqrt{3}\, y)/2$

$u' + v' + w' = 0$

$x = (u' - v' - w')/2$

$y = (w' - v') / \sqrt{3}$

Figure 3.3.--E319 Beam Proportional Chamber Matching Conventions.

3.3 Beam Tra and Momentum

Once

mation conver

of the muon s

momentum vect

ability to de

advantages en

procedure beg

using the E31

projected ups

scopes from w

dent muon ana

Given

stage, subrou

tracks in the

quality of tr

points (i.e.,

At least two

points. (Note

views must be

correct.) Alt

single view or

summarizes the

that PC5 hits

3.3 Beam Track Reconstruction and Momentum

Once the event tapes are fully decoded and the detector information converted to usable form (spatial coordinates), the kinematics of the muon scattering event must be determined by reconstructing the momentum vector for all muons (incident and final-state). Indeed, the ability to determine the incident muon kinematics is one of the great advantages enjoyed in muon (as opposed to neutrino) experiments. The procedure begins by determining the beam track (positions and angles), using the E319 beam PCs (numbers 3 through 5). The tracks are then projected upstream through the 1E4 dipoles to the E98 PCs and hodoscopes from which the beam energy can be found, completing the indident muon analysis.

Given matched points (x, y coordinates) from the decoding stage, subroutine BEAMPC attempts to form all possible straight line tracks in the beam chambers. An important factor in determining the quality of track candidates is the match code of the contributing points (i.e., the number of views which are included; see Figure 3.3). At least two views must have hits for PC3 and PC4 to form matched points. (Note that if any view has more than one hit, all three views must be used to remove ambiguity about which of the hits is correct.) Although this holds for PC5 as well, sometimes only a single view or even no hits are allowed in this chamber. Table 3.7 summarizes the method and the types of beam tracks allowed. Note that PC5 hits must lie within a window of the projected line from

TABLE 3.7.--B

De PC
Ma
Form x PC 3 a
Project Search
Fit 3 found
Cut li beam ar
1st Pas
2nd Pas

TABLE 3.7.--Beam Track Algorithm

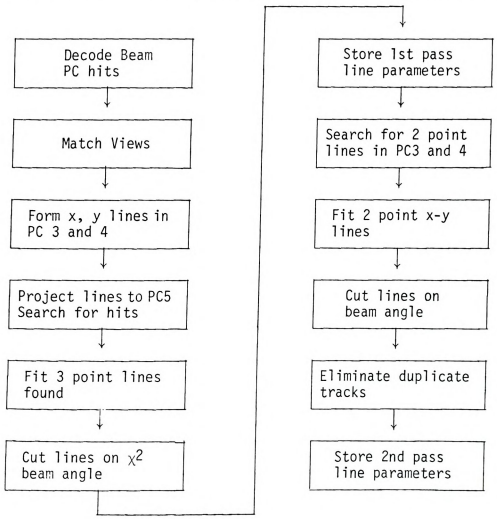

Match Code Combinations (PC3, PC4, PC5)

1st	(3,3,2)	(3,3,1)	(3,2,2)	(3,2,1)
Pass	(2,3,2)	(2,3,1)	(2,2,2)	(2,2,1)
2nd	(3,3,0)	(3,2,0)	(2,3,0)	(2,2,0)
Pass	2 point matches allowed if 1 hit in both views			

the downstrea

caused by th

Afte

dimensional

ithm, which

(actually in

PCs contribu

$\lesssim$ 10 mr) are

usually appl

intercepts a

vertex deter

finding. The

allowed us t

problems invo

Now

(which is the

magnetic fie

upstream E98

Referring to

gerated bend

downstream mu

is clear that

$R(\theta_2^2 - \theta_1^2)$

cosine funct

$\theta_2 = \frac{L}{R} - \theta_1$,

the downstream PCs, whose size is determined by an extrapolation error caused by the wire spacing.

After all lines have been found, they are fitted in the two-dimensional planes (x-z and y-z) by a standard straight line algorithm, which returns the slopes and intercepts at the z=0 point (actually inside the calorimeter) and a chi-squared (X^2) if all three PCs contribute. Very generous beam cuts ($X^2/DOF \leq 5$, beam angles $\leq$ 10 mr) are made to eliminate obvious bad tracks (stricter cuts are usually applied later in analysis). The matched points, angles, and intercepts are then stored (in common blocks) for later use in vertex determination. Table 3.8 gives statistics on the beam track finding. The high rate of success in finding a single beam track allowed us to ignore other events, avoiding the difficult vertex problems involved with 0 or more than 1 beam muons.

Now with the beam track angle and intercept in the y-z plane (which is the direction of bend in the 1E4 dipoles), the measured magnetic field and position of the magnets, and the hits in the upstream E98 PCs and/or hodoscopes, the beam energy can be calculated. Referring to the geometry of Figure 3.4 (which shows a highly exaggerated bend angle and a slightly simplified situation where the downstream muon leaves at the center of the magnet for clarity), it is clear that, for small angles, $L = R(\theta_1 + \theta_2)$ and $h = 1/2\ R(\theta_2^2 - \theta_1^2)$ from trigonometry and the usual expansion of sine and cosine functions. We solve for the two unknowns $h = L(\frac{L}{2R} - \theta_1)$, $\theta_2 = \frac{L}{R} - \theta_1$, where θ_1 is the measured downstream beam angle and L/R

TABLE 3.8 --Beam Statistics

TABLE 3.8.--Beam Statistics

	270 GeV μ^+		270 GeV μ^-		150 GeV μ^+	
	Typical Run	%	Typical Run	%	Typical Run	%
Beam Track Statistics						
No beam track	465	4.8	186	2.1	249	2.6
1 beam track	8684	90.4	8211	94.2	8783	92.3
> 1 beam tracks	463	4.8	323	3.7	484	5.1
Beam Energy Statistics						
E0 not found	552	6.5	78	1.1	1159	13.7
E0 from E98 BH	7979	93.5	821	11.4	7274	86.3
E0 from E98 PC	0	0.0	6271	87.5	0	0.0

$\underline{h}$ ξ-

For s

For t

A_i =

Figur

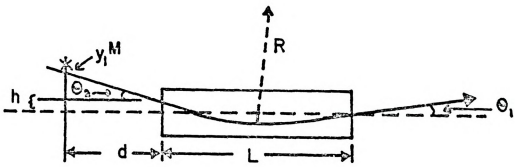

For single upstream detector, $P = \dfrac{A_1}{B_1\theta_1 + y_1^m}$

For two upstream detectors, $P = \dfrac{A_1^2 + A_2^2}{A_1 y_1^m + A_2 y_2^m + \theta_1(A_1 B_1 + A_2 B_2)}$

$A_i = .03BL\ (\frac{L}{2} + d_i)$ $\quad B_i = L + d_i$

Figure 3.4.--Beam Momentum Determination (Using detectors di Upstream of the E104 Dipole, Magnets of length L and Radius of Curvature R) and beam Track (θ_1) downstream.

is the supp

ratio can b

verse momen

in the magn

located at

tion is y_i

Forming a c

tors of ter

of each det

momentum eq

pendent che

analysis us

actual spar

Gaussian of

confidence

other combi

First, only

tracks in t

1E4 and pro

agreed to w

smaller for

E98 chamber

with beam e

bers were u

BHs were wo

is the supplementary angle to the bend (28.6 mr) in the magnets. This ratio can be expressed in terms of the momentum P = .03 BR and transverse momentum kick $\Delta P_\perp$ = .03 BL; that is L/R = $\Delta P_\perp$/p (B is the field in the magnets which determines $\Delta P_\perp$). Then for an upstream detector located at $z_i = -(L + d_i)$, the predicted coordinate in the bend direction is $y_i = \frac{A_i}{P} - B_i\theta_1$, where $A_i = \Delta P_\perp (\frac{L}{2} + d_i)$ and $B_i = L + d_i$. Forming a chi-squared, consisting of the sum over all upstream detectors of terms like $(y_i - y_i^m)^2/\sigma_i^2$ (where σ_i is the measurement error of each detector), and minimizing with respect to 1/p yields beam momentum equations shown in Figure 3.4. Although there was no independent check on beam energy (except possibly for missing energy analysis using the calorimeter), the shape of the predicted minus actual spark distribution in the upsteam PCs in consistent with a Gaussian of width appropriate to the chamber resolution, giving us confidence in this method. Using the same type of algorithm, two other combinations of chambers were tried as a test of the alignment. First, only the three E98 PCs or BHs were employed without beam tracks in the E319 PCs. Secondly, lines were found first upsteam of 1E4 and projected into the downstream chambers. All of these methods agreed to within 1/2% on the mean energy. The spread was somewhat smaller for the latter two, but the inefficiency of the downstream E98 chambers and hodoscopes caused a 25% loss in number of events with beam energy, as opposed to only a 10% loss when the E319 chambers were used to get the downstream track. When both the E98 PCs and BHs were working (after run 480), the efficiency increased to 99%.

Here it was

determined

again they

width of the

because they

Table 3.8 su

energy canno

the approxim

3.4 Spectro Reconstruct

Wit

cult task of

state muons,

Two indepen

already exis

spectrometer

that simply

would make t

using VOREP

quickly beca

the old prog

dimuons foun

the problems

end) of the

sides will n

Here it was also possible to check agreement between beam energy determined from hodoscopes versus that from proportional chambers and again they checked to within about 1/2% in the mean (although the width of the distribution is considerably larger for the hodoscopes because they are 3/4" wide, while the PC wire spacing is 12 per inch). Table 3.8 summarizes beam energy statistics. Note that when the beam energy cannot be found, further analysis assumes it to be 270 GeV, the approximate mean of the distribution.

3.4 Spectrometer Track Reconstruction

With the incident muon kinematics determined, the more difficult task of reconstructing and finding the momentum of all final-state muons, using the magnetic spectrometer, could be undertaken. Two independent track reconstruction programs (VOREP and RECON) already existed from the E26 experiment,[3] which used the same spectrometer elements as E319. So the initial assumption made was that simply reconfiguring the geometry numbers in these programs would make them effective for analysis. Partial success was enjoyed using VOREP on the single muon scattering reconstruction, but it quickly became apparent that either E319 had no multimuons or that the old programs could not find them. A little thought, and a few dimuons found by visual scanning of events, quickly revealed some of the problems: (a) The E26 programs start at the back (downstream end) of the spectrometer, meaning that tracks which escape out the sides will never be found; (b) With all eight magnets powered for

E319 as opp
penetrate t
(c) the lon
frequently
programs, w

Thu
struction p
which would
I developed
labeled PAS
multimuons,

1.
apparatus,
applicable
similar to

2.
was found t
and has bee
results (e.

As
its track s
muons escap
chambers be
and spark c
well). The

E319 as opposed to three in E26, tracks were much less likely to penetrate to the back chambers (especially those which bent outward); (c) the long target in E319 allows low-angle tracks to participate frequently in triggering and these were usually not found in the E26 programs, which were developed with a small angle cut in mind.

Thus, a clear need existed for a uniquely E319 track reconstruction program designed principally to find multimuon events and which would make much better use of the front part of the spectrometer. I developed this program, called MULTIMU, in two distinct stages, labeled PASS1 and PASS2. Since both were used to find samples of multimuons, I will describe each in turn. Two notes here:

1. While MULTIMU was written specifically for the E319 apparatus, the spark search and matching algorithms are generally applicable to any magnetized iron spectrometer and were conceptually similar to those used in RECON.

2. Although early single muon analysis used VOREP, MULTIMU was found to possess much higher efficiency especially at low q^2 and has been used for the most recent deep inelastic scattering results (e.g., in the thesis of R. Ball).[4]

As described above, the multimuon program would have to begin its track search at the front of the spectrometer to be able to find muons escaping out the sides or into the toroid holes. The only chambers before the first magnet are the hadron proportional chambers and spark chambers 9 and 8 (neither of which worked particularly well). The removal of the other two front chambers (7 and 6) to

within the
original PA
chamber (ev
only low en
after one m
line combin
WSC 9 and W
These were
sparks were
three point
on its slop
HPCs (whose
chambers).
likely trac
tracks. Si
of multimuo
analysis, a
no attempt
The output
flagging mu
by visually
Section 3.6

Whi
a sample of

within the spectrometer made front line finding more difficult. The original PASS1 approach compromised by including chamber 7 as a front chamber (even though it was behind one magnet) on the premise that only low energy tracks would severely deviate from straight lines after one magnet. The algorithm was programmed to form all possible line combinations in each view, using either the HPC and WSC 9, or WSC 9 and WSC 8 to preserve efficiency if one of the three failed. These were all projected into WSC 7, where a window was opened and sparks were searched for. If found within the window, the resulting three point line was fit and subjected to two different sets of cuts on its slope, intercept, vertex, and whether it was "live" in the HPCs (whose memory time is ~120ns as opposed to 1μs for the spark chambers). The "narrow" set of cuts was presumed to contain the most likely track candidates and the "wide" cuts to contain all possible tracks. Since the main purpose of PASS1 was to verify the existence of multimuons and begin to develop a sample which would guide further analysis, a large fraction of the main μ^+ data runs were analyzed with no attempt to continue the track search further into the spectrometer. The output of PASS1 was merely two lists of run and event numbers, flagging multimuon candidates. Further event finding was performed by visually scanning the events which passed the "narrow" cuts (see Section 3.6 for a description of this procedure).

While the first stage version of MULTIMU successfully found a sample of multimuon events, the scanning revealed many obvious

deficiencie
energy cut
insufficier
bers; (3) t
chambers ca
dimensional
well withou

The
to reduce i
tate actual
events four
program, ir
events was
front line
was expande
a time) of
method (#4)
Then, in or
Method 2 (w
lines are s
shows the a
to each oth
and interce
developed t
all possibl

deficiencies: (1) the windows opened in WSC 7 constituted a 16 GeV energy cut on muons; (2) the redundancy of line finding was still insufficient to overcome the inefficiency of the front spark chambers; (3) the prevalence of halo and stale beam tracks in the front chambers caused far too many accepted lines, mostly because the two-dimensional vertex routine cannot discriminate against halo very well without losing good tracks.

The second stage reconstruction program PASS2 was developed to reduce inefficiencies in finding multimuon events and to facilitate actual kinematic determination for these events. The multimuon events found in PASS1 were constantly used as tests of the evolving program, insuring good efficiency (Run 280 with eight good dimuon events was especially helpful in this regard). PASS2 begins with front line finding in each view, like PASS1. However, the method was expanded to use all four different combinations (taken three at a time) of the HPCs and the front three spark chambers. The preferred method (#4) was only HPC, WSC9, and WSC8, giving true straight lines. Then, in order of preference, came method 1 (HPC, WSCS 9 and 7), Method 2 (WSCS 9, 8, 7) and Method 3 (HPC, WSCS 8, 7). All of these lines are subject to the same kinds of cuts as in PASS1 (Table 3.9 shows the actual cuts applied) and are sorted by method and compared to each other with duplicates, having essentially the same slope and intercept, eliminated. The lines are then sent to the newly-developed track reconstruction routines (controlled by TRYMAT) where all possible combinations of lines between two views are formed.

TABLE 3.9.-

A. Two dim

1. Slo

2. Lin

3. Ver
str

4. Win

5. HPC

B. Vertex

1. DMI

2. -25

3. |Z

C. Track c

1. χ^2/

2. DOF

3. BCO

4. IRA

5. At

TABLE 3.9.--PASS2 Cuts

A. Two dimensional line cuts

1. Slopes $\leq .234$
2. Line passes within target volume
3. Vertex within 2330 cm upstream of front and 1930 cm downstream of back of target
4. Window at WSC 7 = $\pm$ $5 \times 10^4 x^2 + .165x + 0.5$ ($x \leq 50$ cm)
   10 cm ($50 < x \leq 75$ cm)
   20 cm ($x > 75$ cm)
5. HPCs must register if track projects through them

B. Vertex cuts (3-dimensional)

1. DMIN $\leq$ $.15r + 2.0$ $r \leq 53$ cm
   10 $r > 53$ cm
2. -250 cm $\leq$ ZMIN $\leq$ 600 cm
3. $|$ZMIN - ZADC$| \leq$ 400 cm if shower found

C. Track cuts

1. $\chi^2/DOF \leq 10$
2. DOF $\geq$ 2 (at least 1 back chamber has spark)
3. BCODE $\geq$ 2.8
4. IRAD $\geq$ 1 ($\geq$ 1 of the back 7 chambers out of hole)
5. At least 1/2 of the chambers searched must have sparks

There are
line in a
combinati
intercept
struction,
vertex wi
approach
resulting
verse DMI
are subje
the target
track reco
shower, a
closest to
are also d

No
back into
varying ma
iron toroi
This is a
field dist
the probab
spread out
tracing ap
expansion

There are six view combinations (UV, YV, XV, YU, XU, XY) allowing a line in any view to participate in up to three of them. Each such combination constitutes a potential track and its line slopes and intercepts (at WSC 8) are stored. Before attempting further reconstruction, however, each candidate has its full three-dimensional vertex with the beam track calculated via the distance of closest approach method (described more completely in Appendix B). The resulting vertex consists of a longitudinal ZMIN point and a transverse DMIN measure of distance of closest approach. Both of these are subjected to strict cuts which insure a good vertex (located near the target) and provide a very strong rejection of halo before the track reconstruction proceeds further. When the calorimeter finds a shower, a cut is also made on ZADC-ZMIN so that the tracks pointing closest to the actual interaction point are selected. These cuts are also detailed in Table 3.9.

Now the matched front line track candidates must be traced back into the magnetic spectrometer, taking account of the radially varying magnetic field and energy loss and multiple scattering in the iron toroids, in order to predict where sparks will be in the chambers. This is a very difficult problem in general, especially because the field distorts the symmetric multiple scattering distribution causing the probability of finding the track in the back chambers to be spread out asymmetrically and over a broad area. The method for tracing approximates the magnets as single bend points and uses an expansion of the complicated coordinate functions in the variable 1/P

up to 2nd

dix B.

At

NSC 7 is r

with all 1

opened abo

reflecting

and chambe

opened in

sparks wer

using the

necessary

sparks con

is availab

detailed e

appearing

if within

deadened re

Hou

around the

lated devia

correlation

a distincti

searched ar

(the actual

up to 2nd order. This algorithm is described in detail in Appendix B.

At each of the seven remaining spark chambers (note that WSC 7 is now properly re-considered as a true spectrometer chamber, with all lines defined at WSC 8), a spark search window must be opened about the predicted muon position, with the size of this window reflecting multiple scattering and measurement errors in all magnets and chambers upstream. Initially simple rectangular windows were opened in each chamber to obtain sparks in all four views. These sparks were matched to form all possible three-dimensional points using the routines SMAT and UVXY2. Very complicated indexing was necessary to determine which sparks were available and how many sparks contributed to each point (the match code). Further detail is available in Appendix B. The matching window (set to 1.2 cm by detailed event studies) effectively eliminates extraneous sparks appearing in only a single view. Note that sparks are matched only if within the active areas of the chambers (not within the supposedly deadened region of the last five WSCs).

However, although measurement errors simply contribute circles around the predicted positions, multiple scattering causes correlated deviations, due to the presence of the magnetic field. Such correlations dictated the formation of another, smaller window with a distinctive hourglass shape, in order to minimize the area to be searched and maximize the probability of selecting the correct spark (the actual algorithm in subroutine SELECT is again discussed in

Appendix

quite lar

results i

spark cha

with good

cuts to p

"bad" spa

down and

WSC6 was

higher ra

if: (a)

(b) no sp

then too

call that

beyond wh

spark pass

position w

an estimat

tion proce

This momen

chamber (n

magnet and

The algori

multimuons

track has

Appendix B.) Note that the simple rectangular windows have to be quite large to insure good spark finding efficiency and this often results in finding extraneous sparks (which are always present in spark chambers). The hourglass window rejects these incorrect sparks with good efficiency. Each selected point was subject to several cuts to protect the developing track from veering off course due to "bad" sparks. This was particularly important at WSC6 due to breakdown and stale beam sparks primarily in the middle; so the spark at WSC6 was required to be out of the magnet holes or at least at a higher radius than that at WSC 7. Further spark search is terminated if: (a) the radius of the projected track exceeds the magnet radius; (b) no sparks were found in two consecutive chambers (because it is then too easy to mistakenly connect segments in front and back and call that a track); or (c) the track crosses the spectrometer axis beyond which the tracing routines cannot follow it. If more than one spark passed the cuts, the spark closest to the predicted track position was used. At each chamber, the single chosen point allows an estimate of the track momentum using a simple chi-squared minimization procedure (subroutine RCFIND and CHIS discussed in Appendix B). This momentum was used to update the predicted positions in the next chamber (note that the final estimate was obtained after the last magnet and used to predict positions in the back three spark chambers). The algorithms have been checked visually for many events (including multimuons) and were able to follow tracks quite closely. After the track has been located in all seven back spark chambers (or lost

along the

sparks we

searched

for the b

fields, t

multiple

Points we

Although

and good

Fu

in Table 3

out also

criteria s

sparks agr

an indicat

describes

back seven

(frequentl

erly matche

track is ou

meter. An

was develop

of similar

candidates

of front li

along the way), the front chambers (WSC 8, 9, and HPCS), from which sparks were already found in views to give front lines, are again searched for sparks. This time the method used is the same as that for the back chambers, although now, in the absence of magnetic fields, the search windows can be simple squares consistent with multiple scattering in the hadron shields and measurement errors. Points were matched in exactly the same way as in the back chambers. Although somewhat inefficient, this procedure insures consistency and good connection between front and back parts of the track.

Further cuts were then made on the complete track as shown in Table 3.9. Developed empirically to reject "junky" tracks without also losing good ones, these cuts all involve track "goodness" criteria such as: (1) chi-squared, which tells how well the actual sparks agreed with predicted positions, (2) degress of freedom (DOF), an indication of how many chambers contributed, (3) DMIN, which describes vertex quality, (4) BCODE, the average match code in the back seven chambers, telling how many views normally contributed (frequently tracks with mostly two point matches are halo or improperly matched track segments) and (5) IRAD, which insures that the track is outside of the hole (15.24 cm) somewhere inside the spectrometer. An overall quality factor $QF = \frac{BCODE}{4} + \frac{DOF}{10} - \frac{X^2}{10(DOF)} - \frac{DMIN}{10}$ was developed to choose the best representative of the large number of similar (x and y positions within 2 mm at half the chambers) track candidates (due to the great redundancy in matching all combinations of front lines). After the final sorting of tracks (subroutine

TROUT),
onto out
are writ
muon can
event nu
In the n
along wi
ciencies

3.5 Spec
Fitting

T
each fina
energy wa
vector fo
squared w
[momentum
parametri
resolutio
to arrive

T
FINAL) wa
changes i
track was
very simi
positions

TROUT), only nonidentical tracks should be left and these were written onto output tapes in the format of Table 3.10. Note that all tracks are written out, even if they are not multimuons. Potential multimuon candidates (more than 1 reconstructed track) have their run/event numbers flagged on a separate file for later visual scanning. In the next two sections, the momentum analysis of these tracks along with the multimuon finding procedures and reconstruction efficiencies will be discussed.

3.5 Spectrometer Track Momentum Fitting

Track reconstruction determines the position and angles of each final state muon at the end of the target. However, the muon energy was only estimated in MULTIMU. To obtain the full momentum vector for the muons requires fitting the track, by forming a chi-squared which is a function of the five independent variables [momentum p, x and y angles (θ_x, θ_y) and intercepts (x_o, y_o)] that parametrize the muon. This chi-squared, accounting for all chamber resolution and multiple scattering correlations, is then minimized to arrive at the final values of the momentum vector.

The momentum fitting program used for this experiment (called FINAL) was quite similar to that of E26, although several algorithm changes improved its range of applicability. After the reconstructed track was read from the secondary tapes, a tracing routine (TRACE), very similar to that used in reconstruction, generated predicted positions in the chambers and a momentum estimate was obtained (in

TABLE 3.1

Word	
1	Run
2	Tra
3	Flu
4-6	PC5
7	# S rec
8-17	HPC-
18-20	PC5-
21	Blar
22-31	HPC-
32	Blar
33-42	HPC-
43	Blar
44-45	HPC-
46	WSC8 if f
47	WSC7 if f
48-53	WSC
54-56	Beam (P_{ox}
57-58	Beam (xo,
59-61	Trac (Px,
62-63	Trac (x,

TABLE 3.10.--Secondary Tape Format

Word	Content	Type	Word	Content	Type
1	Run x 100000 + Event	I	64	Chi-squared χ^2	R
2	Track Number	I	65	Degrees of Freedom (DOF)	R
3	Flux	I	66	ZADC (= -1024 if not single showers)	R
4-6	PC5-3 x Coord.	R	67	E_{Hadron} (summed over all showers)	R
7	# Sparks manually reconstructed	R	68-71	Track (x,y) slopes and intercepts	R
8-17	HPC-WSC1 x Coord.	R	72	2nd spark chamber pulled if necessary	R
18-20	PC5-3 y Coord.	R	73	1st spark chamber pulled if necessary	R
21	Blank	R	74	# HPC hits (packed)	I
22-31	HPC-WSC1 y Coord.	R	75	# WSC sparks (packed)	I
32	Blank	R	76	Match codes PCS (packed)	I
33-42	HPC-WSC1 x fitted	R	77	# Spectrometer Tracks	I
43	Blank	R	78	# Beam tracks	I
44-45	HPC-WSC9 y fitted	R	79-83	DCRS 1, 2, 3, 4, 6	I
46	WSC8 y fit → -1024 if fit failed	R	84	BCODE	R
47	WSC7 y fit → 0.0 if fit failed	R	85	DMIN	R
48-53	WSC 6-WSC 1 y fitted	R	86	ZMIN	Rs
54-56	Beam momentum (P_{ox}, P_{oy}, P_{oz})	R	87-88	Accepted, found lines/ view	I
57-58	Beam pos. z=0 (xo, yo)	R	89	Chamber where track leaves spectrometer	I
59-61	Track momentum (Px, Py, P_z)	R	90	WSC match codes (packed)	I
62-63	Track pos @ Z=0 (x, y)	R	91-150	Packed ADCS	I

the same
chi-squa
were form
(CHIF) se
the weigh
measureme
each cham
chambers
initial m
the deriv
to zero,
detailed
the momen
values of

Th
ized in Ap
squared ar
events (pa
is the abi
chi-square
rect spark
instead of
for each e

Ca
by compari

the same manner as in MULTIMU; see Appendix B). Then the rigorous chi-squared definitions (which take full account of correlations) were formed for the back seven chambers (CHIB) and the front three (CHIF) separately (Appendix B). The total chi-squared (CHI2) was the weighted sum of these two with weights determined by the average measurement error in front (.2 cm) versus back (.1 cm). Note that each chamber should really be assigned a separate value, but the chambers are quite similar. Once the chi-squared was formed for the initial momentum guess, minimization was accomplished by calculating the derivatives of CHI2 with respect to each parameter, setting them to zero, and solving for the five parameter changes required (again detailed in Appendix B). The entire procedure was iterated until the momentum changes were less than 1%. The final fitted sparks and values of the five parameters were written on the secondary tapes.

The algorithm changes made in these FINAL routines (summarized in Appendix B) were developed by detailed study of the chi-squared and parameter varying routines for individual, difficult events (particularly extreme energies). The most important of these is the ability to remove up to two "bad" sparks from the fit if the chi-squared was too large. So even if reconstruction selects incorrect sparks, the track was usually preserved and fit adequately instead of being cut. Sparks pulled were flagged on the output tape for each event.

Calibration of the momentum fitting algorithm was determined by comparison to special data calibration runs and to Monte Carlo

predicti
this pur
spread i
(called
beam pro
Cyclotro
cases, i
these ru
obstructi
PCs are g
determine
and beam
into the
the targe
and energ
The metho
struction
for the m
of the la
as possib
grammed (
scatterin
of the in
the spectr
these dist

predictions. There were two sets of data taken specifically for this purpose, in which the iron target was removed and the beam was spread into the spectrometer by upstream magnets. Runs 147-162 (called KB runs) used special, small toroids located near the E319 beam proportional chambers, while in runs 467-478, the Chicago Cyclotron air-gap dipole magnet was used (CCM calibration). In both cases, incident energies ranged from 25 to 250 GeV. The analysis of these runs was complicated by energy loss and multiple scattering in obstructing material of the upstream E98 apparatus. Since the E319 PCs are generally not hit by the deflected beam, beam energy must be determined from the method using only the E98 proportional chambers and beam hodoscopes. A further problem is that the entrance angles into the spectrometer are much shallower than those for data with the target in place. Since the calibration is a function of angle and energy, comparison of the CCM and actual data runs is difficult. The method of analysis for these calibration runs used the old reconstruction/fitting routines (VOREP) to determine spectrometer energy for the mono-energetic muons. The muon is then traced to the front of the lab (accounting for energy loss in the E98 apparatus as well as possible; see Figure 3.5). There the variable $1/E_1$ is histogrammed (E_1 itself is somewhat non-Gaussian because of multiple scattering which is proportional to $1/E_1$) and compared to the mean of the incident energy $1/E_0$. The calibration consists of shifting the spectrometer E_1 (with a multiplicative factor PLOSS) to make these distributions have the same mean. Note that the width of $1/E_1$

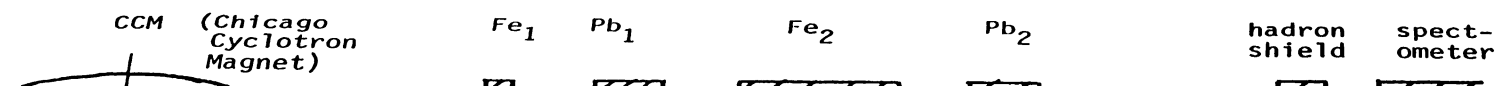
CCM (Chicago Cyclotron Magnet)
Fe1
Pb1
Fe2
Pb2
hadron shield
spect-ometer

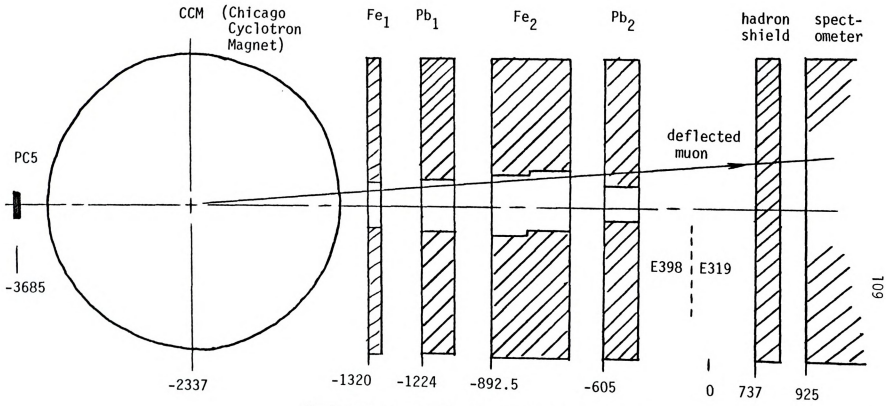

Figure 3.5--Layout of E398 and E319 apparatus during the spectrometer calibration

gives the

summarize

rections,

result.

Carlo cal

is fully

Chapter 4

similar t

the end o

The resul

data.

of points

cise cali

calibrati

available

Histogram

gives both

allows eas

Tables 3.1

sis, where

energies,

gives the resolution of the magnetic spectrometer. The results are summarized in Table 3.11.

Due to uncertainties in beam momentum and energy loss corrections, there was considerable doubt about the CCM calibration result. As a check (and refinement) of the calibration, a Monte Carlo calculation was made (using the updated E26 program MCP which is fully described in several theses[5] and briefly outlined in Chapter 4). Initially the program was run at energies and angles similar to the calibration runs and the true energy distribution at the end of the target compared to the reconstructed distribution. The results are shown in Table 3.12 and compare well with the CCM data.

The above calibrations were quite limited in range and number of points sampled in the E_1-θ plane. In order to develop more precise calibration and resolution functions needed for the Monte Carlo calibration, MCP events were generated over the whole E_1 and θ plane available to multimuon events and then binned in a 10 x 10 array. Histogramming the quantity

$$\Delta = \left[\frac{1}{E_{fit}} - \frac{1}{E_{true}}\right] \Big/ \frac{1}{E_{fit}}$$

gives both calibration and resolution data over the whole range and allows easy application for either data or Monte Carlo corrections. Tables 3.13 and 3.14 summarize the results used for multimuon analysis, where the calibration shifts were applied to the actual data energies, but the resolutions were used in Monte Carlo calculation.

RUN NO.	NO ENI
471	
470	
468	
469	
comb	
473	
474	

Calibra

E(MC)	
250	
200	
150	
100	
50	

Table 3.11

Calibration of the Spectrometer using the CCM

RUN NO.	NOMINAL ENERGY	E_0 GeV	$1/\langle 1/E \rangle$ GeV	$\sigma(E)$	EVENTS	$(E_0-E)/E_0$
471	250	248.4±1.0	243.5±.3	9.5%	3488	2.0%
470	200	200.3±0.5	199.3±.3	9.4%	5528	0.5%
468	150	149.5±0.4	149.3±.2	8.9%	3098	0.13%
469	150	149.1±0.4	148.6±.3	9.1%	2954	0.35%
comb	150	149.4±0.4	149.0±.2	9.0%	6052	0.25%
473	100	98.9±0.24	96.3±0.2	9.4%	6055	2.6%
474	50	47.56±.14	45.89±.08	9.3%	2665	3.5%

Table 3.12

Calibration of the Spectrometer using Monte Carlo Data

E(MC)	E(reconstructed)	$\sigma(E)$	EVENTS	(E(MC)-E(RE))/E(MC)
250	251.83±.17	1.8%	699	-0.7%
200	201.36±.21	1.6%	228	-0.7%
150	150.91±.08	1.4%	631	-0.6%
100	100.56±.08	1.2%	223	-0.6%
50	49.51±.04	1.2%	274	+1.0%

TABLE 3

Top num
Bottom
Each bi

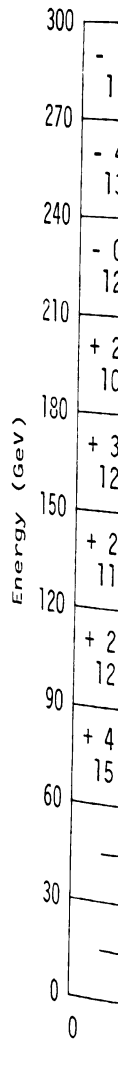

TABLE 3.13.--Positive Muon Calibration

Top number is the energy shift (in %) to be applied to data.
Bottom number is the resolution (in %) used with Monte Carlo.
Each bin contains $\geq$ 10 events.

Energy (GeV)	0	16	32	48	64	80	96	112	128
300	- 9.9 17.1	- 3.5 8.6	0.1 9.2	- 6.8 12.1	-11.7 18.4	—	—	—	
270	- 4.3 13.9	+ 0.2 8.9	+ 1.9 10.4	+ 0.6 10.8	- 7.0 16.1	- 7.5 18.2	—	—	
240	- 0.1 12.1	+ 1.7 8.7	+ 3.8 8.9	+ 2.4 10.9	+ 3.0 15.4	- 2.4 21.8	- 7.7 26.5	—	
210	+ 2.6 10.8	+ 3.0 8.3	+ 3.9 8.1	+ 4.9 10.2	+ 6.0 17.5	+ 3.4 22.0	+13.3 20.6	—	
180	+ 3.2 12.3	+ 3.9 9.0	+ 6.0 8.1	+ 8.0 11.4	+ 8.2 17.4	+12.9 20.4	+16.0 22.0	—	
150	+ 2.2 11.9	+ 3.9 8.1	+ 4.9 8.7	+ 6.7 11.1	+10.3 18.1	+16.1 23.7	+19.1 25.0	—	
120	+ 2.7 12.4	+ 3.9 9.6	+ 4.6 8.9	+ 8.6 11.2	+13.7 17.4	+18.0 26.4	+20.9 29.7	+26.0 29.9	
90	+ 4.2 15.8	+ 3.4 9.9	+ 5.7 8.3	+ 8.5 10.2	+11.2 15.9	+20.4 30.5	+27.2 34.5	+42.1 32.5	
60	—	+ 4.6 9.5	+ 7.0 9.0	+ 7.8 9.8	+10.0 12.7	+19.7 32.9	+48.1 50.8	+60.9 55.3	
30	—	+ 4.9 21.9	+ 7.9 12.6	+ 8.5 10.2	+11.5 12.6	+13.6 15.5	+17.5 25.7	+28.7 38.7	
0									

Polar Angle (mr)

TABLE 3.

Top numb

Bottom r

Each bir

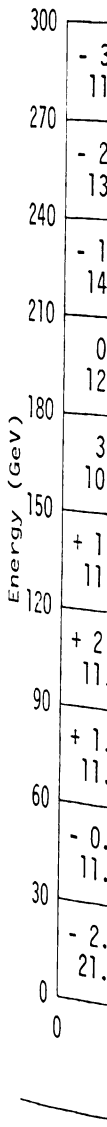

TABLE 3.14.--Negative Muon Calibration

Top number is the energy shift (in %) to be applied to data.
Bottom number is the resolution (in %) used with Monte Carlo.
Each bin contains $\geq$ 10 events.

Energy (GeV) \ Polar Angle (mr)	0–16	16–32	32–48	48–64	64–80	80–96	96–112	112–128
270–300	- 3.5 11.8	- 5.7 10.8	- 0.9 8.2	-10.9 14.8	-16.2 22.5	—	—	—
240–270	- 2.2 13.4	- 0.8 9.6	- 0.6 10.6	- 5.0 13.7	- 9.0 21.8	—	—	—
210–240	- 1.1 14.0	+ 2.2 9.7	+ 2.8 10.0	+ 2.4 13.8	+ 1.2 15.6	- 0.5 19.2	—	—
180–210	0.0 12.8	+ 3.4 9.2	+ 4.0 10.4	+ 6.2 12.6	+ 4.8 17.4	+ 5.6 20.2	+15.6 15.1	—
150–180	3.3 10.7	+ 4.1 9.5	+ 4.6 9.6	+ 8.5 14.6	+ 9.3 23.0	+11.3 24.7	+14.6 24.7	—
120–150	+ 1.8 11.7	+ 3.7 9.3	+ 5.1 10.2	+ 6.0 15.9	+12.2 22.4	+17.3 25.3	+21.4 21.9	—
90–120	+ 2.0 11.7	+ 3.1 9.4	+ 5.7 9.6	+ 6.8 15.2	+15.9 23.5	+21.7 27.0	+26.0 27.1	+30.7 30.9
60–90	+ 1.7 11.1	+ 3.2 9.9	+ 5.0 10.1	+ 9.1 13.2	+12.1 22.7	+23.7 35.9	+28.9 35.6	+41.0 40.0
30–60	- 0.7 11.3	+ 3.5 9.9	+ 5.2 10.5	+ 7.6 13.2	+10.4 21.0	+34.2 48.4	+47.1 51.0	+66.5 28.6
0–30	- 2.8 21.8	+ 4.7 11.2	+ 7.6 12.0	+ 9.7 15.3	+12.3 21.8	+16.1 23.0	+29.8 34.7	+39.6 35.1

3.6 Mul

was to f

ples. T

plished

list of

most are

cient me

cussed e

cator.

target,

muons th

showers

est, yet

4012 grap

shows any

tional ch

magnets.

events we

on events

tic patte

of the pr

scanning

2.5% of t

3.6 Multimuon Finding

The goal of the data analysis (for this dissertation, anyway) was to find as many multimuons as possible from the E319 data samples. The remaining discussion will focus on how this was accomplished given the tools of the preceding sections.

The end result of the track reconstruction programs is a list of event numbers, a few of which are true multimuons, although most are single muons combined with halo and extra sparks. An efficient method of picking out the true multimuons was needed. As discussed earlier, the dimuon trigger was not a very good indicator. The calorimeter often indicates when two muons leave the target, but no algorithm I tried could overcome problems like two muons throughout the calorimeter (halo), noise in the ADCs, and showers near the end. The method settled upon is the oldest, slowest, yet most reliable one; the events were displayed (on a Tektronix 4012 graphics terminal) and visually scanned. The display program shows any of the four views of the spark chambers and the proportional chambers, along with options to view trigger banks, ADCs, and magnets. Paper plots can be made of any event (and all multimuon events were plotted). The reason why scanning works so well, even on events where the computer algorithms fail, stems from the fantastic pattern recognition ability of the human eye and brain, in spite of the presence of considerable "noise." However, the problem with scanning is that it takes a great deal of time (even scanning roughly 2.5% of the data took several man-years). Undergraduate college

students

criteria

tually t

deciding

of the p

responsi

as a qua

The domi

For most

nificant

(especia

hitting

of the s

low angl

causing

finding

8" x 11"

of appro

required

were com

form X-Y

fitting

susceptib

students were easily trained to recognize multimuon events, given the criteria shown in Table 3.15. The more experienced scanners eventually took over supervision of the effort, even to the point of deciding which events were worth plotting. The final classification of the plots (into eight categories shown in Table 3.16) was my responsibility.

As multimuon events were found, it became clear that as many as a quarter of them had at least one poorly reconstructed track. The dominant reasons were spark chamber inefficiency and breakdown. For most tracks, a single spark missing or incorrect does not significantly harm the reconstruction or momentum fitting process (especially with the spark pulling algorithm). However, for tracks hitting very few chambers (e.g., tracks bending quickly out the side of the spectrometer) or for tracks very near the toroid hole (mostly low angle, high energy muons), such problems can be disastrous, causing the momentum fitting to fail or give incorrect answers.

To remedy this, a procedure was developed for manual spark finding by direct measurement from the plots of the events. The 8" x 11" size plots afforded a resolution (in real spatial coordinates) of approximately 2 mm, sufficient for most tracks. Most events required the measurement of only one spark, although a few tracks were completely re-measured. The sparks are aligned and matched to form X-Y coordinates. The track can then be fed to the momentum fitting program in the usual manner. Of course, this procedure is susceptible to possible bias. To check for this, several events,

TABLE 3.

1. Exam
trom

2. Vert
view

3. Use
"liv

4. Exam

5. If s

TABLE 3.

Type
1A
1B
2A
2B
3
4
5

TABLE 3.15.--Scanning Criteria

1. Examine U and V views. Search for evidence of 2 or more spectrometer tracks. If found, examine X and Y.
2. Vertex must appear to be within the target and not change from view to view.
3. Use trigger bank counters and beam vetoes to judge if tracks "live." HPCs also helpful.
4. Examine ADCs to see if 1 particle incoming and $\geq$ 2 leaving target.
5. If still in doubt, plot the event for detailed examinations.

TABLE 3.16.--Multimuon Candidate Types

Type	Description
1A	Definite trimuon. Tracks traceable. TBCs and calorimeter agree.
1B	Questionable trimuon. Tracks uncertain; TBC, calorimeter information not clear.
2A	Definite dimuon. Two clear tracks with TBC and calorimeter consistent.
2B	Questionable dimuon. One or more tracks uncertain. TBC or calorimeter inconsistent.
3	Possible dimuon but 1 track in the magnet hole region.
4	Interesting events (eg. high q^2) but not multimuons.
5	Not a multimuon (usually 2nd track turns out to be halo or stale beam).

which ha

re-fit.

in all c

not be f

kinematic

kinematic

lations r

which hav

MSU (in

events in

or histog

can occur

structior

or by use

no pre-se

ple indep

the effor

data samp

grams to

special h

VOREP com

one progr

high q^2 (

which had been adequately reconstructed and fit, were measured and re-fit. The result was quite stable and accurate to within 10% in all cases. Note that some multimuon events had tracks which could not be fixed. These events are, of course, not included in the full kinematic samples to be presented in Chapter 5, although partial kinematic information is available for most of them and rate calculations must count these events. The complete samples of events which have fully determined kinematics are maintained on tape at MSU (in the secondary tape format), with tracks arranged within the events in order of decreasing E_1. Analysis programs to apply cuts or histogram various kinematics can be run directly on these samples.

Potential losses and kinematic biases in multimuon finding can occur in both the reconstruction and scanning phases. Reconstruction problems can be checked by comparison with other programs or by use of "mass" scanning (visually examine raw data triggers with no pre-selection). Scanning losses can be understood by doing multiple independent scans on the same events. The following describes the efforts made to determine these losses for the main (270 GeV μ+) data sample.

PASS2 has been compared with three other reconstruction programs to estimate its single muon efficiency; VOREP, PASS1 and a special high efficiency version of MULTIMU called PASSOUT. The VOREP comparison was a visual scan study of the events missed by one program and found by the other for low q^2 ($\leq 8 GeV^2/c^2$), and high q^2 ($\geq$ 40 GeV^2/c^2) regions. The results implied that the

inefficie

are lost

is not hi

highlight

part of t

similar f

called PA

in front

applied t

extra ever

the ratio

In

for multi

extremely

smaller sa

results sh

multimuons

efficiency

and the be

this using

of 5 GeV i

Mu

dichotomy.

been re-sc

shown in T

inefficiency of PASS2 was < 10%, except at very high q^2 (where events are lost because they miss the HPCs and the front chamber efficiency is not high). The comparison with PASS1 events on the other hand highlights any potential problems with reconstruction in the back part of the spectrometer, since the two versions of MULTIMU use similar front algorithms. Finally, the efficient version of MULTIMU called PASSOUT (basically the only differences are added redundancy in front lines and wider cuts making much longer running times) was applied to events missed by PASS2 on 28 data tapes yielding 3820 extra events with tracks (or around a 7% inefficiency). The shape of the ratio (PASSOUT-PASS2)/PASS2 is seen in Figures 3.6 and 3.7.

Independent of computer algorithms, reconstruction efficiency for multimuons can be determined by mass scanning. Since this is extremely time-consuming, only two μ+ tapes (runs 280 and 363) and smaller samples of μ- and 150 GeV data were mass scanned. From the results shown in Table 3.17, PASS2 is clearly an efficient finder of multimuons (>92% for energies > 5 GeV). At very low energies, the efficiency falls off dramatically because of front chamber losses and the bend in the first magnet. Instead of trying to correct for this using the low statistics from mass scanning, a cut in energy of 5 GeV is imposed on all further kinematic distributions.

Multiple scans were a natural outgrowth of the PASS1-PASS2 dichotomy. However, at least 30% of the PASS2 events have themselves been re-scanned. The details of the scanning efficiency checks are shown in Table 3.17. The combined efficiency shown there is

20.00

00

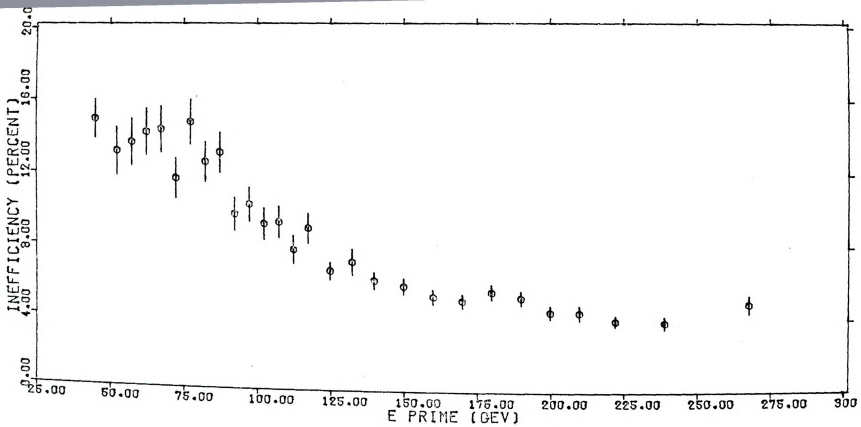

Figure 3.6.--MULTIMU (PASS 2) Reconstruction Inefficiency vs. Scattered (Leading) Muon Energy.

Figure 3.7

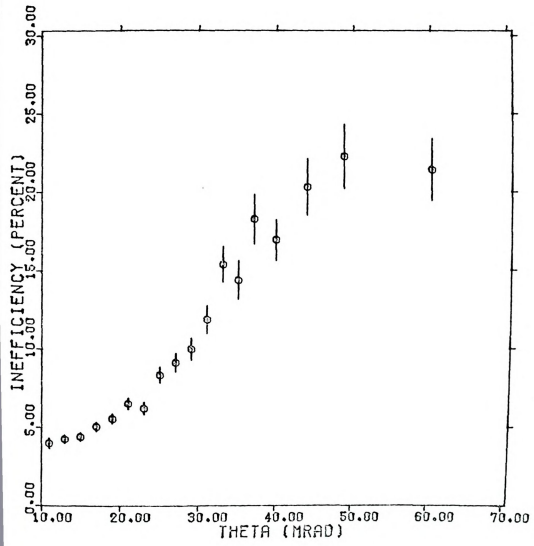

Figure 3.7.--MULTIMU (PASS2) Reconstruction Inefficiency vs. Scattered (Leading) Muon Polar Angle.

TABLE 3.1

A. Multi

Tw

Tw
giving

Ho
mass s

Br

R

B. Multim

PA
8 trim

PA
rescan
and 89

S

C. Multim

Fi

TABLE 3.17.--Finding Efficiency

A. Multimuon Reconstruction Efficiency

Two μ^+ data tapes scanned represent about 1.5% of full sample.

Twelve dimuons found by PASS2 and 19 found by mass scan giving only 63% efficiency.

However, requiring all energies $\geq$ 5 GeV gives only 13 mass scan events making efficiency of 92.3%

Broken down into components,

$$R = \text{Reconstruction efficiency} = \begin{matrix}(83 \pm 5)\% \text{ dimuons} \\ (96 \pm 5)\% \text{ trimuons}\end{matrix}$$

B. Multimuon Scanning Efficiency

PASS1 events not found by PASS2 scan: 25 dimuons (5.6%) and 8 trimuons (12.5%).

PASS2 multiple scans: 9.5% of the total (1.61×10^4) events rescanned yielding average efficiencies of 77.8% for dimuons and 89.7% for trimuons.

$$S = \text{Scanning efficiency} = \begin{matrix}(83.9 \pm 5)\% \text{ dimuons} \\ (92.6 \pm 5)\% \text{ trimuons}\end{matrix}$$

C. Multimuon Combined Efficiency

$$\text{Finding Effiency} \equiv R \times S = \begin{matrix}(70 \pm 7)\% \text{ dimuons} \\ (89 \pm 7)\% \text{ trimuons}\end{matrix}$$

necessar

lized Mor

only on t

other sam

necessary for all rate calculations and also to compare with normalized Monte Carlo predictions. Note that efficiences were obtained only on the 270 GeV μ^+ sample and are assumed to be valid for the other samples too.

4.1 Phi
Calculat

insuffic

being mea

apparatus

which the

ent in th

monetary

apparatus

sical mod

complicat

their pre

(d) severa

data, with

comparison

cal (compu

a simulate

This metho

select (th

CHAPTER 4

MONTE CARLO ANALYSIS AND MODEL CALCULATIONS

4.1 Philosophy of Monte Carlo Calculations

The data taken in modern particle experiments is often insufficient for a complete description of the physical process being measured because: (a) the acceptance of the experimental apparatus (defined for each kinematic region as the ratio of events which the apparatus could detect to the total number of events present in that region) is not uniformly 100 percent, usually due to monetary and space limitations; (b) independent of geometry, the apparatus is never completely efficient (hardware failures); (c) physical models, with which the data is to be compared, are often very complicated with few unambiguous features (e.g., mass peaks) and their predictions are usually greatly modified by acceptance; and (d) several physical processes are frequently responsible for the data, with separation possible only after detailed rate and kinematic comparisons. The most common solution to these problems is numerical (computer) calculation of physical cross sections, folded with a simulated apparatus which accounts for acceptance and efficiency. This method, called Monte Carlo simulation,[1] uses random numbers to select (throw) particle kinematics and calculates the probability

that the

ciency),

variation

the magne

Although

single mu

tribute t

programs

philosoph

give large

production

meson proc

matic cuts

so small t

beyond dis

Th

developed

E26. Since

described

employed by

University

models for

outlined (S

and compare

that the experiment would detect the event (acceptance and efficiency), if nature produced it (cross section of the model).

For both single muon and multimuon parts of E319, the rapid variations in acceptance due to angular and energy limitations of the magnetic spectrometer have made Monte Carlo indispensable. Although deep inelastic scattering is known to be responsible for single muon data, all of the models discussed in Chapter 1 may contribute to multimuon events. The complexity and cost of Monte Carlo programs forbade any attempt to model all of these processes. Our philosophy was to simulate only those models which were expected to give large rates and nondistinctive kinematics (especially charm production, π/k decay and QED tridents). Heavy lepton and vector meson processes lead to clear experimental signatures so that kinematic cuts would isolate these signals. Their expected rates are so small that the data probably could supply little information beyond discovery, making Monte Carlo calculations unnecessary.

The main Monte Carlo computer program used for E319 was developed by A. Van Ginneken (Fermilab) for the previous experiment E26. Since some of its methods are novel, the program will be described in detail (Section 4.2). An independent program was employed by a group of theorists (represented by W. Y. Keung) at the University of Wisconsin (Madison) to calculate several different models for comparison with our data. This method will be briefly outlined (Section 4.2). Section 4.3 describes the QED calculations and compares the results from the two programs, while Section 4.4

does the

data dis

4.2 Mon

basic se

cles are

ciently

(2) Mode

differen

calculate

be subjec

ments of

to data s

of the ev

rate), an

weighted

among Mon

acceptanc

event gen

a.

b.

does the same for hadronic processes. Detailed comparisons with data distributions will be made in Chapter 5.

4.2 Monte Carlo Methods

All Monte Carlo simulation programs contain at least four basic sections: (1) Event generation--the kinematics of all particles are selected in some pre-determined manner designed to efficiently sample regions of high cross section and good acceptance; (2) Model parametrization--given the kinematics, the theoretical differential cross section (and decay distribution if relevant) is calculated; (3) Apparatus acceptance--the generated particles must be subjected to all of the important geometrical and hardware requirements of the experiment, plus further analysis cuts for comparison to data samples; and (4) Weighting--the total weight (α 1/probability of the event) is formed, summed (to keep track of total predicted rate), and binned in desired kinematic variables so as to produce weighted histograms for data comparison. Most of the differences among Monte Carlo methods can be found in the event generation and acceptance phases of the programs. There are two philosophies of event generation:

a. Throw events uniformly over the available kinematic range and let the cross section and acceptance choose preferred events, or

b. Pre-select regions where throwing will be concentrated and use weighting to remove the resulting bias later

Method (
data com
cheaper
the tail
weights.
particle
accounti
ing, etc
an attem
made on
acceptan
predicte
approach
more det
because
experime
detail.

A
limits, e
incident
tion of
written t
called be
then read
of the ki

Method (a) takes much longer to achieve sufficient smoothness for data comparison and is very expensive. Method (b), which we use, is cheaper and converges more quickly, but is susceptible to spikes on the tails of distributions corresponding to rare events with large weights. There are also two types of acceptance calculation: (a) all particles are traced step by step through a simulated apparatus accounting for physical effects (e.g., energy loss, multiple scattering, etc.) and hardware effects (e.g., triggering,vetoing, etc.) in an attempt to mimic treatment of data events, or (b) simple cuts are made on generated kinematics, reproducing general features of the acceptance and hoping that finer detail makes little difference in predicted rates. This second style is characteristic of a theorist's approach and was used by Keung and co-workers. We have employed the more detailed (and much more expensive) first method, principally because it gives more believable kinematic distributions for our experiment. The E319 Monte Carlo will now be considered in more detail.

After initialization (of counters, histograms, kinematic limits, etc.), the main event generation loop begins by choosing incident muon kinematics (E_o, θ_x, θ_y, x_o, y_o). To improve simulation of incident muon distributions, the random sample of beam written to data tapes by the pulser trigger was condensed onto files called beam tapes in the format of Table 4.1. These events are then read by the Monte Carlo program with a small Gaussian smearing of the kinematics, because the sample of beam is not very large

TABLE 4.

Beam
available

(~18000 ev

tion is c

length) x

function

traced fr

to 10 step

multiple s

the "muon"

Figure 4.

muon can t

usually in

according

TABLE 4.1.--Beam Tape Format

Word	Beam Tape Format
1	Run Number
2	Event Number
3	Fit slope of track in X-Z plane (θ_x)
4	Fit slope of track in Y-Z plane (θ_y)
5	Fit X at front of target (x_0)
6	Fit Y at front of target (y_0)
7	X^2 of fit in X-Z plane
8	X^2 of fit in Y-Z plane
9	DCR3 (Triggers, PC Reset)
10	Beam Energy (E_0)

Beam tapes, written with 10 of the above blocks per record, are available for both 270 GeV μ+ and μ- data samples.

(~18000 events) and must be used repeatedly. The event vertex z position is chosen uniformly over the target length [i.e., z = (target length) x (random #), where the random numbers are supplied by the CDC function RANF in the open interval (0, 1)]. The incident muon is traced from the front of the target to the interaction vertex in up to 10 steps, accounting for average energy loss, straggling and multiple scattering by the methods detailed in Appendix C [note that the "muon" is really a set of three direction cosines, as defined in Figure 4.1, three spatial coordinates and an energy]. The scattered muon can then be generated at the vertex (i.e., throw E_1, θ_1 and ϕ_1 usually in the reference frame required for cross section calculations) according to a desired selection function, with a weight assigned to

y

For smal

Directio

Figure 4.

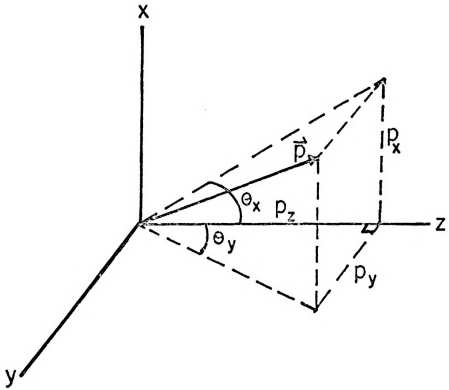

For small angles:

$$p_x = \theta_x \, p_z$$

$$p_y = \theta_y \, p_z$$

$$p_z = |\vec{p}| \, / \sqrt{1 + \theta_x^2 + \theta_y^2}$$

Direction cosines:

$$DCX = p_x / |\vec{p}|$$

$$DCY = p_y / |\vec{p}|$$

$$DCZ = p_z / |\vec{p}|$$

Figure 4.1.--Monte Carlo Conventions.

correct f

is to be

(a, b).

P

normalize

(0, 1).

r

is then s

defined a

for the d

cylindric

azimuthal

W

virtual p

duced muo

tions are

sections

all muons

calculate

section)

the accep

event is

correct for nonuniform throwing. For example, say the variable x is to be thrown by the probability density p(x) over the interval (a, b). The distribution function

$$P(x) = \int_a^x p(x)dx$$

normalized by P(b) = 1, can be represented by a random number r in (0, 1). The integral equation

$$r = \int_a^x p(x)dx$$

is then solved for x, giving the throwing equation. The weight, defined as the inverse of the probability of the throw, compensates for the deliberate biasing of x by p(x). Note that due to the cylindrical symmetry of our apparatus and model cross sections, azimuthal angles (ϕ) are always thrown uniformly in (0, 2π).

With incident and scattered muon kinematics determined, the virtual photon (referring to EM processes) is fixed, and the produced muon(s) can be generated. Usually, different selection functions are used here than for the scattered muon, because the cross sections and acceptance depend on produced muons differently. With all muons generated, the model differential cross section can be calculated and the event weight formed [= (throwing weights) x (cross section) x (integrated luminosities)]. The event is then passed to the acceptance and histogramming routines for judgment and the next event is generated.

final-sta

goals: (

which wou

the measu

generated

end of ea

(e.g., ai

netic fie

calculate

tracing p

matics ar

at the fr

tion does

spark cha

DMIN, ZMI

the angul

made at c

(Table 3.

A

veto coun

are set,

last veto

is checke

if that m

The main acceptance routine (called TRAMP) must trace all final-state muons from the vertex through the spectrometer with two goals: (a) deciding whether the muons generated constitute an event which would have triggered the apparatus and (b) determining what the measured kinematics of the event would be (as opposed to the generated kinematics). Constant steps of 5 cm are taken and, at the end of each step, a locating routing (HITOR) tells what material (e.g., air, iron, etc.) the muon is in and the strength of the magnetic field. Energy loss, multiple scattering and bending all are calculated and applied to the direction cosines (Appendix C). The tracing pauses at several places in the spectrometer to store kinematics and make cuts. The momentum and direction cosines are stored at the front of the spectrometer, since the data momentum determination does the same. Track positions are recorded at the location of spark chambers 9 and 8, and reconstruction cuts (maximum angle, ZMIN, DMIN, ZMIN-Z as in Table 3.9) are applied at chamber 8 along with the angular resolution of the momentum fitting. Further cuts are made at chamber 7 to simulate the reconstruction line-finding windows (Table 3.9).

As the muon is traced further back, trigger bank and beam veto counter positions are reached. At each such place, indices are set, denoting which counters would have been struck. After the last veto, tracing ceases and the status of triggering and vetoing is checked. Each muon, n, has an acceptance flag NMP (n) which: = 1 if that muon triggered the apparatus (or at least participated in a

multi-par

vetoing,

it is mon

event hav

N

is formed

then used

and TRIMU

and accep

their kin

tum fitti

the spect

function

3.5). Th

modified

preserved

distribut

smeared ea

events is

is a mult

is divided

rate, and

Du

and the al

multi-particle trigger), = 2 if that muon vetoed or cooperated in vetoing, = 3 if the muon passed through at least one magnet so that it is momentum analyzable, = 5 otherwise. After all muons of the event have been traced, an index

$$NCODE = 25 \times (NMP(1)-1) + 5 \times (NMP(2)-1) + NMP(3)$$

is formed which carries the event signature uniquely. This index is then used to determine (from the preset arrays labeled NGO, DIMU and TRIMU) whether (and what kind of) a multimuon has been generated and accepted. After all muons are traced through the spectrometer, their kinematics must be modified to simulate the effects of the momentum fitting algorithm and the inherent resolution and calibration of the spectrometer. Six points are chosen on the Gaussian resolution function (with standard deviation and mean as discussed in Section 3.5). These are then treated as six independent muons, with weights modified by position in the Gaussian. Thus the total weight is preserved, but resolution is naturally accounted for, and smooth distributions are obtained much more quickly than if one simply smeared each muon once. Finally, the weight for each of the smeared events is stuffed into the appropriate kinematic bins, if the event is a multimuon. At the end of each run, the total weight generated is divided by the number of thrown muons to give the experimental rate, and properly weighted histograms give kinematic distributions.

Due to the limited number of multimuon events usually obtained and the already large running costs of these Monte Carlo calculations,

we have g

make < 1C

rections,

errors in

with diff

deviation

with data

T

Carlo inte

determined

sequence c

(with n =

section).

phase spac

section is

the produc

weighted h

all variab

the summed

not indivi

many exper

triggering.

are its sim

of Wisconsi

processes.

two methods

we have generally not included physical or geometrical effects which make < 10% changes in single muon Monte Carlo (e.g., radiative corrections, Fermi motion of target nucleons, etc.). To estimate random errors involved in these simulations, several runs are always made with different initial random numbers and the means and standard deviations of each bin of the histograms are used for comparison with data.

The "Keung" simulation methods essentially perform a Monte Carlo integration of the model differential cross section over limits determined by features of the experimental acceptance.[2] A random sequence of numbers is used to form an n-dimensional unit hypercube (with n = number of independent variables in the differential cross section). This is then mapped by a weighting transformation onto the phase space volume available (within acceptance cuts). The cross section is calculated within each bin and the final weight is then the product of cross section and the Jacobian of the mapping. Weighted histograms are formed by integration (summing weights) over all variables except the one being histogramed. The total rate is the summed weight, divided by number of events generated. Muons are not individually generated or traced through an apparatus, so that many experimental details (e.g., magnetic field bending, cooperative triggering, etc.) cannot be modeled. The advantages of this method are its simplicity and low cost. We are grateful to the University of Wisconsin group for their willingness to simulate several difficult processes. The acceptance cuts they used, and some comparison of the two methods will be shown in the next sections.

(called

the spect

lous muor

be moment

cal effec

problems

tion and

events.

single mu

matic rang

tion 3.5.

4.3 Simul

Th

were those

Chapter 1,

trimuon ev

and kinema

In this se

tridents (a

tion proces

apparatus f

Monte Carlo

The

was supplie

Brief mention must be made of the original E26 Monte Carlo (called MCP), since it was used to obtain the energy calibration of the spectrometer. The virtue of this program is its extremely meticulous muon tracing and ability to write event output tapes, which can be momentum fit in the same way as the data. Furthermore, all physical effects (to the 1-2% level) are included in this program. The problems with it include large cost (due to somewhat wasteful generation and the detailed tracing) and the inability to generate multimuon events. Detailed comparisons of MCP with the methods we used for single muon analysis show excellent agreement over most of the kinematic range. The use of MCP for calibration was described in Section 3.5.

4.3 Simulation of QED Processes

The most important Monte Carlo calculations for this thesis were those for Bethe-Heitler tridents. As already discussed in Chapter 1, this process concentrates a potentially large number of trimuon events in a very poor acceptance region, making rate estimates and kinematic comparisons impossible without Monte Carlo simulations. In this section, the results of both Monte Carlo calculations for tridents (and the related pseudotrident and heavy lepton pair production processes) are presented with comparisons. The acceptance of the apparatus for such low angle multimuons is also shown. Hadronic Monte Carlo calculations are outlined in Section 4.4.

The differential cross section for our calculation of tridents was supplied by a computer code (TRIDNT) written by Brodsky and Ting.[3]

This pro

(using e

a spin-z

statistic

mined by

polar ang

state muc

then calc

strained

energies

All of th

$$\frac{d}{d}$$

can then

$$CC$$

carries th

$\mu b/GeV^2 Sr^3$

$$PT$$

is the phas

$$QT$$

This program calculates four different types of elastic tridents (using electrons and/or muons as incident and final particles) in a spin-zero nucleus of charge Z and form factor $F(q_n^2)$ with lepton statistics (Fermi-Dirac or Bose-Einstein) and spin (0 or 1/2) determined by the user. For each event, the kinematics (energy E in MeV, polar angle θ and azimuthal angle ϕ both in radians) of the three final state muons are passed to TRIDNT and stored in arrays (4-momenta are then calculated internally). Note that the incident muon is constrained to have $\theta_4 = \phi_4 = 0$ (i.e., to be along the z axis) and the energies must obey $E_4 = E_1 + E_2 + E_3$ because the events are elastic. All of the factors in the differential cross section

$$\frac{d^5\sigma}{dE_1 dE_2 (d\Omega)^3} = CCT \times PT \times QT \times SU$$

can then be calculated as follows. The first term

$$CCT = \frac{\alpha^4}{2\pi^4}(hc)^2(1 \times 10^{10}) = 5.7 \times 10^3$$

carries the constants and conversion factors from cm^2/MeV^2Sr^3 to $\mu b/GeV^2Sr^3$. The second factor

$$PT = \frac{P_1 P_2 P_3}{P_4}$$

is the phase space factor while the third

$$QT = \frac{Z^2 F^2(q_n^2)}{q_n^4}$$

carries

transfer

discusse

interact

whole nuc

good appr

with indi

(instead

the numbe

inside th

deal with

tion whic

using the

matric ele

and Dirac

summing ov

and was nc

resulting

mental dat

Th

Carlo fram

rates and

E319. It

region of

maximizes

carries all nuclear structure information (note q_n is the 4-momentum transfer to the nucleus). The nuclear form factors used will be discussed in Appendix C. Of course, this description of the nuclear interaction, where the virtual photon interacts coherently with the whole nucleus, is strictly valid only for low q_n^2. However, to a good approximation, incoherent processes (where the interaction is with individual nucleons) can be described by using elastic nucleon (instead of nuclear) form factors, setting Z = 1, and multiplying by the number of nucleons A. For still higher q_n^2 the interaction probes inside the nucleons and becomes inelastic. The TRIDNT code cannot deal with this because inelasticity destroys the energy balance condition which allows all four diagrams (see Figure 1.4) to be calculated using the same algorithm. Finally, the fourth term SU represents the matric elements squared, calculated by numerically multiplying spinors and Dirac matrices for each helicity state, squaring the result, and summing over all helicities. The coding of this is quite complicated and was not directly checked. We relied instead on comparing the resulting distributions with independent calculations and experimental data.

The TRIDNT routines were used in conjunction with the Monte Carlo framework described in the previous section to calculate trident rates and distributions expected from the 270 GeV μ^+ data sample of E319. It is particularly important since tridents occupy such a small region of phase space, to generate muon kinematics in a way that maximizes the product of cross section and acceptance. We have

attem

Chapt

about

incid

bilit

muon

severa

suffi

kinema

(and

of the

howeve

is co

per ru

10000-

enough

Severa

produc

accoun

accept

greate

attempted to sample the four Tannenbaum[4] regions (as described in Chapter 1)by throwing produced muon polar angles exponentially peaked about zero. These thrown angles can be taken relative to either the incident muon, scattered muon, or the virtual photon and these possibilities are tried for each event. The generation of both scattered muon kinematics and produced muon energies was then optimized in several test runs to allow minimum spikiness and cost.

If the product of kinematic and cross section weights is sufficiently large, a loop is set up to exploit this favorable set of kinematics by simply re-throwing azimuthal angles up to twelve times (and dividing each weight by 12). This greatly enhances the sampling of the four "good" regions and reduces running time. The results, however, should be independent of generating functions (if weighting is correct) for high statistics runs. The number of events generated per run is set to keep the bin variations reasonably low (usually 10000-50000 events are required, with from 10-50% having weights large enough to be counted).

Our trident Monte Carlo runs are summarized in Table 4.2. Several conclusions can be made:

1. The number of multimuon events expected from trident production is quite low and, as we shall show in Chapter 5, does not account for most of the E319 events;

2. Although tridents naturally lead to trimuons, the acceptance converts ~ 1/2 of these into dimuons;

3. These dimuons are primarily OSPs, because SSPs have a greater chance of the missing muon being bent into the beam veto;

TABLE 4.2.--E319 Monte Carlo Results for Tridents

Run	Process	Number Generated	2μ Total	2μ σ	OSP	SSP	3μ Total	3μ σ
c	Fe	10000	2.0	0.7	1.8	0.2	2.9	2.4
d	Fe	20000	1.4	0.4	0.9	0.5	1.3	0.3
e	Fe	20000	2.5	2.5	2.2	0.3	0.4	0.1
Average	Fe	50000	2.0	2.6	1.6	0.4	1.5	2.4
I	p	10000	14.1	5.3	13.0	1.1	7.6	1.2
J	p	10000	9.1	0.6	6.3	2.8	8.0	1.3
K	p	10000	8.0	0.7	5.8	2.2	7.1	1.3
L	p	10000	9.0	1.6	5.9	3.1	12.2	6.5
M	p	50000	8.8	0.6	7.1	1.6	7.0	0.4
Average	p	90000	9.8	5.6	7.6	2.2	8.4	6.9
Sum	Fe+p		11.8	6.2	9.2	2.6	9.9	7.3
Ratio	$\frac{q}{p}$		0.6		0.6	0.6	0.9	
Ratio	$\frac{\beta}{p}$		0.4		0.4	0.4	0.6	
Estimated Total $Fe + p\,(1 + \frac{q}{p} + \frac{\beta}{p})$			21.6	11.5	16.8	4.8	22.5	17.5

Fe = coherent tridents

p = incoherent tridents

q = inelastic tridents (estimated by Keung)

β = pseudo tridents (estimated by Keung)

4. Although coherent cross sections are much larger than those from the incoherent process before acceptance, the nuclear form factor is much more strongly peaked at low q_n^2 than the nucleon form factor, so that incoherent tridents dominate the event rates. Histograms of kinematic distributions for these tridents will be compared to the data in Chapter 5.

A multimuon acceptance table for the trident process was obtained in the following manner: the event generation part of the trident Monte Carlo was run without apparatus tracing or cuts, giving ran generated histograms. Then the appropriate accepted distribution was divided (bin by bin) by the generated distribution. Table 4.3 shows the acceptance as calculated in the produced muon transverse momentum relative to the virtual photon ($p_\perp$) (the dimuon and trimuon accepted histograms must first be added and then divided by the purely trimuon generated histogram). Two points are clear: (1) the acceptance is very low at small $p_\perp$, which is why tridents are so greatly suppressed in our experiment, and (2) the acceptance is quite different in the low bins for the two types of tridents, illustrating the model-dependent nature of multimuon acceptance. This fact prevents the use of such a simple 1-dimensional acceptance table for all processes. The problem could be avoided by forming a complete acceptance table in all relevant kinematic variables (e.g., a nine-dimensional table would be necessary for three final state muons), but this would require prohibitive amounts of Monte Carlo computer time. In the high transverse-momentum region (>2 GeV/c), the model

TABLE 4.3.--Multimuon Acceptance in $p_\perp$ for Tridents

$P_\perp$ Range (GeV/c)	Accepted			Generated			Acceptance		
	Fe	p	ASUM	Fe	p	GSUM	Fe	p	$\frac{ASUM}{GSUM}$
0.0 - 0.3	.38	1.95	2.33	1.68×10^{5}	2.21×10^{6}	1.90×10^{5}	2.27×10^{-6}	8.82×10^{-5}	1.22×10^{-5}
0.3 - 0.6	.84	3.03	3.86	1.37×10^{5}	1.86×10^{4}	1.56×10^{5}	6.09×10^{-6}	1.62×10^{-4}	2.48×10^{-5}
0.6 - 0.9	.63	2.75	3.38	2.96×10^{4}	1.02×10^{3}	3.06×10^{4}	2.14×10^{-5}	2.69×10^{-3}	1.11×10^{-4}
0.9 - 1.2	.38	2.39	2.77	4.50×10^{2}	2.83×10^{2}	7.33×10^{2}	8.36×10^{-4}	8.46×10^{-3}	3.78×10^{-3}
1.2 - 1.5	.20	1.74	1.94	42.19	40.50	82.68	4.70×10^{-3}	4.30×10^{-2}	2.35×10^{-2}
1.5 - 1.8	.11	1.02	1.14	13.28	19.30	32.58	8.48×10^{-3}	5.31×10^{-2}	3.49×10^{-2}
1.8 - 2.1	.06	1.08	1.14	3.74	7.04	10.78	1.71×10^{-2}	.15	.11
2.1 - 2.4	.06	.91	.97	.82	3.42	4.24	7.05×10^{-2}	.27	.23
2.4 - 2.7	.03	.61	.64	.31	1.61	1.92	.11	.38	.33
2.7 - 3.0	.03	.40	.42	.14	.80	.94	.20	.50	.44
3.0 - 3.3	.01	.25	.27	1.56×10^{-2}	.39	.41	.77	.65	.66
3.3 - 3.6	.01	.21	.22	1.04×10^{-2}	.19	.20	1.17*	1.08*	1.03*
3.6 - 3.9	$.42 \times 10^{-2}$	.13	.14	2.92×10^{-3}	.13	.14	1.44*	.99	1.00
3.9 - 4.2	$.70 \times 10^{-2}$	.09	.10	1.36×10^{-3}	9.56×10^{-2}	9.70×10^{-2}	5.15*	.96	1.02*
4.2 - 4.5	$.43 \times 10^{-2}$	.05	.06	9.24×10^{-4}	5.79×10^{-2}	5.86×10^{-2}	4.65*	.91	.97
4.5 - 4.8	$.36 \times 10^{-3}$	.04	.04	1.34×10^{-3}	4.20×10^{-2}	4.33×10^{-2}	.27	.88	.86
4.8 - 5.1	$.13 \times 10^{-3}$	.02	.02	5.48×10^{-4}	2.48×10^{-2}	2.53×10^{-2}	.24	.88	.86
5.1 - 5.4	$.14 \times 10^{-2}$	.01	.01	7.62×10^{-4}	2.23×10^{-2}	2.31×10^{-2}	1.84*	.63	.67
5.4 - 5.7	$.36 \times 10^{-3}$	.01	.01	6.23×10^{-4}	1.75×10^{-2}	1.81×10^{-2}	.58	.65	.65
5.7 - 6.0	$.15 \times 10^{-3}$	.007	.01	5.58×10^{-5}	1.45×10^{-2}	1.45×10^{-2}	2.69*	.50	.52
0.0 - 6.0	2.76	16.70	19.47	3.35×10^{5}	4.21×10^{4}	3.78×10^{5}	8.24×10^{-6}	3.97×10^{-4}	5.16×10^{-5}

dependence should be a minor effect. Processes concentrated in that region could be expected to have about the same acceptance as the tridents.

Using luminosities (Table 1.4) and generated event rates (Table 4.3), the total trident cross section can be calculated and compared to independent estimates, as shown in Table 4.4. The other calculations agree well with experimental data at low energies and, using the expected energy dependence, match our trident results within errors. Differences are probably due to small sampling difficulties and generation problems at the lowest angles, where the cross section peaks and the acceptance dips. The general agreement gives confidence in the calculated accepted trident event rates for E319.

Keung has used his Monte Carlo methods and independent QED differential cross section routines to calculate rates and distributions expected for tridents, as well as pseudotridents and interference between the two.[5] Briefly, the Feynman diagrams are all topologically converted to a general diagram, which is then reduced to algebraic form (via a trace manipulation routine similar to SCHOONSHIP). When fed event kinematics, the coded equations supply the full differential cross section. There is no restriction on nuclear recoil (unlike the Brodsky routines), so that inelastic tridents can be calculated.

As described in the previous section, Keung's method requires phrasing the experimental acceptance in terms of simple kinematic cuts (integration limits). Through a series of meetings with Keung, we

TABLE 4.4.--Muon Trident Total Cross Sections

Reference	Methods Used	$\sigma(\frac{nb}{nucleon})$
--	a. E319 Monte Carlo b. Total generated rate - 3.8×10^5 c. Coherent and incoherent tridents	13.5
Tannenbaum 1970 FNAL Summer Study	a. Brodsky-Ting cross section and Monte Carlo Integration b. Get .075 μb per Carbon nucleus at 12 GeV. Scale using $\sigma(E) \propto \ln(\frac{E}{6.7m_\mu})[\ln(\frac{E}{6.7m_\mu}) - \frac{3}{2}]$ c. Coherent tridents only	6.3 ± 0.5
Russell, et al., Phys. Rev. Lett. 26, 46 (1971)	a. Experimentally measured to be 51 ± 7 nb per Pb nucleus at 10.5 GeV	15.5 ± 2.1
	b. Calculated in manner similar to Tannenbaum as 60 ± 2 nb/ Pb nucleus	18.2 ± 0.6
	c. Scale both in energy as above	
Barger, et al., Preprint coo-881-83	a. Keung method for E319 b. Coherent, Incoherent, and Inelastic tridents	17

developed such a set of simple cuts (Table 4.5) to adequately describe triggering, veto, and momentum analysis requirements. To monitor the validity of Keung's results, our trident Monte Carlo was modified by replacing the extensive apparatus section with the same simple cuts. Table 4.6 compares both simple cut results with the full calculation. Several conclusions are evident: (1) The agreement between simple cut versions is quite satisfactory, with the exception of SSP events which are sensitive to magnetic field bending; (2) Neither simple cut result reproduces the full calculation for the Fe process due to its extreme sensitivity to low angle geometry; and (3) Both simple cut versions agree well with the full p calculation, which is not so strongly peaked at low energies and angles. Figure 4.2 compares the leading and produced muon energy distributions from the Fe process for all three Monte Carlo versions. Clearly, all of the calculations populate roughly the same kinematic regions with differences attributable to resolution and spectrometer bending effects. The same distributions for the p tridents are shown in Figure 4.3, where the agreement is even better. This given us confidence in Keung's calculations for other processes (e.g., inelastic tridents (q) and pseudotridents (B)) which are not too sharply peaked in low acceptance regions. Although detailed kinematic distributions are unavailable for these two processes, they appear to follow the same tendencies as the p tridents.[5] Since the rates are small (Table 4.6), we include the q and B processes by simply scaling the p trident kinematics upwards with a multiplicative factor $(1 + q/p + B/p)$,

TABLE 4.5.--Simple Cut Acceptance for E319

Purpose of Cut	Energy	Angle
1. Trigger--At least one muon must be within magnet area at the trigger banks. One μ must satisfy (a) and one μ (need not be the same one) must satisfy (b).	a. $E > 8.5r + 4.1$	$\tan\theta > \frac{15.3}{598+738r}$
		$\tan\theta < \frac{86.0}{598+738r}$
	b. $E > 8.5r + 9.0$	$\tan\theta > \frac{15.3}{1160+738r}$
		$\tan\theta < \frac{86.0}{1160+738r}$
2. Veto--All thrown muons must satisfy the angle cut unless they satisfy the energy lower limit to prevent hitting the beam veto counters	$E < 8.5r + 6.6$	$\tan\theta > \frac{15.9}{1388+738r}$
3. Momentum Analyzability--To determine the momentum (not necessary for total rates) the muons must penetrate 1 magnet	$E > 8.5r + 4.1$	$\tan\theta < \frac{86.0}{598+738r}$
		$\tan\theta > \frac{15.3}{1160+738r}$

Note: Due to the long iron target, the cuts are functions of the random number r which determines the interaction point in the target by Z = 738r.

TABLE 4.6.--Simple Cut Trident Results and Comparison to Full Calculation

Calculation	Process	2μ	OSP	SSP	OSP/SSP	3μ	3μ/2μ
E 319 Simple	Fe	37	27	10	2.7	61	1.6
E 319 Full	Fe	2.0	1.6	0.4	4.0	1.5	0.8
Keung	Fe	45	22	23	1.0	39	0.9
E 319 Simple	p	11	7	4	2.0	19	1.7
E 319 Full	p	9.8	7.6	2.2	3.5	8.4	0.9
Keung	p	27	13	14	1.0	20	0.7
E 319 Simple	Fe + p	48	34	14	2.4	80	1.7
E 319 Full	Fe + p	11.8	9.2	2.6	3.5	9.9	0.8
Keung	Fe + p	72	35	37	1.0	59	0.8
Keung	q	16	8	8	1.0	18	1.1
	(q/p)	(0.6)	(0.6)	(0.6)	--	(0.9)	--
Keung	B	≤ 10	--	--	--	≤12	--
	(B/p)	(0.4)				(0.6)	

Note: Same notation as in Table 4.2.

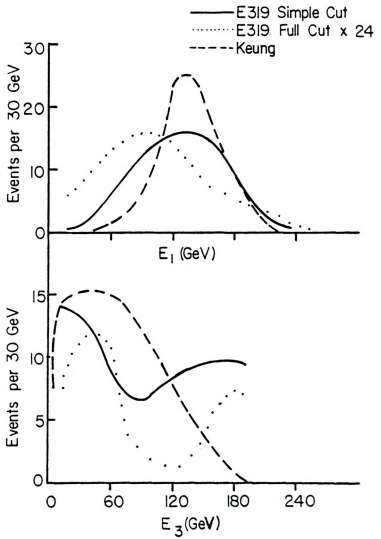

Figure 4.2.--Coherent (Fe) Trident Monte Carlo Leading Muon (E_1) and Produced Opposite Charge Muon (E_3) Energy Distributions

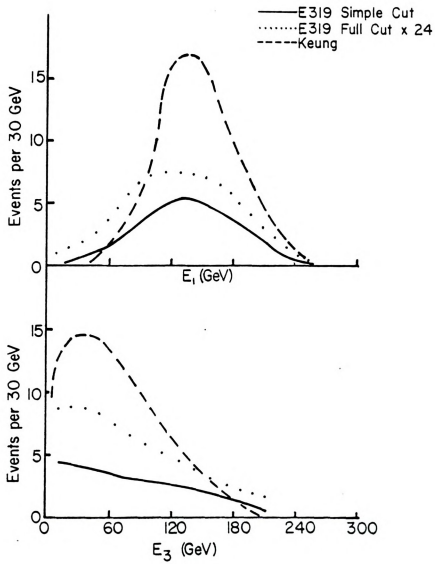

Figure 4.3.--Incoherent (p) Trident Monte Carlo Leading Muon (E_1) and Produced Opposite Charge Muon (E_3) Energy Distribution

where the rate ratios are shown in Table 4.6. The systematic errors involved are estimated to be less than 20% in each bin. Distributions from the QED calculations will be compared with hadronic processes in the next section and with the data in Chapter 5.

4.4 Simulation of Hadronic Processes

This section contains a brief outline of Monte Carlo calculations for the hadronic processes described in Chapter 1 (a more complete discussion will be available in the thesis of J. Kiley). Our effort has been directed toward calculation of the charm and pion (kaon) decay processes, which dominated the E26 multimuon rates. Keung has studied both $c\bar{c}$ and $b\bar{b}$ associated production, hadronic final state interactions (quark recombination), and vector meson production.[5] The basic methods are the same as those described in section 4.2, with modifications for calculating cross sections in the CM reference frame and weighting procedures to account for decay branching ratios of the produced hadrons.

Dimuons from the decay of one of the shower hadrons produced in the deep-inelastic scattering were the first process to be simulated for multimuon studies. The original program (called CASIM)[6] was developed to generate hadron showers (using measured hadron production cross sections and multiplicities) for use in calorimetry and shielding studies. By following each hadron until it either stops or decays, the rate of extra muons accompanying the scattered muon can be determined. Using the same program as in E26[7] (except for updating the geometry and flux) predicts 54 ± 6 dimuons and a negligible number of trimuons

from π/k decay. Due to the high hadron multiplicity, none of the shower particles receives much energy so the resulting energy and transverse momentum of the produced muon are small relative to other processes, as seen in Figure 4.4.

Associated charm production (and semi-leptonic decay) was the other main process considered in E26, where it was believed to dominate the dimuon sample. We have used essentially the same model[8] for the production and decay of charmed mesons except that the proportion of the decays $D \rightarrow k\mu\nu$ and $D \rightarrow K^{+}\mu\nu$ have been adjusted to reflect more recent data.[9] Since the normalization of this phenomenological model is left free, kinematic shape comparisons with data were used to establish the charm hypothesis. However, Keung's calculation for associated charm production uses the photon-gluon fusion model[10] which can supply rate estimates and kinematic distributions. The predicted dimuon rate after acceptance is 26 pb/nucleon, or about 730 events in the main data sample. Due to the small branching ratio (10%), the trimuon rates are quite small (about 11 events). Kinematic distributions compare closely between the two independent calculations, showing the characteristically steep fall-off in transverse momenta of all hadronic processes (Figure 4.4).

A simple change in quark mass (from Mc = 1.87 to Mb = 5) in Keung's simulation allows an estimate of heavy quark production. At our incident energy, even without acceptance cuts, the rates are still very low (about 1 pb or 30 events) meaning that this process is almost certainly undetectable in our experiment. The kinematics of

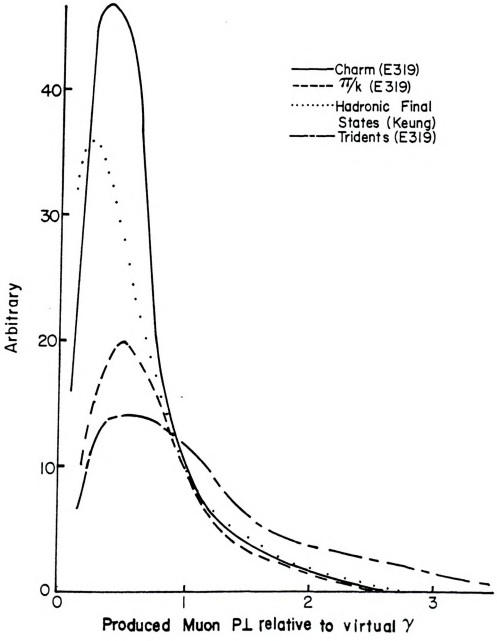

Figure 4.4.--Unnormalized Comparison of Transverse Momentum Distributions (from Monte Carlo Calculations for Several Hadronic Processes and for Tridents).

such events would be similar to those for charm production but scaled upwards to higher momenta and masses.

Neither Monte Carlo has been used for detailed examination of vector meson (Ψ) production and decay for E319 because: (a) The rates are known to be quite small (only 24 trimuons expected without acceptance correction), and (b) The kinematics are distinctive (i.e., the apparent mass of the produced muons should peak at M_ψ = 3.1 GeV). Furthermore, ψ production has been thoroughly studied already in both lepton and hadron interactions.

Finally, Keung has also calculated rates and distributions for the hadronic recombination process in a phenomenological manner based on hadron experiments with the results (Table 4.7 and Figure 4.4) appearing much like the π/k process. Indeed, Figure 4.4 illustrates that all of the hadronic processes tend to lie in low transverse momentum regions, with QED spectra being much flatter. In the next chapter, we shall exploit this and other characteristics of the Monte Carlo predictions in an attempt to isolate signals from the non-hadronic mechanisms of interest.

TABLE 4.7.--Hadronic Monte Carlo Results

Process	Monte Carlo	2μ	3μ
1. π/k decay	E319	54 ($\pm$6)	--
2. Charm ($D\bar{D}$)	Keung	730	11
3. "Beauty" $b\bar{b}$	Keung	<30 (before cuts very few after cuts)	--
4. ψ	Keung	Estimate <20	20-30
5. Hadronic Final States	Keung	25	8

CHAPTER 5

MULTIMUON DATA AND INTERPRETATIONS

5.1 Status of Data Analysis

The data taken in E319 (excluding tests and calibration) can be grouped into five chronological blocks with the following characteristics: (A) 1.1 x 10^{10} incident μ^+ at 270 GeV on the full iron target (the main data sample); (B) about 4 x 10^8 incident μ^+ at 270 GeV on a 1/3 density iron target with two out of every three iron plates removed; (C) 1.4 x 10^9 incident μ^+ at 150 GeV on the 1/3 density iron target; (D) 3.1 x 10^9 incident μ^- at 270 GeV on the full iron target; and (E) about 2 x 10^9 incident π^+, mostly at 120 GeV, on the full iron target. Data analysis (including PASS2 track reconstruction, momentum fitting and multimuon scanning) has been completed on all useful runs from samples A, C, and D. However, track fixing (manual reconstruction) and efficiency studies were performed only on A and calorimetry information was not available for C (due to problems with the 1/3 target arrangement) and E (rate effects from the large flux of pions). Sample E has been superficially examined to judge if the data would be useful for vector meson production studies. Data from B has not been analyzed because of equipment problems and the low statistics of those runs. Most of the distributions presented in the following sections came from sample A

and all Monte Carlo simulations were run with the flux and geometry of that data. Distributions from C and D will be presented only to illustrate the incident energy and incident charge dependence, respectively, of multimuon production.

We group the data events from each sample into four classes on the basis of the number of final state muons: (1) Single muon (deep inelastic scattering) events, which will be discussed here only in comparison to leading particles of multimuon events (and in Appendix A as a check on missing energy determination); (2) Dimuon events which, because they are the most numerous of the multimuon types, have received the largest analysis effort; (3) Trimuon events, which are roughly an order of magnitude scarcer than dimuons; and (4) Exotic events with four (or more) final state muons. Each of these classes will be first presented in raw form, with rate estimates and a discussion of kinematics. Then, calculation of non-leptonic processes (backgrounds) will be subtracted and the remaining data compared to the simulated leptonic signals expected. When Monte Carlo predictions are unavailable, cuts on the data will be used to attempt isolation of the signal (heavy leptons).

5.2 Single Muon Events

Although the track reconstruction and fitting programs are able to reject most improper triggers (e.g., live halo, cosmic rays, etc.), there are still some events on the secondary tapes which are neither deep inelastic scatters nor multimuons (principally

multiple scattered beam and halo events). Furthermore, some of the reconstructed tracks are not of the quality desired for the deep inelastic scattering studies. Thus, a set of geometric and kinematic cuts has been developed to further purify the sample. As detailed in Table 5.1, these cuts keep the data away from geometric (e.g., toroid holes and outer edges) and kinematic boundaries, where the apparatus and/or analysis programs are less well understood. By comparing the single muon sample thus obtained with the leading particles (those with the same charge as the beam and the highest energy) of multi-muons, the acceptance of the apparatus can be partially corrected for and multimuon rates per deep-inelastic scattering event can be obtained. For the A sample only, these rates are detailed in Table 5.2. However, these are still uncorrected for produced muon acceptance. Table 5.3 shows some single muon kinematic averages and Figure 5.1 displays kinematic distributions of single muons and leading particles of dimuon events (with and without the cuts of Table 5.1). Even after cuts, the leading muons prefer higher y and W regions, mostly because the scattered muon receives less energy on the average if other muons are produced. Also, large q^2 and low x are favored, which has been interpreted as a sign of interactions with non-valence (sea) quarks in the nucleon (e.g., charmed quarks).[1] However, large q^2 can also be considered a sign of an interaction which is not electromagnetic (because electromagnetic cross sections are proportional to $1/q^4$). We have found that the leading particle characteristics are not very helpful in distinguishing among

TABLE 5.1.--Single Muon Cuts

Definition of Cut	% Rejected by This Cut Alone	Actual % Cut by the Program
1. 0 < Beam Angle (mr) < 2	0.7	0.7
2. 0 < Beam Radius (cm) < 10	0.08	0.01
3. 243 < Beam Energy (GeV) < 297	0.5	0.1
4. -300 < ZNIN (cm) < 700	0.9	0.9
(Target stretches from -167 to 567)		
5. DMIN (cm) < 5	1.2	1.0
6. $0 < \frac{\text{Chi Squared}}{\text{Degree of Freedom}} < 10$	0.7	0.6
7. Require at least 7 of the 10 chambers to have sparks	20.2	18.1
8. Radius at Trigger Banks (cm) > 15.24	37.0	24.7
9. Radius at Beam Vetos (cm) > 15.88	12.3	0.3
10. $5 < \theta_1^{(mr)} < 1000$	9.8	0.1
11. $10 < E_1^{(GeV)} < 300$	7.7	1.7
12. $1 < Q^2$ $(GeV^2/c^2) < 500$	8.5	0.0
13. Momentum Fit Good	3.4	3.3
Total % cut		51.5%

TABLE 5.2.--Numbers and Ratios of Events

Event Type	Number Before Cuts	Number After Cuts	Ratio (After/ Before) %	Multimuons / Single Muons
Single Muons				
a. Raw	8.24×10^5	3.89×10^5	47.2	--
b. Corrected (for 7% of finding inefficiency")	8.87×10^5	4.18×10^5		
Dimuons				
a. Raw	412 ± 20	157 ± 8	38.1	$(5.9 \pm 0.6) \times 10^{-4}$
b. Corrected (for 36% finding inefficiency)	644 ± 61	245 ± 23		
Trimuons				
a. Raw	36 ± 6	8 ± 1	22.2	$(3.8 \pm 0.7) \times 10^{-5}$
b. Corrected (for 50% losses)	72 ± 13	16 ± 3		

TABLE 5.3.--Single Muon Averages

Kinematic Variable	Average After Cuts	
1. Beam Energy (E_0)	268.8	GeV
2. Scattered Energy (E_1)	168.4	GeV
3. Scattered Polar Angle (θ_1)	18.2	mr
4. 4-momentum Transfer Squared (Q^2)	14.4	$(\frac{GeV}{c})^2$
5. Energy Transfer (ν)	100.5	GeV
6. Bjorken Scaling Variable (x)	.09	
7. Fractional Photon Energy (y)	.37	
8. Center of Mass Energy (W)	12.5	GeV
9. Vertex Quality (DMIN)	.53	cm
10. Vertex Position (ZMIN)	115.6	cm

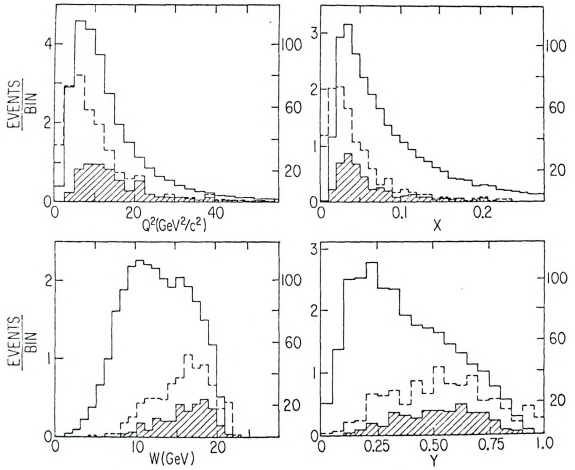

Figure 5.1.--Kinematic Comparisons of Single Muons and Leading Particles from Dimuon Events. (The solid histogram represents deep inelastic single muons after the cuts of Table 5.1 and refers to the arbitrarily-normalized left scales. The dashed histogram represents leading muons from the full dimuon sample while the shaded histogram represents leading muons after the cuts of Table 5.1. Both of the leading particle histograms use the normalized scale on the right.)

multimuon processes. In the following sections, produced muon kinematics will be shown for the various multimuon types.

5.3 Dimuon Events

Our experiment currently has the largest reported sample[2] of dimuon events from muon interactions in the world (although this will soon change as more recent experiments finish their data analysis). Three possible mechanisms can give rise to such dimuon events with differing predictions for the expected charge types: (a) the weak production and muonic decay of neutral or doubly-charged heavy leptons leading respectively to OSPs or SSPs, exclusively; (b) the electromagnetic production of hadrons, one of which decays semi-leptonically (giving equal numbers of OSPs and SSPs before acceptance); and (c) mis-identified tridents, where one muon is undetected (and the OSP to SSP ratio depends solely on the apparatus). Table 5.4 details the numbers of dimuon events (from Sample A) of various types, while Table 5.5 shows event totals from several different samples along with calculated rates, corrected for finding efficiencies, but not for apparatus acceptance. Finally, Table 5.6 displays kinematic averages for the dimuon events (note particularly the low values of produced muon energy and transverse momentum). Since the two samples with opposite incident charges (A and D) agree closely in rates and kinematics, we conclude that (a) the event fixing procedure, done only for A, makes little impact on kinematics and can be applied to all samples and (b) weak processes, which should give sign-dependent results, do not dominate dimuon production in muon

TABLE 5.4.--Dimuon Numbers (Sample A Only)

Category	Total	Events with Hadron Shower (Not Leaky)	Events with Hadron Shower (Leaky)	Total Events with Hadron Shower	Events with No Shower	Uncertain Events
Total OSP Dimuons	324	233	67	300	17	7
Analyzable OSP Dimuons	298	222	58	280	14	4
Total SSP Dimuons	125	90	27	117	6	2
Analyzable SSP Dimuons	114	86	21	107	5	2
Total Dimuons	449	323	94	417	23	9
Analyzable Dimuons	412	308	79	387	19	6

TABLE 5.5.--Dimuon Rates and Sample Comparisons

Quantity		Sample A (270 GeVμ^+)	Sample D (270 GeVμ^-)	Sample C (150 GeVμ^+)	E26 LT Data
Dimuons Found	Total	449	154	28	32
	OSP	324	102	18	15
	SSP	125	50	10	17
	OSP/SSP	2.59	2.04	1.80	0.88
Dimuons Analyzed	Total	412	82	19	32
	OSP	298	54	12	15
	SSP	114	28	7	17
	OSP/SSP	2.61	1.93	1.71	0.88
Dimuons Corrected for Efficiency	Total	644 (±55)	221 (±28)	40 ± 5	was
	OSP	465	146	26	not
	SSP	179	72	14	done
Incident Flux		1.094×10^{10}	3.085×10^{9}	1.377×10^{9}	6.1×10^{9}
"Found" rate/flux		4.1×10^{-8}	5.0×10^{-8}	2.0×10^{-8}	5.2×10^{-9}
"Corrected" rate/flux		$(5.9 \pm 0.5) \times 10^{-8}$	$(7.2 \pm .6) \times 10^{-8}$	$(2.9 \pm .3) \times 10^{-8}$	--
Luminosity		2.80×10^{37}	7.88×10^{36}	1.25×10^{36}	5.76×10^{36}
"Found cross section"		1.6×10^{-35}	2.0×10^{-35}	2.2×10^{-35}	0.6×10^{-35}
"Corrected Cross Section"		$(2.3 \pm 0.3) \times 10^{-35}$	$(2.8 \pm 0.4) \times 10^{-35}$	$(3.2 \pm 0.4) \times 10^{-35}$	--
Finding Inefficiency Correction		1.43	Used same as in A	Used same as in A	--
Kinematic Loss Correction		1.09	Used same as in A	Used same as in A	--

TABLE 5.6.--Dimuon Kinematic Averages

Average Kinematic Quantity	Sample A (270 GeV μ^+)	Sample D (270 GeV μ^-)	Sample C (150 GeV μ^+)
Leading μ Energy (E_1)	122 GeV	138 GeV	66 GeV
Produced μ Energy (E_2)	24.5 GeV	23.9 GeV	20.0 GeV
4-mom. transfer squared Q^2	10.2 $(\frac{GeV}{c})^2$	9.9 $(\frac{GeV}{c})^2$	5.9 $(\frac{GeV}{c})^2$
Transverse Momentum (P_t relative to virtual photon)	0.67 $\frac{GeV}{c}$	0.61 $\frac{GeV}{c}$	0.80 $\frac{GeV}{c}$
Hadron Energy (E_H)	86 GeV	87 GeV	
E_1/E_2	8.8	9.2	5.8
E_2/ν	0.20	0.22	0.02
Polar opening angle ($\Delta\theta_{12}$)	56 mr	57 mr	72 mr
Apparent mass (M_{12})	2.5 $\frac{GeV}{c^2}$	2.7 $\frac{GeV}{c^2}$	2.6 $\frac{GeV}{c^2}$
Azimuthal opening angle ($\Delta\phi_{12}$)	126°	127°	149°

scattering. Although the statistics are low, the 150 GeV sample (C) gives similar produced muon spectra (lower leading muon energies are obtained due to the smaller incident energy). The 150 GeV raw rates are lower than the 270 GeV samples because of the lower target density. When corrected for this factor, the rates are consistent, implying that no threshold in incident energy exists between the two samples.

As noted previously, the E319 multimuon kinematic distributions are partly shaped by apparatus acceptance, requiring Monte Carlo simulation in order to compare with theoretical models. Figures 5.2 and 5.3 detail some of the more sensitive kinematic distributions (from Sample A only) along with the dominant hadronic backgrounds. The charm calculation comes from our Monte Carlo, normalized arbitrarily to the total number of dimuon events. The other curve represents our absolutely normalized calculation for π/K decay, raised by a factor of 1.46 (from Table 4.7) to partially account for the hadronic final states background. All of the Monte Carlo calculations are reduced by the finding inefficiency and kinematic loss corrections of Table 5.5 for these kinematic comparisons. Although the normalization of the total hadronic background is thus somewhat uncertain, it is clear that most of the dimuons are adequately explained by these processes (particularly charm).

Even with the considerable calculational uncertainty, it is apparent that a few dimuons, concentrated in the elastic, large p_2 (and p_1) region, do not result from conventional hadronic processes.

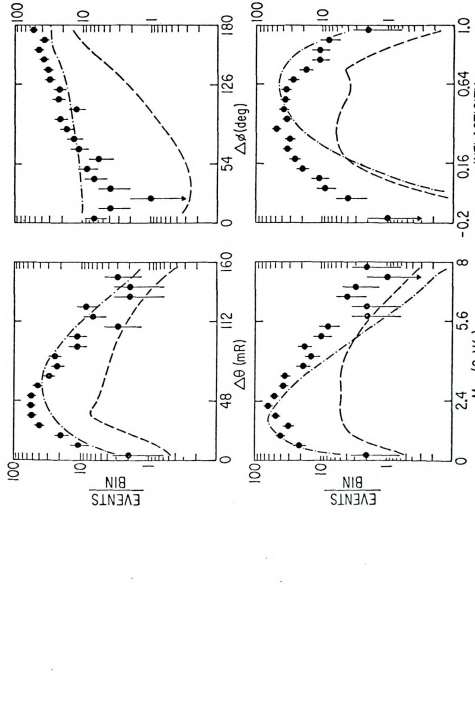

Figure 5.2.--Dimuon Data Characteristics with Calculated Hadronic Backgrounds (the curves are as described in the text with the dash-dotted one representing charm and the dotted one π/k and hadronic final states. Kinematic definitions can be found in Figure 1.1).

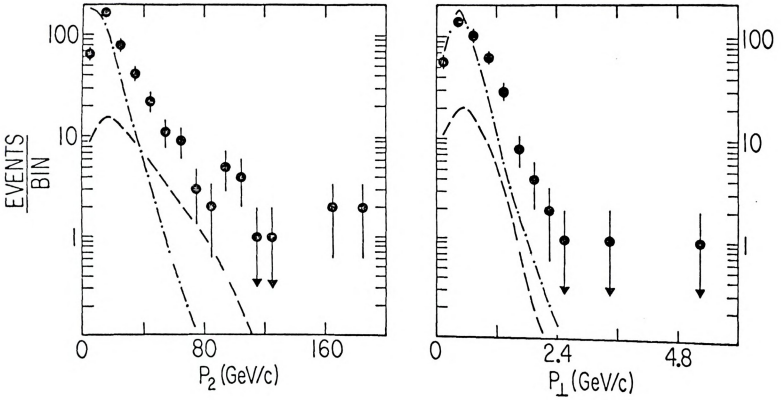

Figure 5.3.--Further Dimuon Data Characteristics with Calculated Hadronic Backgrounds (as in Figure 5.2 and the text).

In Figure 5.4 and 5.5, the data left after subtraction of the hadronic backgrounds are presented, along with the QED trident Monte Carlo predictions. Some of the excess dimuons (those concentrated at moderately high apparent mass, with large momenta, and primarily quasi-elastic) can be explained by the trident mechanism. The apparent excess of inelastic events at low p_2 ($p_\perp$) probably stems from inadequacies in the charm model and the large uncertainty in the inclusion of the hadronic recombination background. Clearly, the dimuon sample is a poor place to study tridents in this experiment due to the large charm background.

Even after all of the above processes have been subtracted, there remain a few dimuons with very large transverse momenta, which constitute possible heavy lepton and/or heavy quark production signals. However, since neither of these processes has been simulated for E319, we have chosen to return to the full dimuon sample and attempt isolation of heavy leptons via the kinematic cuts described by Albright and Shrock[3] and shown in Table 5.7. These cuts were developed for the Berkeley-FNAL-Princeton experiment (E203).[4] Although their apparatus differs from ours in several ways (which will be outlined in Chapter 6), none of the differences should prevent the use of these cuts for our data. Further, though the cuts were designed to select heavy neutral muon candidates, it is reasonable that they would also tend to select the kinematically similar doubly charged heptons.

No dimuons pass all of these cuts! However, removing the energy-dependent[5] $\Delta\phi$ cut leaves 6 OSP and 4 SSP events. This sample

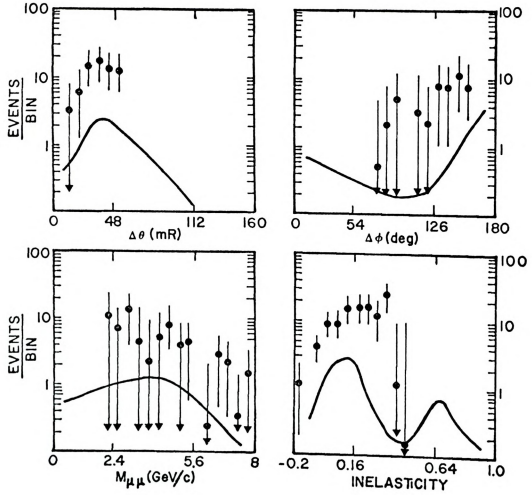

Figure 5.4.--Dimuon Data Characteristics After Subtraction of Calculated Hadronic Processes Versus Results of QED Trident Monte Carlo (Solid Curve).

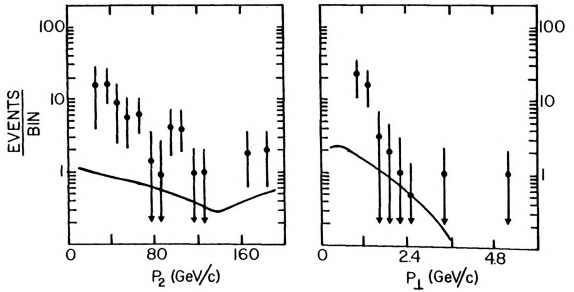

Figure 5.5.--Further Subtracted Dimuon Data Characteristics Compared to QED Trident Calculations (Solid Curve).

TABLE 5.7.--Heavy Lepton Kinematic Cuts

Kinematic Cut	Meaning
1. $E_1 > 20$ GeV	Some rejection of hadronic and EM processes
2. $E_2 > 20$ GeV	Rejects hadronic processes, which favor low produced μ energies
3. $E_H > 20$ GeV	Rejects elastic inechanisms (e.g., tridents)
4. $E_m > 20$ GeV	Favor large missing energy (i.e., decay neutrinos)
5. $Q^2 > 10 \left(\frac{GeV}{C}\right)^2$	Discriminate against EM processes which go like $1/Q^4$
6. Pais-Trieman $.48 < \frac{E_2}{E_1} < 2.1$	Characteristic of two muons from the same parent (Strongly rejects charm)
7. $M_{12} > 1.0 \frac{GeV}{C^2}$	Weak rejection of π/k and hadronic backgrounds
8. $P_{\perp 2} > 1.0 \frac{GeV}{c}$	Clear discrimination against exponentially falling hadronic transverse momentum spectra
9. $\Delta\phi_{12} < 90°$	Somewhat uncertain rejection of charm (because of broad $\Delta\phi_{12}$ distributions)

is expanded to 10 SSPs and 6 OSPs when the four explicit energy cuts are also removed. Table 5.8 summarizes the effects of these cuts and Tables 5.9 and 5.10 detail the kinematics of the events passing the reduced cuts and which tests are failed by each. If one assumes that the events which miss only the $\Delta\phi$ cut are all heavy leptons, cross section times branching ratio estimates of 2.1×10^{-37} cm^2 for SSPs (k^{++}) and 1.4×10^{-37} cm^2 for OSPs (M°) are obtained with no acceptance correction. Further, assuming that the trident acceptance applies in this moderately large $p_\perp$ region (probably good to within a factor of 2 anyway), and using it to correct the events within the bins of Table 4.3, the σ x BR estimates become 1.8×10^{-35} cm^2 for k^{++} and 1.3×10^{-35} cm^2 for M°. Perhaps more realistic estimates can be obtained by selecting a subsample of events nearest the $\Delta\phi$ boundary. From Tables 5.9 and 5.10, it is clear that only 1 OSP (299 - 4330) and 1 SSP (268 - 5907) are reasonably close and these are also the events with the largest $p_\perp$ (Figures 5.6 and 5.7 display these two events). Correcting for acceptance, these single events give σ x BR estimates of 1×10^{-36} cm^2 for M° and 3×10^{-37} cm^2 for k^{++}. The M° value is consistent with the published[6] upper limit of 2.5×10^{-36} cm^2. It is clear, however, that our estimates are subject to much uncertainty without a clear heavy lepton signal or Monte Carlo calculations. The situation should be clarified substantially by the data of more recent muon experiments which have larger incident fluxes and better acceptance than E319.[4,7]

The few high $p_\perp$ dimuons remaining after background subtraction also did not pass the heavy lepton cuts and Table 5.11 shows why,

TABLE 5.8.--Effects of Kinematic Cuts

Cuts Applied (from Table 5.7)	#OSPS Left		#SSPS Left	
1	282	(94.6%)	111	(97.4%)
2	144	(48.3%)	39	(34.2%)
3	271	(90.6%)	100	(87.7%)
4	199	(66.8%)	67	(58.8%)
5	89	(29.9%)	80	(70.2%)
6	41	(13.8%)	18	(15.8%)
7	264	(88.6%)	108	(94.7%)
8	50	(16.8%)	33	(28.9%)
9	65	(21.8%)	17	(14.9%)
1→9	0	(0%)	0	(0%)
1→8	4	(1.3%)	6	(5.3%)
5→8	6	(2.0%)	10	(8.8%)

TABLE 5.9.--OSP Events Passing Cuts (5-8): Neutral Heavy Muon Candidates

Run	Event	E_0(GeV)	E_1(GeV)	E_2(GeV)	θ_1(mr)	θ_2(mr)	$Q^2(\frac{GeV}{c})^2$	y	$P_{12}(\frac{GeV}{c})$	E_H(GeV)	E_M(GeV)	M_{12}(GeV)	$\Delta\phi_{12}$ Degrees	E_2/E_1	Cuts Failed
223	4867	270.3	49.0	57.0	33.9	28.9	12.9	.79	1.26	133.5	30.8	3.26	159.9	1.16	9
249	10126	268.6	92.4	56.5	16.5	31.2	14.8	.79	1.32	0.0	119.8	3.39	163.4	.61	3,9
252	6434	255.5	124.1	90.0	23.4	27.4	17.3	.65	2.04	16.1	25.3	4.81	126.1	.73	3,9
278	3146	270.7	99.3	69.8	20.6	28.9	15.8	.74	1.30	58.6	43.0	4.04	154.0	.70	9
290	3774	257.8	48.5	26.0	36.8	49.2	16.2	.90	1.06	70.1	113.2	3.05	171.1	.54	9
299	4330	274.2	87.7	70.4	16.5	27.0	14.1	.74	1.69	81.7	34.5	3.00	121.4	.80	9

TABLE 5.10.--SSP Events Passing Cuts (5-8) -- Hepton Candidates

Run	Event	E_0(GeV)	E_1(Gev)	E_2(GeV)	θ_1(mr)	θ_2(mr)	$Q^2(\frac{GeV}{c})^2$	y	$p_{\perp 2}(\frac{GeV}{c})$	E_H(GeV)	E_M(GeV)	$M_{12}\frac{GeV}{c^2}$	$\Delta\Phi_{12}$ degrees	E_2/E_1	Cuts Failed
224	4495	266.1	43.6	32.6	36.0	43.7	16.6	.88	1.21	152.0	38.0	2.95	160.3	.75	9
241	5527	267.5	81.1	50.5	22.3	41.2	23.0	.81	1.62	68.7	67.2	4.02	165.1	.62	9
268	5907	270.3	109.7	68.2	33.1	29.4	15.9	.75	1.81	62.3	30.2	4.69	117.8	.62	9
270	2868	267.4	113.0	75.3	13.7	24.3	11.9	.72	1.07	59.1	20.0	3.50	174.6	.67	4,9
278	2819	260.8	109.2	68.3	11.7	31.7	17.8	.74	1.68	38.0	45.4	3.65	145.4	.63	9
291	1198	270.9	47.4	41.3	20.5	30.3	10.3	.85	1.14	146.5	35.7	2.06	130.1	.87	9
326	9925	267.6	213.3	108.2	14.1	22.7	14.9	.60	3.56	0.0	-54.0	5.58	172.0	.51	3,4,9
356	3412	269.0	31.3	21.2	34.8	57.3	18.8	.92	1.14	170.2	46.3	2.24	141.1	.68	9
373	1290	273.7	30.8	18.4	24.8	61.2	18.8	.93	1.07	205.5	19.0	2.04	173.4	.60	2,4,9
383	3215	260.0	197.5	101.9	17.1	29.7	23.3	.61	7.37	46.4	-86.0	3.77	63.7	.52	4

TABLE 5.11.--Kinematics of Dimuons with High $P_{\perp 2}$ (> 1.8 GeV/c)

Run	Event	E_0(GeV)	E_1(GeV)	E_2(GeV)	θ_1(mr)	θ_2(mr)	$Q^2(\frac{GeV}{c})^2$	y	$P_{\perp 2}(\frac{GeV}{c})$	E_H(GeV)	E_M(GeV)	$M_{12}\frac{GeV}{c^2}$	$\Delta\phi_{12}$ degrees	E_2/E_1	Cuts Failed
225	1884	275.6	140.1	46.3	19.3	41.0	21.4	.83	2.35	123.8	-35.0	3.19	71.8	.33	4,6
244	2163	259.9	121.6	40.7	14.3	37.4	14.8	.84	2.03	56.6	41.0	1.64	7.0	.33	6
268	5907	270.3	109.7	68.2	33.1	29.4	15.9	.75	1.81	62.3	30.2	4.69	117.8	.62	9
283	2209	273.2	266.7	10.9	17.3	126.3	47.3	.96	5.32	10.5	-15.0	7.61	149.2	.04	2,3,4, 6,9
283	8150	273.7	131.9	92.7	18.0	18.4	8.6	.66	2.12	124.2	-75.0	3.04	96.1	.70	4,5,9
326	9925	267.6	213.3	108.2	14.1	22.7	14.9	.60	3.56	0.0	-54.0	5.58	172.0	.51	3,4,9
331	6060	267.4	102.5	42.5	16.2	47.0	25.1	.84	1.84	78.0	44.5	3.70	119.1	.41	6,9
383	3215	260.0	197.5	101.9	17.1	29.7	23.3	.61	7.37	46.4	-86.0	3.77	63.7	.52	4
252	6434	255.5	124.1	-90.0	23.4	27.4	17.3	.65	2.04	16.1	25.3	4.81	126.1	.73	3,9
323	2741	279.1	124.6	-96.7	17.5	13.0	4.6	.65	2.43	51.6	6.2	1.34	43.9	.78	4,5

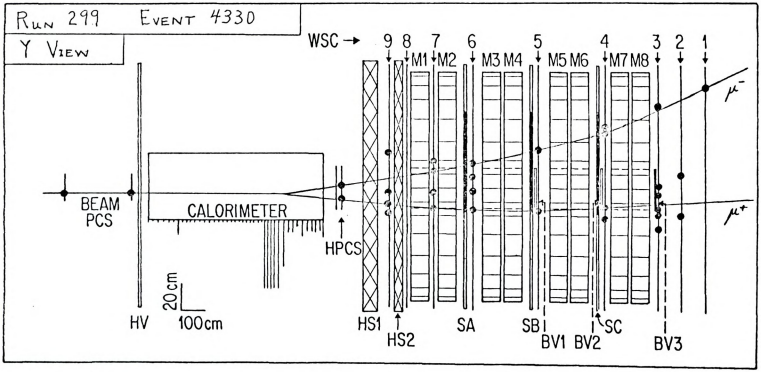

Figure 5.6.--Opposite-Sign Dimuon Event (Possible M° Candidate).

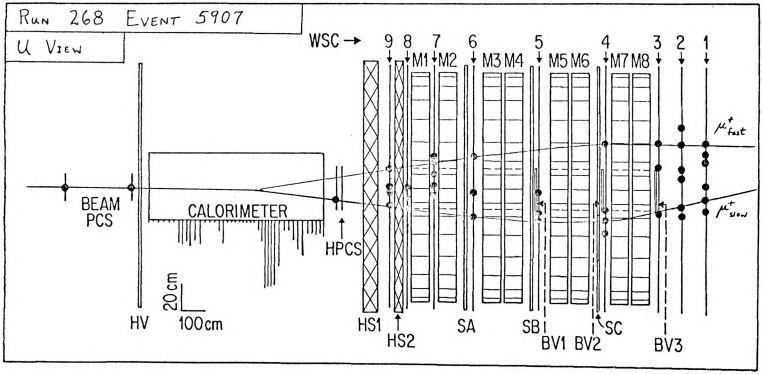

Figure 5.7.--Same-Sign Dimuon Event (Possible k^{++} Candidate).

particularly for the three SSPs with $p_\perp > 3.5$ GeV/c. These events tend to be elastic (low E_H) with negative missing energy, probably resulting from somewhat uncertain momentum fitting (especially on 383-3215). The elasticity suggests these may be mis-identified tridents, although it is possible that vector meson or heavy quark production may be responsible. Figure 5.8 displays one of these events.

Finally, a small-scale effort has been made to examine dimuons from Sample E (incident pions instead of muons) with the hope of: (a) finding a $\psi(3100)$ peak, to allow an accurate check on the calibration of the experiment (the lower mass vector mesons give much broader peaks, amidst large background, making them unsuitable for this purpose) and (b) comparing hadronically and leptonically produced dimuons within the same experimental apparatus. Unfortunately, the incident hadron energy for these runs was limited to 150 GeV, making the realization of either goal difficult. We have analyzed approximately 8% of the Sample E data in the same manner as the muon samples. Figure 5.9 displays the apparent mass and azimuthal opening angle distributions of Sample C (150 GeV muons) vs. Sample E (150 GeV hadrons) while Table 5.12 compares kinematic averages and approximate rates. Clearly, the apparent mass range does not extend as far as the $\psi(3100)$, due to the low incident energy and the poor apparatus acceptance for the low energy muons which result from hadron interactions. While some comparison of muon and hadron induced dimuons may be possible, the low statistics allow

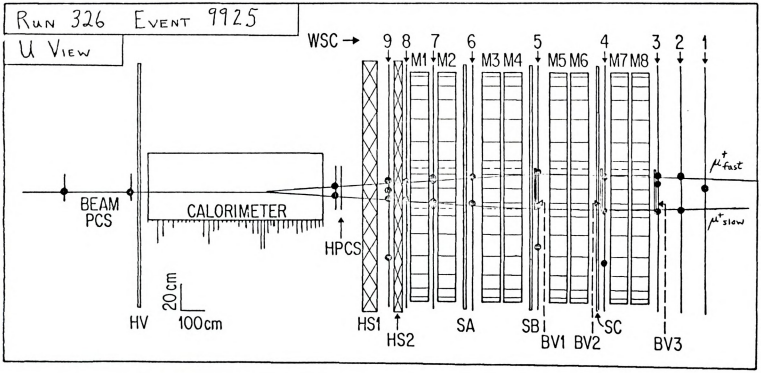

Figure 5.8.--High $P_{\perp}$ SSP (Possible Mis-Identified QED Trident).

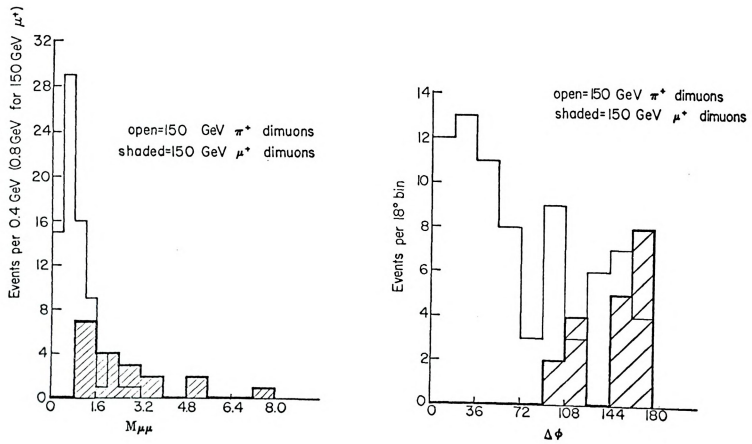

Figure 5.9.--Comparison of Hadron (π^+) and Muon (μ^+) Induced Dimuons at 150 GeV.

TABLE 5.12.--Pion vs. Muon Induced Dimuons

Quantity		Sample C (150 GeV μ^+)	Sample E (150 GeV π^+)	
			Single Tape	Estimated Total
Dimuons	Total	28	76	(988)
Found	OSP	18	64	(832)
	SSP	10	12	(156)
	OSP/SSP	1.8	5.3	
Flux		1.38×10^{9}	9.36×10^{7}	
Luminosity		1.25×10^{36}	2.39×10^{35}	
Uncorrected Rate/Flux		2.0×10^{-8}	8.1×10^{-7}	
Uncorrected Cross Section		2.2×10^{-35}	3.2×10^{-34}	
Averages				
Leading (E_1) Particle Energy		78 GeV	24 GeV	
Produced (E_2) Particle Energy		20 GeV	32 GeV	
4-Mom. (Q^2) transfer squared		5.9 $(\frac{GeV}{c})^2$	3.9 $(\frac{GeV}{c})^2$	
Produced ($P_{\perp 2}$) muon transverse momentum		0.80 $\frac{GeV}{c}$	0.91 $\frac{GeV}{c}$	
Energy ratio ($\frac{E_1}{E_2}$)		5.8	1.1	
Polar Angle ($\Delta\theta_{12}$) Difference		72 mr	40 mr	
Apparent Mass (M_{12})		2.6 $\frac{GeV}{c^2}$	0.9 $\frac{GeV}{c^2}$	
Azimuthal ($\Delta\phi_{12}$) Angle Difference		149 degrees	72 degrees	

only weak conclusions. Since hadron induced dimuons have been experimentally studied in detail,[8] we have not pursued the analysis of the Sample E further.

5.4 Trimuon Events

Trimuons would be the predominant multimuon type in muon scattering if: (a) such events were mostly electromagnetic in origin (because the virtual photon has the quantum numbers of a muon pair) or (b) the semi-leptonic branching ratios of produced hadrons (e.g., D° mesons) were large. However, trimuons are actually an order of magnitude scarcer than dimuons apparently because the purely QED processes are suppressed relative to the hadronic ones and the branching ratios of the produced hadrons are all $\leq 10\%$. Further suppression of trimuons relative to dimuons arises from the occasional loss of a final state muon due to the limited apparatus acceptance, especially at low angles.

The rates and average kinematics of trimuon events are presented in Tables 5.13 and 5.14. The track fixing procedure has not been as successful for trimuons as dimuons, due to spark chamber inefficiency and the tendency for at least one muon to be very near the hole in the spectrometer. Thus, only about half of the trimuons found are completely determined kinematically. Figures 5.10 through 5.12 display some of the kinematic distributions with curves from the QED trident calculation superimposed. Although the leading particle characteristics are not substantially different from those for dimuon events, trimuon produced muons favor larger momenta and

TABLE 5.13.--Trimuon Numbers and Rates

Category	Total	Hadronic (Not Leaky)	Hadronic (Leaky)	Total Hadronic	Leptonic Vertex	Uncertain
Total Trimuons*	64	25	6	31	24	9
Analyzable* Trimuons	36	11	1	12	17	7

Quantity	Sample A (270 GeV μ+)	Sample D (270 GeV μ^-)	Sample C (150 GeV μ+)
Trimuons Found	64	18	3
Trimuons Analyzable	36	7	0
Trimuons Corrected for Losses	72 ($\pm$6)	20 ($\pm$5)	3 ($\pm$2)
Found ($3\mu/2\mu$)	.143	.117	.107
Corrected ($3\mu/2\mu$)	.112	.091	.075
Found (3μ/flux)	5.9×10^{-9}	5.8×10^{-9}	2.2×10^{-9}
Corrected (3μ/flux)	$(6.6 \pm .8) \times 10^{-9}$	$(6.5 \pm 1.6) \times 10^{-9}$	$(2.2 \pm 1.4) \times 10^{-9}$
Found 3μ "cross section:	2.3×10^{-36}	2.3×10^{-36}	2.4×10^{-36}
Corrected 3μ "cross section"	$(2.6 \pm .3) \times 10^{-36}$	$(2.5 \pm .6) \times 10^{-36}$	$(2.4 \pm 1.6) \times 10^{-36}$

*Sample A only.

TABLE 5.14.--Trimuon Kinematic Averages

Average	Sample A		Sample D	
Leading μ Energy (E_1)	152	GeV	97	GeV
4-mom. transfer squared (Q^2)	6.7	$(\frac{GeV}{C})^2$	8.5	$(\frac{GeV}{C})^2$
Hadron Energy (E_H)	22	GeV	30	GeV
Produced μ_2 energy (E_2)	43	GeV	46	GeV
Produced μ_3 energy (E_3)	47	GeV	60	GeV
Transverse momentum ($P_{\perp 2}$) of μ_2 relative to virtual photon	1.1	$\frac{GeV}{C}$	1.6	$\frac{GeV}{C}$
Transverse momentum of ($P_{\perp 3}$) μ_3 relative to virtual photon	1.1	$\frac{GeV}{C}$	1.0	$\frac{GeV}{C}$
Produced Pair Mass (M_{23})	2.3	$\frac{GeV}{C^2}$	2.5	$\frac{GeV}{C^2}$
Polar opening angle ($\Delta\theta_{23}$)	66	mr	59	mr
Azimuthal opening angle ($\Delta\phi_{23}$)	107	degrees	120	degrees
Inelasticity (η)	.10		.24	

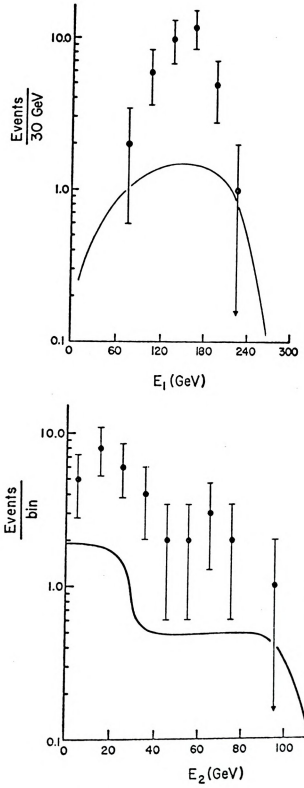

Figure 5.10.--Trimuon Data Energy Distributions versus Calculated QED Trident Results.

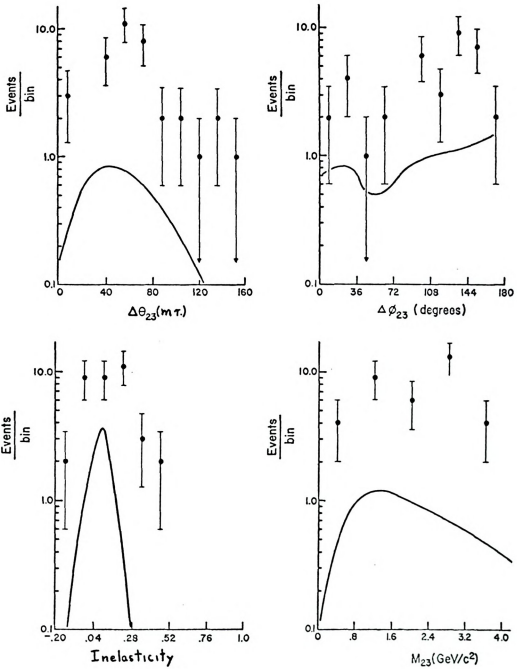

Figure 5.11.--More Trimuon Data Kinematics versus Calculated QED Trident Results (Kinematic Definitions as in Figure 1.1).

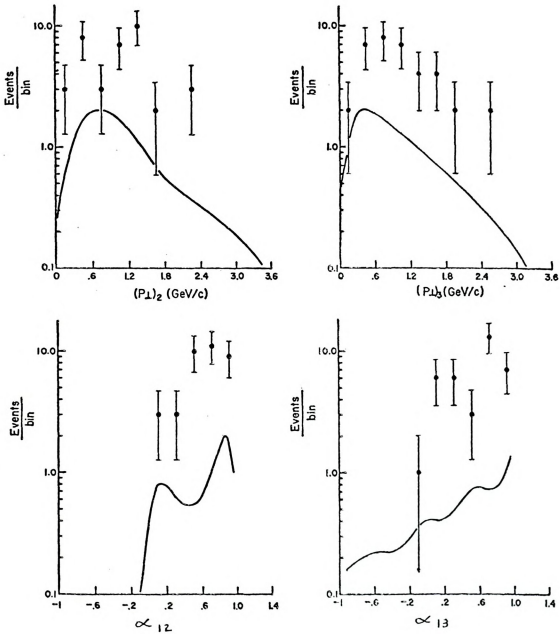

Figure 5.12.--Still Further Trimuon Data Comparisons with QED Trident Calculations.

flatter distributions. The inelasticity distribution suggests an explanation for this; trimuons seem to be primarily elastic, with most of the energy available to the final state muons, instead of the hadron shower. Another observation is that the transverse momentum distributions are much flatter for trimuons (nearly uniform out to 2-3 GeV/c, in sharp contrast to the exponential fall-off characteristic of dimuons) which indicates that hadronic processes do not dominate the trimuon sample. The asymmetry distributions merely indicate that the leading muon remains generally more energetic than either produced muon.

A close examination of the produced pair mass (M_{23}) suggests an enhancement in the bin where $\psi(3100)$ would be expected to appear. Given the mass resolution of about .3-.5 GeV/c^2 in this region, one can perform a smooth fit to neighboring bins, giving a background of 3 events. This could predict 6 ± 3 events to have resulted from $\psi(3100)$ production. Table 5.15 shows the kinematics of the events most likely to be from this process and Figure 5.13 displays one of these events. Clearly, elastic production (with little missing energy) is favored. Furthermore, the events tend to concentrate near a azimuthal opening angle of 180° and have large produced muon energies and transverse momenta. These are all characteristic of the production (at rest in the CM frame) and subsequent two muon decay of a heavy particle. The average apparent mass of 3.1 ± 0.1 for the six events is in good agreement with the accepted ψ mass and gives us confidence (to the few percent level) in the energy calibration of

TABLE 5.15.--Trimuon Kinematics for 6 Probable ψ Events

Run	Event	E_0(GeV)	E_1(GeV)	E_2(GeV)	E_3(GeV)	θ_1(mr)	θ_2(mr)	θ_3(mr)	E_H(GeV)	E_M(GeV)	$P_{\perp 2}(\frac{GeV}{c})$	$P_{\perp 3}(\frac{GeV}{c})$	$M_{23}(\frac{GeV}{c^2})$	$\Delta\theta_{23}$ (mr)	$\Delta\phi_{23}$ (degrees)
225	6530	266.7	159.4	67.5	-25.2	17.7	46.6	40.7	17.2	-2.6	2.21	1.10	3.14	76.2	121.8
271	272	268.1	103.5	28.9	-92.2	20.5	51.9	20.7	21.2	22.2	1.30	1.50	3.11	60.3	106.5
278	5029	270.5	175.4	14.4	-98.9	12.4	55.4	25.3	0.0	-18.0	1.12	0.31	3.04	80.6	170.8
312	6035	275.1	190.6	38.7	-78.4	9.9	31.0	24.4	0.0	-33.0	1.86	1.05	3.00	54.5	161.9
366	3357	271.8	109.6	26.7	-94.2	19.8	51.9	26.9	48.4	- 7.0	1.52	1.29	3.13	62.5	101.1
376	3110	270.2	144.7	57.9	-29.8	11.6	40.4	37.0	19.1	18.7	2.53	1.00	3.17	76.2	160.1

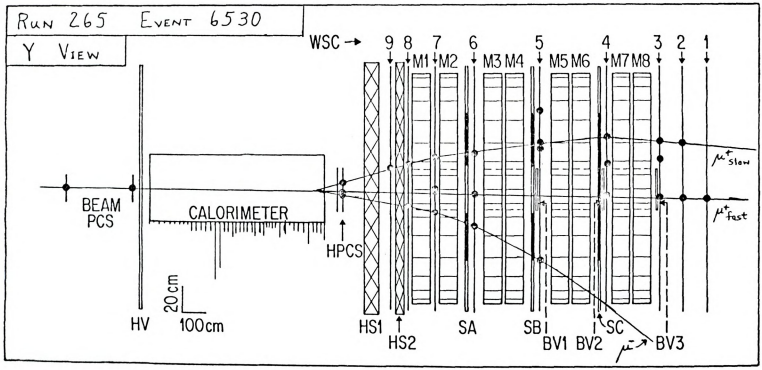

Figure 5.13.--Trimuon Event (Probable ψ Production and Decay).

our experiment. If we make rough corrections for finding efficiency (89%), kinematic losses (50%) and acceptance (estimated from the trident calculation to be 2.5% for the $p_\perp$ values characteristic of the ψ events), the total cross section times branching ratio is calculated to be $(20 \pm 10) \times 10^{-36}$ cm^2, which is consistent with the published muo-production value[9] of $(49 \pm 14) \times 10^{-36} cm^2$, given the large uncertainties in the corrections.

After subtraction of the six events presumed to be from ψ production, Figure 5.14 shows some of the sensitive kinematic distributions for the remaining trimuons, along with estimated hadronic backgrounds from the charm and hadronic recombination processes as calculated by Keung.[10] Clearly, these hadronic mechanisms give trimuons with low produced muon energies and transverse momenta. Although the normalization is uncertain, we can subtract this hadronic background, leaving the small sample shown in Figure 5.15 again with the QED trident calculation superimposed. The kinematics of events most likely to be tridents are listed in Table 5.16 and one such event is displayed in Figure 5.16. Sadly, the low statistics prevents any attempt at extraction of trident cross sections from the data, (which would be a useful extension of such measurements from the previous low energy studies at Brookhaven).[11] Presumably, more recent muon experiments with improved low angle acceptance and higher incident flux will be able to measure trident cross sections, if hadronic backgrounds are not overwhelming.

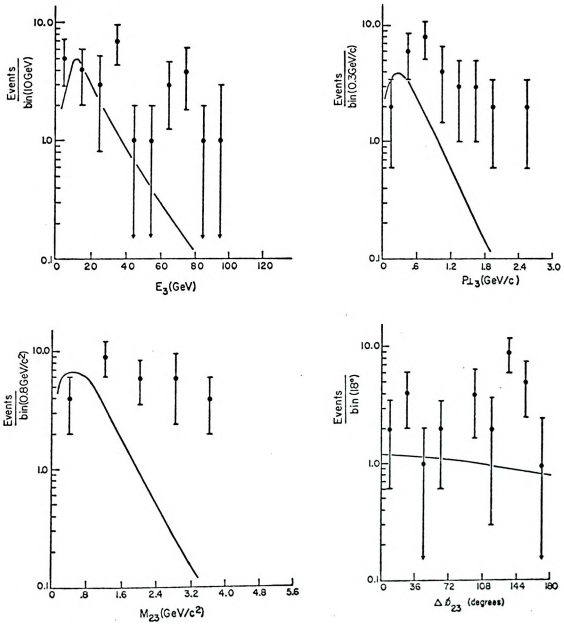

Figure 5.14.--Trimuon Data with ψ Contributions Subtracted versus Total Hadronic Background (as described in the text).

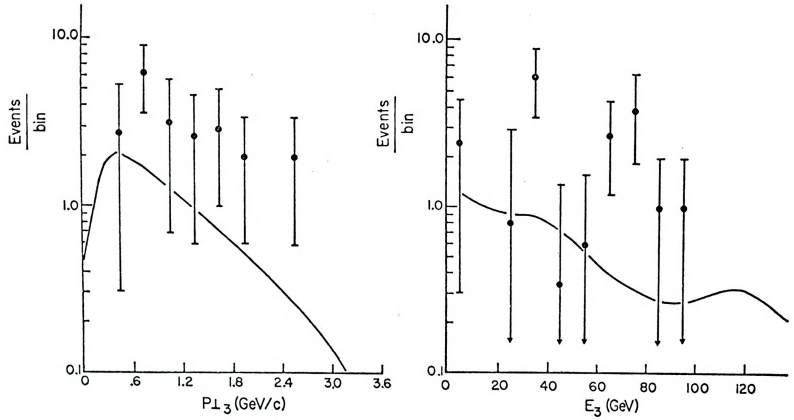

Figure 5.15.--Trimuon Data After Subtraction of All Hadronic Backgrounds versus QED Trident Calculations.

TABLE 5.16.--Trimuon Kinematics for Trident Candidates

Run	Event	E_0(GeV)	E_1(GeV)	E_2(GeV)	E_3(GeV)	θ_1(mr)	θ_2(mr)	θ_3(mr)	E_H(GeV)	E_M(GeV)	$p_{\perp 2c}\left(\frac{GeV}{c}\right)$	$p_{\perp 3c}\left(\frac{GeV}{c}\right)$	$M_{23c^2}\left(\frac{GeV}{c^2}\right)$	$\Delta\theta_{23}$(mr)	$\Delta\phi_{23}$ (degrees)
225	648	266.7	209.3	25.4	-28.6	8.0	68.2	14.0	0.0	3.4	.99	.49	1.50	55.6	23.2
240	2931	249.9	156.3	77.3	-19.9	11.6	20.3	19.8	0.0	-3.6	.39	.76	1.56	40.0	162.9
303	9400	271.5	153.5	132.3	- 4.9	19.6	23.6	60.1	0.0	-19.4	.52	.24	1.35	52.7	59.6
328	5703	270.0	198.4	60.6	-17.8	14.3	37.9	20.7	0.0	- 6.7	.58	.76	1.19	36.3	69.6
346	4952	268.9	134.3	119.1	-23.4	9.1	12.4	41.2	0.0	- 7.9	.94	.98	2.63	49.7	130.1
373	4483	282.6	180.8	64.2	-18.5	9.9	34.8	41.4	0.0	19.1	1.20	.82	2.08	60.4	102.7
376	1310	271.6	160.6	22.6	-70.0	11.1	20.9	21.3	8.8	9.6	.13	.47	.33	8.2	22.0

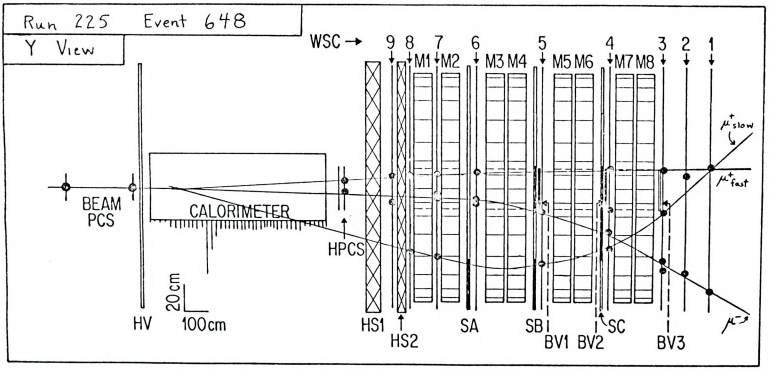

Figure 5.16.--Trimuon Event (Probable QED Trident).

5.5 Exotic Events

Several physical mechanisms (including double tridents, heavy lepton combined with heavy quark production or charged heavy lepton pair production) have been discussed in the literature[12] for the production of events with more than three final state muons. Although, the improbability of this has ruled out any systematic search for such events, calorimetric information for dimuon and trimuon events has pinpointed one event (332 - 75) which may have four final state muons. However, the tracks and calorimeter analysis are ambiguous as to whether the possible fourth muon penetrates into the spectrometer. Again, the more recent, high luminosity experiments should see these exotic events, if they are produced in muon interactions.

CHAPTER 6

CONCLUSIONS

6.1 Introduction

The concluding chapter of this dissertation has three objectives: (1) to summarize the methods and results of experiment E319 pertaining to leptonic sources of multimuon events (primarily QED tridents and heavy leptons); (2) to discuss changes in the apparatus and data-taking of E319 which would have improved the multimuon sample without substantial expenditures of time or money; and (3) to suggest general principles for the design of further multimuon studies and compare these requirements with the status of third generation experiments already in progress.

6.2 Summary of Multimuon Results

Although neither experiment was explicitly designed to study events with more than one final-state muon, such multimuon events have been found, at low levels initially in E26, and in substantially larger numbers from E319. Several possible explanations have been proposed for the existence of muon-induced multimuons. The most likely source of such events is the virtual photoproduction of hadrons, either singly (e.g., $\mu N \rightarrow \mu \pi X$, $\pi \rightarrow \mu \nu$) diffractively (e.g., $\mu N \rightarrow \mu \Psi X$, $\Psi \rightarrow \mu\mu$) or in pairs (e.g, $\mu N \rightarrow \mu D^0 \bar{D}^0 X$, $D^0 \rightarrow k\bar{\mu}\nu$, $\bar{D}^0 \rightarrow$ hadrons). While all of these hadronic processes are

suppressed due to the low branching ratios of the hadrons into muons, recent models (e.g., photon-gluon fusion) suggest that they may still dominate multi-muon production. Associated charm production ($D^0\bar{D}^0$) seems especially favorable. A second type of process which results in multi-muon final states is the weak production of neutral ($\mu N \rightarrow M^0 X$, $M^0 \rightarrow \mu^+\mu^-\nu$) or doubly charged ($\mu N \rightarrow k^{++}x$, $k^{++} \rightarrow \mu^+\mu^+\nu$) heavy leptons. Most gauge theories which purport to combine weak and electromagnetic interactions contain such heavy leptons (although the currently favored Weinberg-Salam model does not). While such particles have not yet been found, the experimental limits are not particularly strict. A final category of processes which may contribute to multi-muon events involves the direct electromagnetic pair production of muons (or possibly charged heavy leptons) via Bethe-Heitler, bremsstrahlung or Compton mechanisms. Quantum electrodynamics allows the calculation of these processes and indeed muon trident production has been observed at low energies in good agreement with the prediction. Scaling these results to E319 energies predicts small, although not negligible, event rates.

The apparatus for experiment E319 can be functionally divided into three major parts; incident muon detection, interaction vertex and shower energy measurement, and final state muon detection. The beam muon was detected via a system of scintillation counters and multi-wire proportional chambers which give good spatial (and timing) information, as well as a momentum analysis from the last beam line magnet. The incident muon energy could be varied from 25 to 270 GeV with a typical intensity of 5×10^5 muons per spill.

Halo was vetoed at the front of the target. The event vertex and shower energy were measured via an iron-scintillator hadron calorimeter, which also served as the target. Calibrated with hadrons of known energy, the calorimeter showed good linearity and an energy resolution ranging from 5% at high energies to 25% at very low energies. The sampling frequency localized each event vertex longitudinally to within a few centimeters. Finally, the muons emerging from the interaction were detected and momentum-analyzed by eight toroidal iron magnets and nine wire spark chambers. Scintillation counter banks provided triggering and timing information. The energy resolution of this magnetic spectrometer averaged about 10%. Muon energies could be measured with good efficiency from 5 GeV to 250 GeV and muon scattering angles from 10 mr to 150 mr were accepted.

The low produced muon energies and small leading muon angles characteristic of multimuons found in both experiments suggested the need for a new analysis program capable of working from the front of the spectrometer. Developed over an extended period of time with constant feedback from the growing multimuon sample, this track reconstruction program MULTIMU has become the main data analysis tool for all aspects of E319. Combined with the time-consuming, but effective, visual scanning procedures and the vertex and muon detection capabilities of the calorimeter, this has proved to be an efficient method for finding and analyzing multimuon events. With the addition of detailed manual reconstruction of some events, the overall finding efficiencies were determined to be $(70 \pm 7)\%$ for

dimuons and (89 ± 7)% for trimuons. Roughly 92% (56%) of the dimuons (trimuons) were kinematically analyzable in full with losses primarily due to poor acceptance of low energies and small angles.

The drastic effects of experimental acceptance on model predictions for E319 have necessitated Monte Carlo simulations of the dominant multimuon processes, including associated charm production, shower pion (kaon) decay, and QED tridents. Close collaboration with theorists from the University of Wisconsin has supplied independent checks for these and several other possible mechanisms. While the kinematic distributions of the Monte Carlo calculations are generally believable, absolute normalization is much more uncertain, especially for the charm models. This hampers the background subtractions needed to study the small leptonic signals expected from QED trident or heavy lepton production. Because of the low rates predicted for the heavy lepton processes and the uncertainty in model predictions, I have chosen to search for them using direct kinematic tests applied to the data, instead of elaborate Monte Carlo simulation.

The multimuon results presented in Chapter 5 indicate that hadronic processes (particularly charm production) account for the bulk of dimuon events, as evidenced by the comparison of experimental kinematic distributions and rates with those calculated by the Monte Carlo simulation. Although subtraction of these hadronic predictions is an uncertain proposition due to the normalization difficulties, the resulting distributions agree reasonably well with Monte Carlo

predictions for QED tridents, allowing for the acceptance loss of one final state muon. A very few large transverse momentum dimuons remain, which may be from heavy lepton (or heavy quark) production. Application of kinematic cuts, designed to select neutral heavy muons (or possibly doubly charged heptons) out of a large hadronic background, yields a few candidates. However, normalization uncertainty and the large overlap between kinematics preferred by heavy leptons and tridents make firm conclusions untenable. Accepting the hypothesis that the most likely of the candidates is truly a neutral heavy lepton yields a cross-section estimate consistent with the best upper limit published.

Trimuons, although an order of magnitude less numerous than dimuon events, are also not so severely dominated by hadronic processes (roughly 50% as opposed to over 95% for dimuons). We have identified 6 ± 3 events in the apparent mass distribution, which appear to derive from the production and two-muon decay of the $\Psi(3100)$ meson. Subtraction of these events, and the calculated charm and hadronic recombination backgrounds, yields kinematic distributions which agree reasonably well with QED trident predictions, within the uncertainties. There is little evidence for other processes in the trimuon sample. One exotic event with possibly four final state muons has been found, but the kinematics are not fully-determined, leaving only speculation about its origin.

6.3 Improvements in E319

E319 was originally proposed as a further study of deep-inelastic muon scattering designed to extend tests of Bjorken

scaling to larger q^2. The discovery of multimuon events had a considerable influence on the final planning and experimental conditions of E319, especially in the placement and use of spectrometer detectors such as the hadron proportional chambers and trigger banks. However, the need to minimize the impact on deep-inelastic studies necessitated some unfavorable apparatus features for multimuon work, including: (1) poor detection immediately after the target due to the small size of the hadron proportional chambers and the rate limitations of the front spark chambers; (2) full magnetic field in each toroid causing low-energy produced muons to be bent out of the spectrometer too quickly or, worse, into the veto counters; and (3) inappropriate design of the trigger bank and veto counters in the hole region favoring rejection of the typical low angle leading muon. These problems are most severe for QED tridents and electromagnetic processes in general, and least troublesome for heavy particle production (e.g., charm or heavy leptons).

The simplest solution to all such difficulties is to take more data and attempt to work around the problem in analysis. However, due to demand for the neutrino and muon beams, this option was unavailable for E319. In the following, we detail some apparatus changes which would have enhanced the multimuon aspects of E319, at minimal expense to the deep inelastic studies.

The acceptance problems could have been ameliorated by simply shifting some of the spectrometer detectors to different

positions. Given the success of the MULTIMU analysis at track reconstruction from the front of the spectrometer, the back two spark chambers were unnecessary and could have easily been shifted to the front, giving greater detection redundancy. It might have even proved feasible to offset some of these chambers to improve wide-angle muon detection. With increased shielding in the toroid holes, the last beam veto (BV3) would also have been unnecessary, and its elimination would have prevented the tendency for low-energy positive muons to bend back into the hole and veto events. Trigger bank detection could have been extended further into the hole, allowing a much more efficient multimuon trigger to be formed and greatly aiding analysis of these events. Trident production, being primarily low angle by nature, is not well-suited to an experiment with a central hole and veto, but heavy particle production could have been preferentially selected by triggering on high transverse momentum inelastic events (perhaps with the aid of the calorimeter). Although little could have been done about the low rate capability of the spark chambers, a reduction in event rate from more selective triggering, or a reduction in the muon beam halo would have greatly lessened the effects. However, it is clear that the proposed heavy lepton rates still would not have been substantially improved without a large increase in incident flux.

6.4 Third Generation Muon Experiments

Based on our experience with multimuons, I believe that future experiments must employ the following: (1) an improved muon

beam (with higher rate or at least lower halo); (2) proportional or drift chambers in place of the slow spark chambers, especially to improve multi-track efficiency; (3) more flexible triggering schemes to enhance multimuon signals and simplify event finding and (4) improved acceptance, both at low angles and energies and at large angles. Third generation muon experiments have already taken considerable data both at Fermilab (E203) and CERN (NA2 and NA4). E203 has taken the novel approach of making the target and spectrometer part of the same detector, giving excellent angular acceptnce. Furthermore, they use proportional chambers and employ several multimuon triggers which make use of calorimeter information. However, they use essentially the same muon beam as E319. The CERN experiments have the advantage of a fantastic muon beam (10^7 muons per spill with only 10% halo), but use fairly conventional target and spectrometer arrangements, which may not represent a large improvement in acceptance over our experiment. All of these experiments have roughly an order of magnitude larger incident flux than E319, and, with the apparatus improvements mentioned, they should isolate multimuons from heavy leptons if the cross sections are not substantially lower than current upper limits. Should these experiments fail to detect heavy leptons, the discovery may have to await the construction of the proposed Tevatron muon beam at Fermilab.

APPENDICES

APPENDIX A

THE HADRON CALORIMETER

APPENDIX A

THE HADRON CALORIMETER

A.1 Theory and Design Considerations

The use of the measurement technique called calorimetry is conceptually as simple in particle physics as in its original chemistry applications. The basic idea is to obtain a measure of the energy released in a process by immersing it in a suitable medium which samples that energy in a proportional manner. In place of the temperature measurements used for chemical reactions, however, particle calorimeters must determine the number of particles produced in an interaction which can be related to the energy involved. Such techniques were first used in cosmic ray experiments[1] where typical particle energies are often far too large for conventional magnetic energy measurements. More recently, the advent of high energy accelerators and neutral beams has made calorimetry even more attractive. A variety of forms have evolved depending on the energy and composition of the particle showers to be measured.[2] Neutrino experiments in particular have pioneered the sampling calorimeter used to measure hadron showers in which scintillation detectors are interspersed with heavy target plates (usually iron).[3] The target acts as the medium with which the incoming beam interacts and the scintillators then sample the spatial distribution of the resulting

shower of hadrons and thus obtain a measure of the energy deposited. If the incoming beam consists of neutrinos, the hadron shower energy can be used to determine the neutrino energy. Alternatively, if the incoming particles are charged so that their energies are already known, the shower energy can be used to determine if there is any "missing energy" carried away by produced neutrinos. The previous muon experiment E26 was equipped with a few scintillation counters in its iron target partly for this reason. However, the small size and inadequate pulse height range of the counters effectively prevented their use for calorimetry. From the experience gained there, and the published neutrino calorimeter work, came the motivation and the necessary information to build a hadron calorimeter for the present muon scattering experiment.

The E319 hadron calorimeter was designed with three functions in mind: (a) to improve the energy resolution of the apparatus for events with large energy transfer to the virtual photon; (b) to determine the interaction point along the beam direction with better spatial resolution; and (c) to measure missing energy for multimuon events. Achievement of these goals required that the calorimeter be made sufficiently wide (51 cm) and long (738 cm) to contain hadron showers with energies up to 200 GeV. Furthermore, the sampling distance (i.e., the width of the target plates) had to be small enough (4.8 cm) to give good spatial and energy resolution without making the cost astronomical. The choice of iron for the target material was a compromise between minimizing multiple scattering and

energy loss (which increase with atomic number) and maximizing the ability to sample hadronic (relative to electromagnetic) showers. Aluminum and polyethylene targets were also purchased to allow tests of nucleon number dependence for muon scattering and multimuon production, although lack of beam time prevented their use.

The detectors in the calorimeter needed to respond to the anticipated large range of shower hadrons with good spatial uniformity and linearity. The relatively new plastic scintillation material NE110 seemed to be the cheapest way to satisfy this demand. To match the spectral output of this material, ultraviolet transmitting lucite was used for all light guides and special glues were used to form the resulting counters.

The choice of photomultiplier tube was complicated by the need for a high degree of stability with time, so that constant gain checks would not be needed. Most of the common tubes used in high energy applications were found to be rather unstable, especially at large anode currents. The least expensive compromise turned out to be the new RCA 6342A, which tests had shown to be stable over sufficient lengths of time and large light levels.[4] About twice as many tubes were purchased as were actually used to allow the selection of only the ones with good signal-to-noise ratios and minimal instability. The tube base electronics were taken from standard designs used successfully on other ten stage phototubes. Direct measurement during the data runs convinced us that dynode voltage sagging was negligible.

Analog-to-digital converters (ADCs) were used to convert the voltages from the phototubes into the digital form needed by the computer. Two methods were considered for achieving the large dynamic pulse height range needed: (a) use a single logarithmic response ADC for each counter, or (b) use two linear response ADCs each with a different amplifier gain, for the same counter. This second option allows a broader range, with the same resolution and easier analysis, so it was chosen. The fast amplifiers needed to take the tiny phototube signals (10 to 100 mv, 20 ns long) and convert them into signals more compatible with ADCs (100-1000 mv) were patterned after a working design of Sippach. The actual choice of ADC was for all practical purposes determined by the necessity of having 220 total channels. Only the new Lecroy 2249A, with 12 channels per module, seemed feasible.

Finally, a target cart had to be built which would allow movement of the enormously heavy calorimeter (10.6 metric tons) along a set of rails to give maximum flexibility in target placement. The iron plates were constructed to hang freely along rails in the target cart with the counters sandwiched vertically in between. The aluminum frames of the counters maintained close and uniform packing, minimizing air gaps which might allow shower leakage.

A.2 Construction

All of the scintillation counters, tube bases, and amplifiers for the calorimeter were built at MSU while Fermilab supplied the ADCs and high voltage supplies. Among the many problems involved

in making large scintillation counters for pulse height measurement, the worst is non-uniform light attenuation from the point of passage of the particle to the phototube. This is really a two-fold problem since the absorption or scattering of light can result either from the actual geometry of the counter, or from construction techniques such as polishing and gluing. This is further complicated by the fact that light from scintillator is primarily ultraviolet, which is difficult to transmit through many materials and scatters easily. This section describes some of the techniques used to construct scintillation counters for E319.

The scintillation plastic arrived already cut to the proper size and polished on all sides. Very careful handling was necessary to minimize crazing due to heat, stress, and chemicals. The light pipes consisted of two pieces: (a) a trapezoidal piece of lucite to funnel the light from the 20 inch scintillator edge to a flat 12 inches, and (b) seven stripes of lucite twisted separately to transport the light into a roughly 2 inch circle which matches the phototube aperture. All of this lucite was machined and tediously polished on the sides to preserve the total internal reflecting quality and reduce scattering of light. However, the faces to be glued were not polished, since a better glue joint results if the surface is slightly rough.

A counter was then put together in the following way. First, the lucite strips were made flexible by heating in an oven and carefully twisted into the proper shape by a jig. They were then bonded together by a solvent bond cement (called H94 from Almac Plastics,

Co., Grand Rapids, Michigan). Next, the lucite trapezoid was glued to the strips using a special non-yellowing epoxy (called PS30). The gluing was done horizontally with a jig constructed to apply some pressure to strengthen the joint and suppress air bubbles. If the quality of the joints was visually bad, they were easily broken and reformed. The scintillator was then attached using the Nuclear Enterprise optical cement NE580. Here the gluing was done vertically, using gravity to squeeze out air since it was found that this pressure was crucial to the optical quality and strength of the joint. Finally, the counter was wrapped to keep extraneous light out, using a combination of an inner layer of aluminum foil and outer layers of black vinyl plastic and tape. The assembled counter was then placed gently into its aluminum channel frame and secured at the top by a clamp arrangement to provide mechanical stability and allow easy handling. The phototubes were separately wrapped in aluminum foil and black tape. They were then secured to the face of the light pipe simply by strapping tape, since it was decided that grease or glue couplings were too unstable. In order to shield the photocathode from potentials in the outside world, the aluminum foil wrapping of the tube was tied to the cathode high voltage via a current limiting resistor. Finally, the vital magnetic shielding was provided by commercial mu-metal shields to protect the sensitive dynode chain focusing. This completed the construction for one counter and the process was repeated at least 110 times over a space of approximately 6 months to build the whole calorimeter.

To conserve money, the tube base and amplifier circuits were all made in-house at MSU. The amplifiers were placed four to a printed circuit board of Camac size. This unfortunately contributed to some cross-talk problems between channels and was not the most optimum design. However, the modularity and use of bussed card voltages allowed for easy replacement and repair.

A.3 Testing

Since the calorimeter counters were required to provide absolute pulse height information, it was essential to test their spatial uniformity, linearity with respect to energy input, and stability with time. Of course, each counter was first verified to be light-tight by simply watching the noise signals under dark and light room conditions and taping suspect spots. Then, using several beta sources of differing energies, the uniformity of response at several points on the scintillator was checked. The spectral shape of the pulse height for each source is well known and degradation of that shape is usually a sign of poor light transmission. Several counters were broken apart and re-glued to reduce their non-uniformities to the 10-15% level which seemed typical of this counter geometry. Although techniques exist to further suppress such variance by selective absorption of ultraviolet light, it was felt that this would be unnecessary since calibration data over the whole face of the calorimeter could be readily used to correct for non-uniformities.

The next test involved the use of cosmic rays to study the response of the counters to minimum ionizing muons. It was hoped

that this would determine the voltage and relative gains of all the counters and perhaps the single muon resolution. However, the fast 2249A ADCs were not available at this time and the cosmic ray rate of around 10 counts/sec. was insufficient to really pin down the gains. Still the information obtained was a great aid in later calibration efforts.

The first attempt to understand the energy response of these counters involved the use of the 50 MeV proton beam of the MSU cyclotron. The procedure was to vary the beam energy by using absorbers and then to plot energy deposited in the scintillator versus light output (measured as signal voltage times width). The test showed good linearity for absorbed energies between 10 and 30 MeV, with deviations due to straggling and signal mismatches between counters and analyzers. These tests were not pursued further since the most important linearity curve would be the response of the whole calorimeter to incoming high energy hadron beams (see section A.4).

Finally, halo muon tests were made at Fermilab just prior to the running of E319. These muons resulted from an upstream hadron experiment and were used essentially as an intense cosmic ray test. Since the proper ADCs were now hooked up, the counter voltages and gains were set using these muons. To obtain the desired pulse height range, it was necessary to make the high gain amplifier channels with a gain of around 35 and the low gain channels with a gain around 1. Then, with counter voltages between 1200 and 1500 volts, the

single muon peaks appeared in channel 50 for the high gain channels and channel 10 for the low gains.

LEDs were mounted on each scintillator, supposedly to provide a monitor of the stability of the counters during the data taking. However, the LED signals were badly mismatched for the ADC range and, even worse, there was no feedback to insure that the LEDs themselves were always giving the same amount of light. Due to severe time pressure, it was decided to use single muon peaks as monitors of the calorimeter stability. Although somewhat broad, these peaks verified that the whole calorimeter system was stable over the course of the data run to within 10% except for one deliberate shift. During the first set of data runs, it was discovered that noise from the spark chambers was able to feed into the ground paths of some of the ADCs and turn their gates back on, scrambling some of the pulse heights. To correct this for the later data, tiny ferrite core transformers were placed on all inputs to the ADCs to absorb the spark energy induced. This had the effect of a downward shift of the calorimeter calibration which was measured and corrected for in the analysis. We understand that LECROY has since modified their design for the 2249A ADC to prevent such occurrences.[5]

A.4 Calibration

Energy calibration of the hadron calorimeter was obtained by using incident hadron beams of known energy which create hadron showers at a much higher rate than incident leptons. The assumption in our case is that the showers develop in much the same manner,

independent of the incident particle type. The calibration then required correlation of the 220 ADC readings with the number of charged particles present. This presumes knowledge of the response of each counter to no incoming particles (called the pedestal level) and one minimum ionizing particle. Pedestals were monitored throughout the experiment by deliberately writing out events when no beam was present, while single muon peaks were obtained simply by triggering on unscattered incident muons.

In the analysis, pedestals were determined then by averaging the raw ADC channels over the roughly 1000 events on each of the 38 pedestal runs, with bad channels corrected from other runs. The pedestals range from channel 4 to channel 12 with the typical value being around 7. The width of the pedestal peaks is usually less than 2 channels. Single muon peaks were partially obtained in the same manner for the 7 unscattered muon runs. However, in place of averaging, the peaks were fit by Gaussians since straggling biases the means more than the peaks of these distributions. This procedure worked well for the high gain channels, but failed for the low gains, where the muon peaks were crowded into very low channel numbers near the pedestal. However, by measuring the relative gains on the high and low gain channels, it was possible to calculate the low gain muon peaks by the formula:

$$\text{(Low Peak)} = \text{(Low Pedestal)} + (\text{(High Peak)} - \text{(High Pedestal)})/\text{Relative Gain}$$

Now, with the 0 and 1 particle responses known, it was simple in principle to correlate energy with pulse heights. The ADC channel numbers were first converted into equivalent particles by the formula:

Particles = (ADC reading - Pedestal)/(Muon Peak - Pedestal)

This set the scale for the energy calibration, which is then simply the slope of a plot of the sum of the equivalent particles in the calorimeter shower versus the known incident energy. Detailed studies of shower development have shown that the poorly sampled parts of the showers do not prevent a linear calibration although they do broaden the resolution somewhat. However, even a small leakage of the showers can significantly alter the calibration and we made careful studies of shower containment in our data.

Table 3.1 summarized the hadron calibration data taken for E319. The first period was essentially a shakedown run for the calorimeter with the object being to compare its response to similar devices and settle the final configuration. Longitudinal spatial response was of particular concern, so several sub-sections of the calorimeter were separately studied. Little difference was detected between the response of the sub-sections and the whole calorimeter, implying that even the highest energy showers were well contained within about one third of the calorimeter. This was not true of the runs made with aluminum and polyethylene targets where clear leakage effects were seen at high energies. Problems with some calorimeter

channels, uncertain beam energy determination, and very high incident hadron rates (which give large tails on the distributions) prevented the use of this early data for actual energy calibration.

A second period of hadron calibration, just before the main muon runs, focused solely on obtaining a good energy calibration for the full iron target. A negative hadron beam was used due to its lower rate and the fact that it consisted primarily of pions without the large component of protons present in the positive beam. Five energies ranging from 25 GeV to 225 GeV were studied (the beam line was unable to give reasonable fluxes outside this range).

Finally, a third set of calibration runs were made near the end of the experiment in order to study how the ferrite cores affected the calibration and to determine the stability of the response with time. Further tests were also made on potential rate effects, spark chamber noise influence, and spatial uniformity of the calorimeter as a whole.

The final algorithm for determining the calibration constants and resolution of the calorimeter began by decoding all high and low channel ADCs and converting the numbers to equivalent particles. Then a search was made for showers, with the definition being at least four consecutive counters with greater than 10 equivalent particles present in the high gain ADC channels. The vertex is then the first counter of the largest shower. This procedure was complicated by the presence of noise spikes and missing channels, with recovery methods needed to find some showers. To calculate the energy of each shower, the equivalent particles of all counters

within the shower plus two on either side were summed. Normally, the low gain ADCs were used, since the high gain signals overflow at around 20 particles. If the last two counters in the target had signals exceeding 10 particles, the shower was labeled as leaky and its energy not trusted. Histogramming the resulting equivalent particle sums gives a Gaussian distribution to a good approximation. The peaks of these distributions were plotted versus the mean incident hadron energy to form the calibration, while the widths gave a measure of the calorimeter energy resolution. The results of this analysis on the second and third sets of calibration data are shown in Table A.1 and in Figures A.1 and A.2. Furthermore, Table A.2 compares our calibration and resolution with that for similar calorimeters.[3,6] The calibration seems quite consistent with the published data, although our resolution is somewhat worse than might be expected. This problem was studied by making a whole series of geometric and shower cuts on the hadron data, looking for factors which affect the widths of the distributions. It was found that showers which start later in the calorimeter and extend over more counters have better resolution, as shown in Figure A.3. This implies that short, electromagnetic showers were often present at the front of the calorimeter and these seem to be inadequately sampled. A more complete understanding of this problem would have required more extensive calibration data which we were unable to obtain. Nevertheless, disagreements with other experiments and published Monte Carlo calculations[7] were all less than 10% which gave us

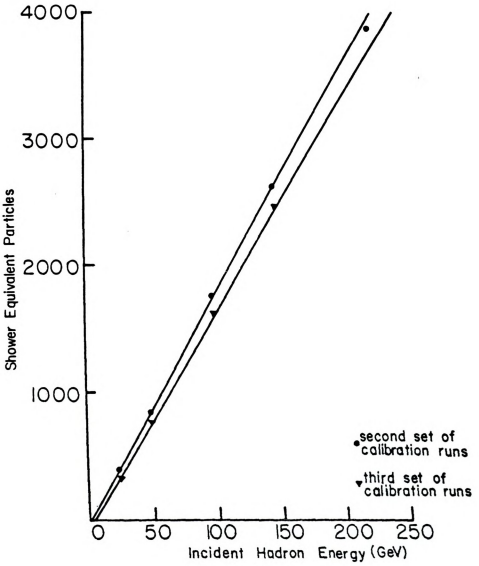

Figure A.1.--Hadron Calorimeter Energy Calibration.

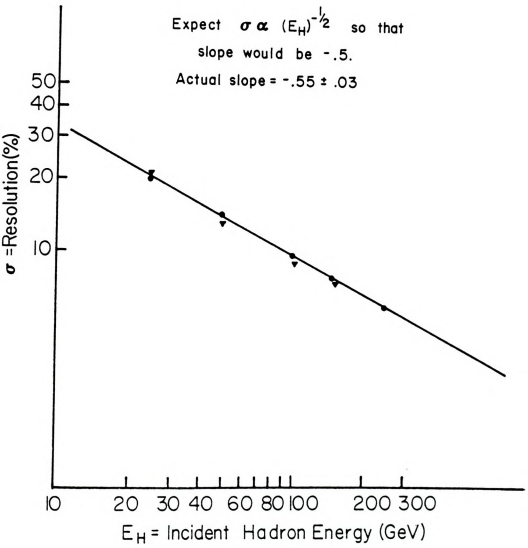

Figure A.2.--Hadron Calorimeter Energy Resolution (Dots are from second set of calibration runs and triangles are from the third set).

TABLE A.1.--Summary of Hadron Calibration Results for E319

Run Nos.	Incident Hadron Energy		Calorimeter Shower Equivalent Particles					
			Peak (ep)			Resol. (%)		
	Peak (GeV)	Resol. (%)	A	B	C	A	B	C
2nd Calibration, Last 2/3 Iron Target, π^- incident, old ADC patch panel								
163, 165	228.4	0.7	3708	3796	--	5.3	5.5	--
166, 167	99.6	0.9	1682	1741	--	9.2	9.5	--
168	24.6	1.6	383	421	--	20.1	15.7	--
169, 170	149.5	0.8	2527	2597	2490	7.2	7.6	6.7
172	49.4	1.1	823	885	--	13.8	13.8	--
2nd Calibration, Full Iron Target, π^- incident, old ADC patch panel								
173	224.6	0.8	4066	4079	3928	6.2	7.5	5.5
174	24.6	1.6	395	410	419	19.8	16.6	16.7
175	99.6	0.8	1832	1833	1792	9.7	10.6	8.7
176	49.5	1.2	875	894	890	14.1	14.2	12.4
177	149.8	0.8	2751	2763	2676	7.9	8.7	7.0
3rd Calibration, Full Iron Target, π^+/p incident, new ADC patch panel								
558	101.5	1.4	1617	1663	1672	8.7	8.8	8.5
560	50.3	2.0	767	808	815	12.9	12.1	12.4
563	24.6	3.6	340	377	384	20.5	16.6	16.2
564	151.6	1.3	2454	2504	2517	7.3	7.4	6.1

A = Standard shower algorithm with no cuts.

B = Allow only events with single shower found and not leaking out the back of the calorimeter.

C = Also require that the shower start well into the calorimeter and that the first two counters are quiet.

TABLE A.2.--Comparisons with Other Hadron Calorimeters

Incid. Hadron Energy (GeV)	CERN[a] (t=5cm)		CALTECH[b] (t=10.16cm)		E319[c] (t=4.76cm)		Expected E319[d] σ from	
	ep	σ(%)	ep	σ(%)	ep	σ(%)	CERN	CALTECH
5			18	38.4				
10			53	33.1				
15	234	20.3						
20			106	25.3				
25					419	16.7	15.7	15.1
30	496	14.7	165	19.9				
50	865	11.7	269	15.8	890	12.4	11.4	10.8
75	1326	9.6						
100	1725	7.8	538	11.1	1792	8.7	7.6	7.6
140	2449	6.9						
150			808	8.9	2676	7.0	6.4	6.1
200			1056	7.9				
225					3928	5.5	5.3	5.1
250			1287	7.3				

[a] see Reference 1.

[b] See Reference 2.

[c] From the 2nd calibration runs 173-177 with the full set of cuts C listed in Table A.1

[d] Assuming $\frac{\sigma(t_1)}{\sigma(t_2)} = \sqrt{\frac{t_1}{t_2}}$ where t is the sampling thickness;

σ is the resolution (= FWHM(ep)/2.355 peak(ep)) and ep means equivalent particles.

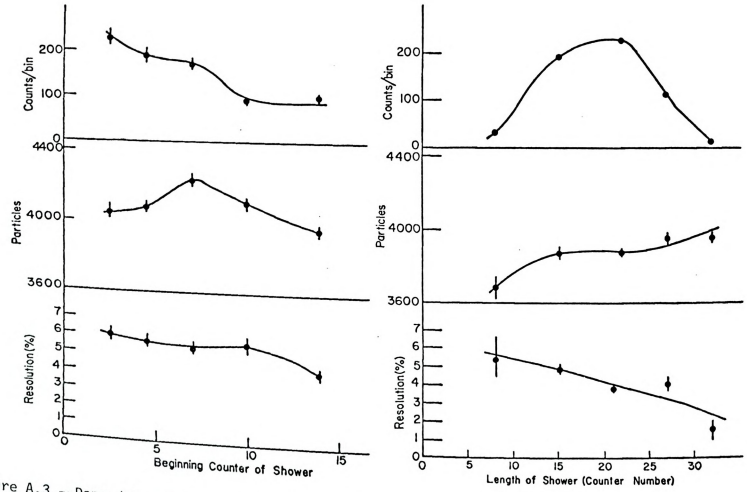

Figure A.3.--Dependence of Calorimeter Response on Position and Length of Hadron Showers (for a typical 225 GeV π^- incident calibration run).

confidence that the calorimeter information would be useful in the muon data analysis.

A.5 Uses of Calorimeter Information

In this section, I will evaluate how well the calorimeter data for the muon runs lived up to expectations, especially for multimuon events. The easiest objective was to determine, with good resolution, the event vertex along the beam direction (called ZADC). Figures A.4, A.5, and A.6 show the distributions in ZADC for single muon, dimuon, and trimuon events respectively. Clearly, the multimuons prefer more downstream vertices, mostly because the muon acceptance is better there. Also, both beam pion and shower pion decay origins of multimuons are essentially ruled out here because the events would then be strongly peaked at the front and back of the target, respectively. The ZADC vertex distributions agreed very closely with those obtained from muon track information, but supplied better spatial resolution.

By averaging the high gain signals for counters well before the shower, the number of muons entering the target could be obtained. The number of muons exiting the target was available in a similar manner, as long as the shower was not too close to the end. Figures A.7, A.8, and A.9 show the distributions of these muon numbers for single muon, dimuon, and trimuon events. Although shower straggling supplies large tails on these distributions, it is clear from the ratio of leaving to entering muons that our multimuon assignments were correct.

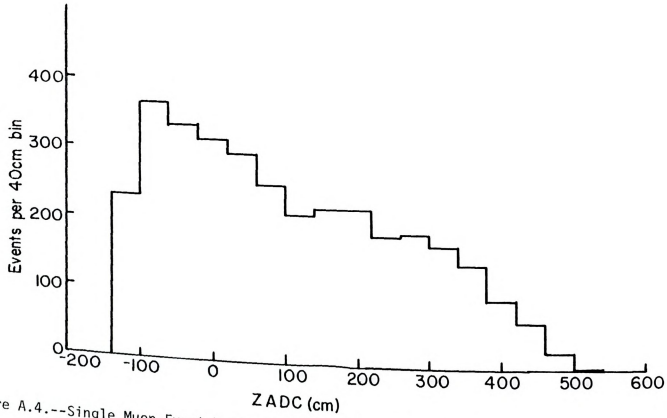

Figure A.4.--Single Muon Event Vertex Positions from the Calorimeter (ZADC).

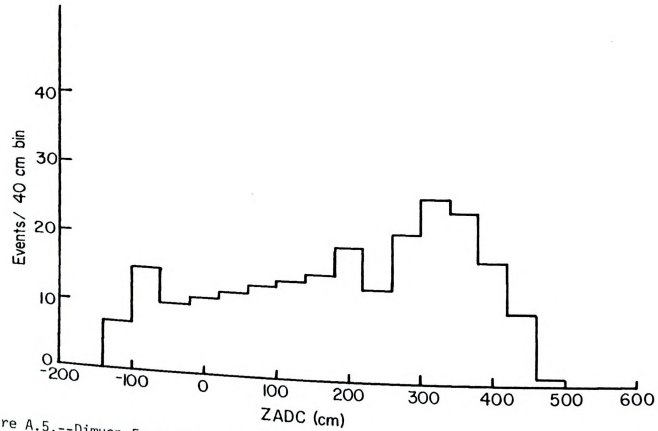

Figure A.5.--Dimuon Event Vertex Positions from the Calorimeter (ZADC).

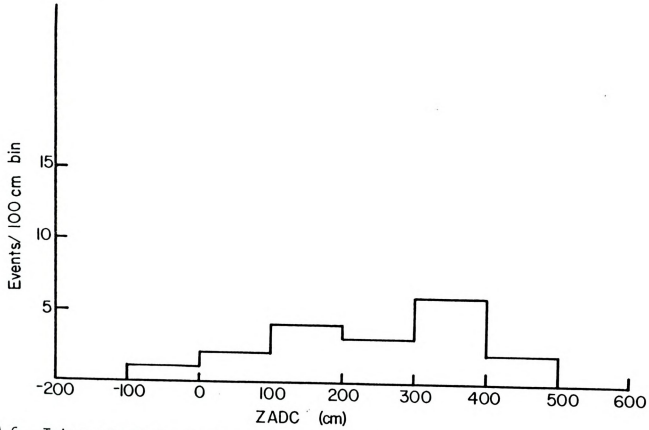

Figure A.6.--Trimuon Event Vertex Positions from the Calorimeter (ZADC).

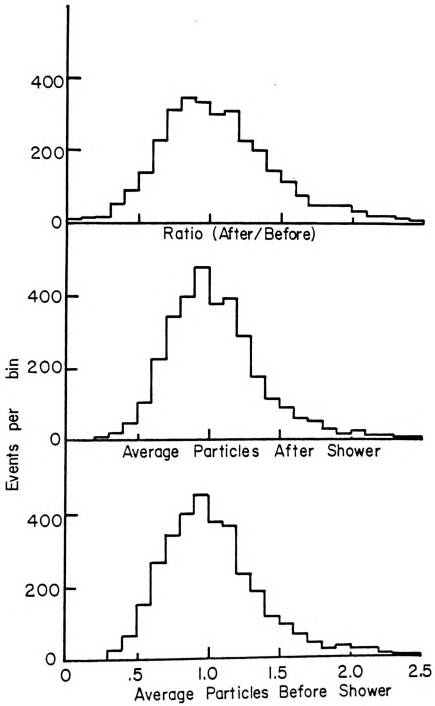

Figure A.7.--Average Number Particles Before and After the Vertex for Single Muon Events.

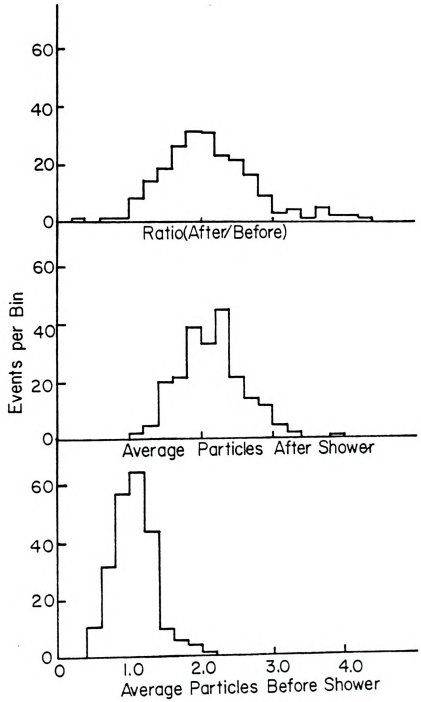

Figure A.8.--Average Number Particles Before and After the Vertex for Dimuon Events.

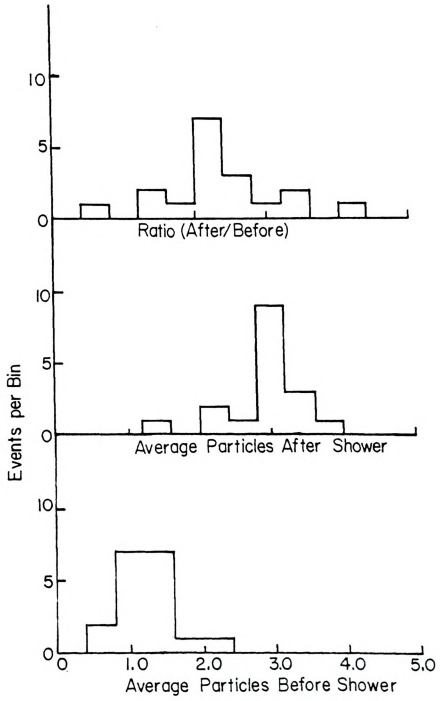

Figure A.9.--Average Number Particles Before and After the Vertex for Trimuon Events.

The most difficult use of the calorimeter was the determination of missing energy for multimuon events. The ADC decoding, shower location and equivalent particle summing algorithms were the same as those used to analyze the hardron calibration data except that the particle sums were converted into energies from the fits of Table A.1. At that point in the analysis then, we had the incident muon energy at the front of the target, the hadron shower energy at the interaction point, and the final state muon energies from the momentum fitting routines evaluated at the end of the target. A determination of missing energy required that energy loss corrections be made to estimate all muon energies at the interaction point. This was done using a polynomial fit to published energy loss tables for muons in iron.[8] Note that this was only an average correction which ignored straggling effects.

To test the consistency of these energy measurements, the resulting hadron energy was compared with the difference between incident and scattered muon energies for single muon events where the missing energy should be zero. A histogram of this comparison is shown in Figure A.10, from which it is clear that the mean is zero within errors. Furthermore, the width of the distribution is only slightly larger than that expected from the measured calorimeter and spectrometer resolutions. Binning this missing energy versus hadron energy (Figure A.11) shows that the only problems were at very low hadron energy (due to noise and poor resolution) and very high hadron energy (due to leakage and calibration inaccuracies).

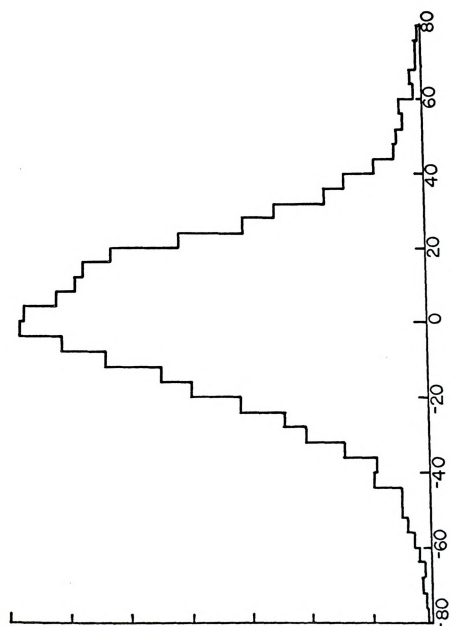

Figure A.10.--Missing Energy for Single Muon Events.

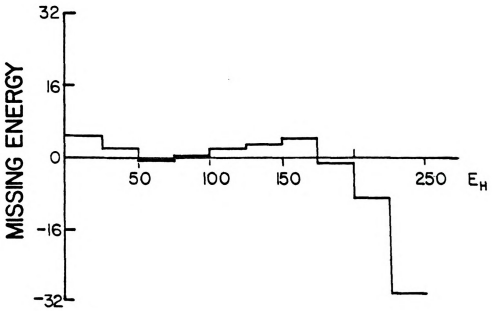

Figure A.11.--Average Missing Energy (per 25 GeV bin) versus Hadron Energy for Single Muon Events.

The otherwise good agreement over most of the energy range lends confidence in the energy calibration of both the calorimeter and the spectrometer.

For multimuons, missing energy was defined as the incident energy minus the energy of all final state muons minus the hadron energy, with all defined at the interaction point. Dimuon missing energy distributions are shown in Figures A.12 and A.13. The peak missing energy is clearly not zero, although the width is considerably larger than the distribution for single muons due to the generally poorer resolution of the extra muon. Furthermore, the missing energy also increases with the hadron energy, a characteristic feature of heavy hadron production and decay which has been shown to dominate the dimuon sample. Although the statistics are poor for the trimuon sample, the missing energy distribution shown in Figure A.14 is consistent with a mean of zero. This supports the hypothesis that these events tend to be largely due to trident and vector meson production.

In summary, the hadron calorimeter has contributed in a significant way to the identification and understanding of multimuon events. The missing energy distributions, in particular, tend to discriminate against some of the many possible explanations for these events. Although the construction and operation of hadron calorimeters is by no means trivial, the advantages for multimuon work are so convincing that all proposed muon and neutrino experiments will employ some form of calorimetry.

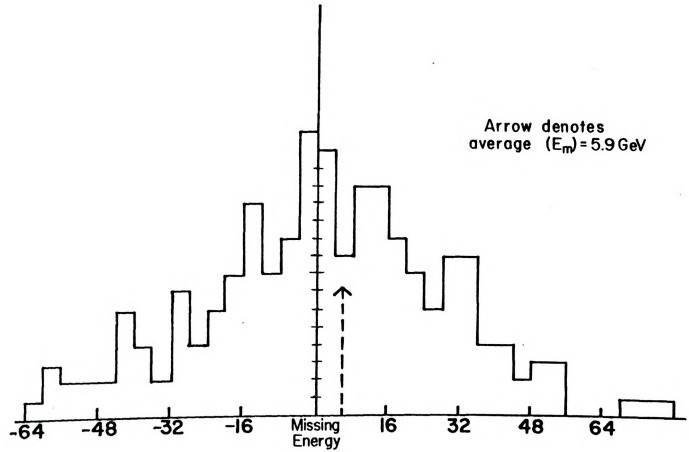

Figure A.12.--Missing Energy for Dimuon Events. (The vertical scale is number of events per 4 GeV bin with each division representing two events.)

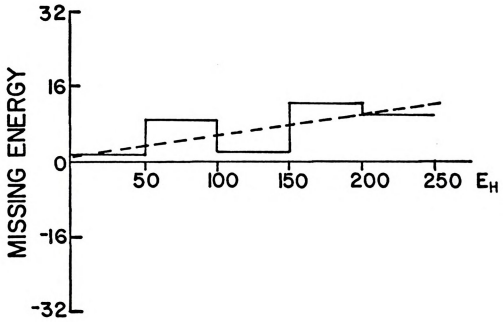

Figure A.13.--Average Missing Energy (per 50 GeV bin) versus Hadron Energy for Dimuon Events.

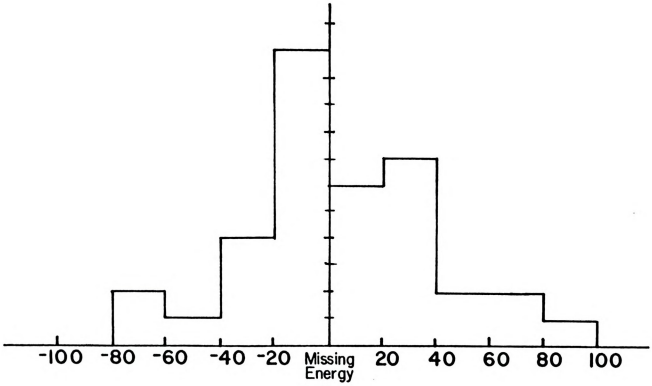

Figure A.14.--Missing Energy for Trimuon Events. (The vertical scale is number of events per 20 GeV bin with each division representing one event.)

APPENDIX B

TRACK RECONSTRUCTION AND FITTING ALGORITHMS

APPENDIX B

TRACK RECONSTRUCTION AND FITTING ALGORITHMS

B.1 Introduction

This appendix is devoted to a more thorough description of the algorithms used to reconstruct and fit muon tracks in the analysis program MULTIMU. Although developed specifically for the E319 apparatus, these methods are widely applicable to any magnetic spectrometer with toroidal symmetry about the beam axis.

B.1 Vertices

One of the most powerful means of rejecting halo muon and spuriously-matched tracks found in the spectrometer was to make cuts on the vertex position of the track with the beam. In MULTIMU the distance of closest approach of each line found at the front of the spectrometer to the beam track was calculated using the following method. Take any two non-parallel lines (shown in Figure B.1) which can be parametrized as

$$\vec{R}_i = \vec{r}_i + \hat{n}_i t_i$$

The unit vector

$$\hat{u} = \hat{n}_1 \times \hat{n}_2 / | \hat{n}_1 \times \hat{n}_2 |$$

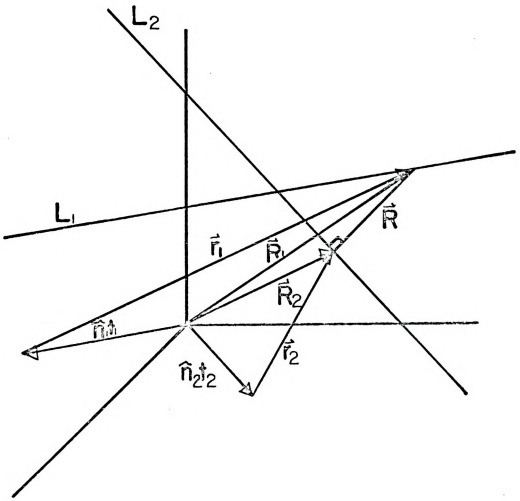

Figure B.1.--Vertex Algorithm Geometry and Conventions.

is then perpendicular to both lines and the distance between them is then

$$d = (\vec{R}_2 - \vec{R}_1) \cdot \hat{u}$$

This can be minimized in the standard way by taking derivatives of d with respect to each coordinate. But, for only two lines at minimum distance, the equations

$$(\vec{R}_2 - \vec{R}_1) \cdot \hat{n}_1 = 0 \qquad (\vec{R}_2 - \vec{R}_1) \cdot \hat{n}_2 = 0$$

allow an easy solution for t_1 and t_2. Since the matched lines in the E319 coordinate system are of the form

$$x = x_i + \alpha_i z \qquad y = y_i + \beta_i z \qquad z = t,$$

we then easily obtain the z position of the vertex (ZMIN). This is sufficient to make cuts which insure that the tracks really come from the general vicinity of the calorimeter shower (ZADC) in the target. Then, projecting the beam to (X1, Y1, ZMIN) and the line candidate to (X2, Y2, ZMIN), the quantity

$$DMIN = [(X2-X1)^2 + (Y2-Y1)^2]^{\frac{1}{2}}$$

allows a further cut on the track quality.

This method can be generalized to give the spatial position of the vertex for any number of lines by defining a point P = (X, Y, Z) in space. By drawing a vector $\vec{R}$ from P to line i, it is obvious that the perpendicular distance between P and the line is

$$d_i = |\vec{R} \times \hat{n}_i|.$$

The idea is then to solve for the point P which minimizes

$$D = \sum_i d_i^2$$

Since this becomes analytically unmanagable for more than a few lines, the calculation is most often done numerically.

B.3 Tracing Muon Trajectories in Magnetized Iron

The algorithm for tracing tracks through the toroidal spectrometer was originally developed for the E26 apparatus[1] and has required only minor modifications for E319. The basic approach was to treat each magnet as a set of discrete bend points for the track as shown in Figure B.2. Then the x coordinate of the track at the nth detector (z_n) can be written

$$x_n = x_o + \theta_o (z_n - z_o)$$

$$- \sum_{i=1}^{m} (\Delta x')_i (z_n - zm_i)$$

where (θ_o, x_o, z_o) = (Slope, intercept, z position) just before the first magnet and $\Delta x'$ = slope change at bend point zm_i. The equation for y_n is of exactly the same form due to the cylindrical symmetry of the apparatus. The slope changes can be derived from the Lorentz force equation:

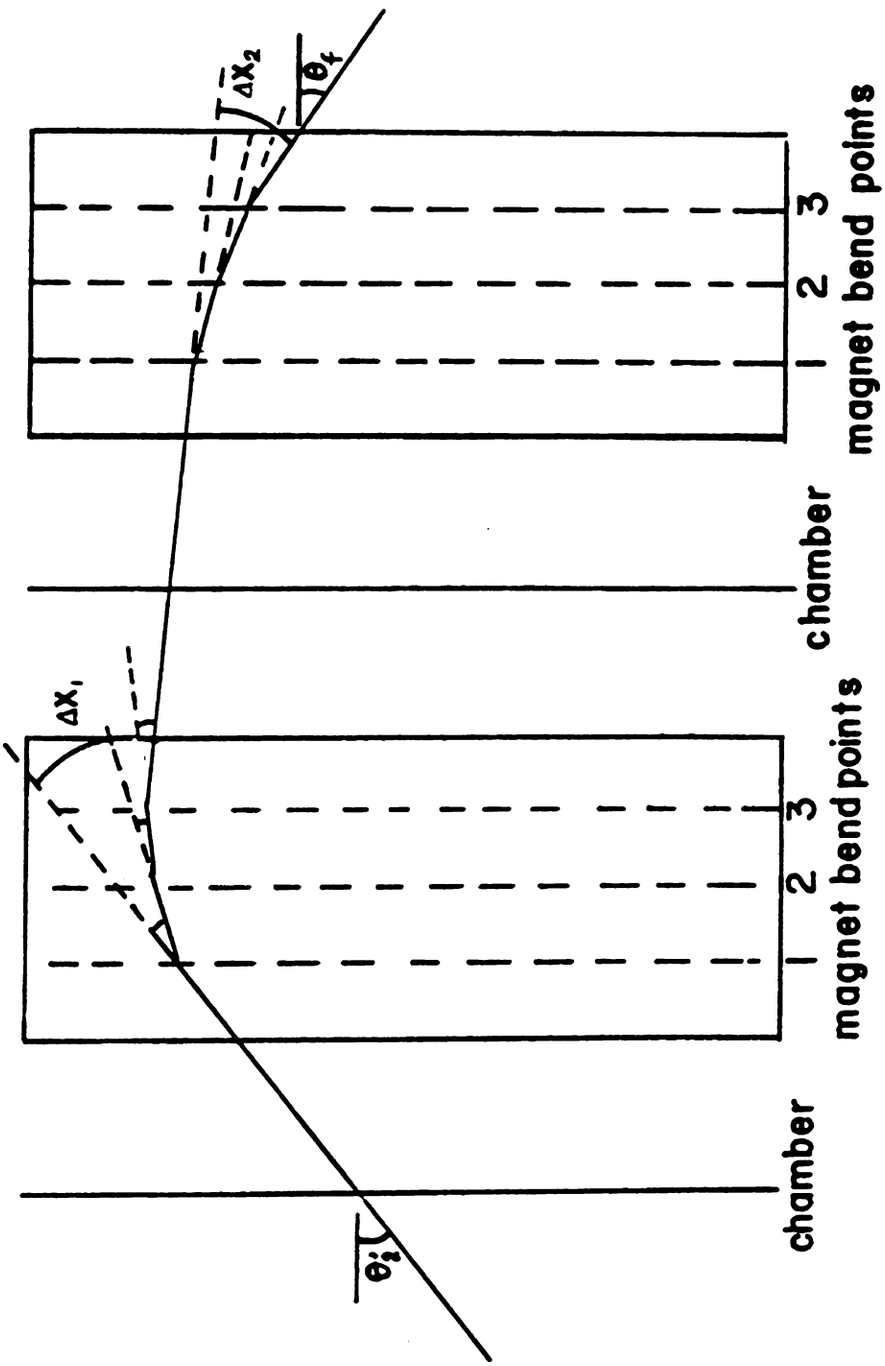

Figure B.2.--Geometry for Tracing Muons through Magnetized Iron.

$$\Delta x' = \frac{\Delta p_x}{p} = -kf(r)L\cos\phi \quad \Delta y' = \frac{\Delta p_y}{p} = -kf(r)L\sin\phi.$$

These complicated functions of k, r and ϕ can be expanded in a Taylor series and truncated at second order in k with little loss of accuracy. The resulting expression for the slope changes consists of a first order term, accounting for the bending due to a uniform magnetic field, and a second order term which contains the effects of field variation with radius and muon energy loss in the iron magnets. Of course, these approximations would be expected to break down at very low momenta (large k) or in regions of large field variation. They have proven quite adequate for most of the scattered muons in the E319 apparatus. Detailed comparisons of projected tracks versus actual spark coordinates have assured us that, excepting a region very near the hole in the magnets, tracks with momenta between 5 and 300 GeV are followed quite well.

The above algorithm can be reversed so as to give momentum estimates for a potential track by ignoring the small second order terms and forming a pseudo chi-squared equal to the sum of the squares of the actual sparks minum predicted positions. This can be minimized as a function of k, leading to a solution for the momentum p. Although this estimate is somewhat biased at the extremes of the momentum range, it has proven useful in finding tracks. The final momentum fitting uses a more sophisticated approach as described in Section B.5.

B.4 Spark Finding

As described in Chapter 3, track finding in MULTIMU begins by finding x and y lines at the front of the spectrometer, forming matched three-dimensional lines, and then projecting them into the magnetic region via the algorithm described in the previous section. However, there are several reasons why the sparks will not, in general, lie along the projected track. First, the finite wire spacing of the chambers causes a Gaussian extrapolation error about the projected track position downstream. This can be calculated by assuming the absence of the magnets so that the predicted position at any chamber z is

$$x_n = a\,(z_n - z_o) + b$$

with (a, b, z_o) being the (slope, intercept, z position) of the upstream track just before entering the spectrometer. The deviations due to extrapolation error can then be written

$$\Delta x_n = z_n \Delta a + \Delta b$$

with the slope and intercept changes related to the chamber resolution σ by:

$$\begin{bmatrix} (\Delta a)^2 & \Delta a \Delta b \\ \Delta a \Delta b & (\Delta b)^2 \end{bmatrix} = \sigma^2 \begin{bmatrix} 3 & -\sum_{i=1}^{m} z_i \\ -\sum_{i=1}^{m} z_i & \sum_{i=1}^{m} z_i^2 \end{bmatrix} \Bigg/ \begin{bmatrix} \text{Determinant} \\ \text{of the} \\ \text{above} \\ \text{matrix} \end{bmatrix}$$

Due to the cylindrical symmetry, the extrapolation error becomes a circular spark finding window about the projected track with radius

$$r_e = \Delta x_n.$$

A much more serious source of deviation is multiple scattering of the muons in the iron magnets. The problem here is that the magnetic field causes the positions at successive downstream chambers to be correlated with physical deviations like multiple scattering upsteam. This has the effect of offsetting the spark-finding window from the projected track position, as shown in Figure B.3. The resulting overall shape of the spark finding window, consisting of a set of circles of increasing radii and offsets, is that of an hourglass. The radii of the multiple scattering part of the window were derived from the equations for RMS angular deviation $\langle\theta\rangle$ and average linear deviation $\langle y\rangle = L\,\langle\theta\rangle/\sqrt{3}$ given in the particle data book.[2] From Figure B.4, it is clear that

$$r_x = \langle y\rangle + x_p = \langle\theta\rangle[L\sqrt{3} + 1]$$

and similarly for r_y. Defining

$$\Delta z = |z_n - z_m|, \quad \text{zeff} = L\,(1/\sqrt{3} - 1/2)$$

gives $r_x = \langle\theta\rangle\,[\text{zeff} + \Delta z]$

where $z_n = n^{th}$ spark chamber, $z_m = m^{th}$ magnet mid-point.

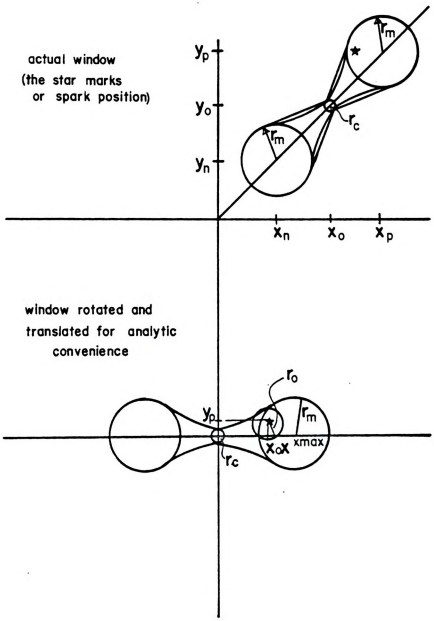

Figure B.3.--Definiton of the Hourglass Window for Track Finding.

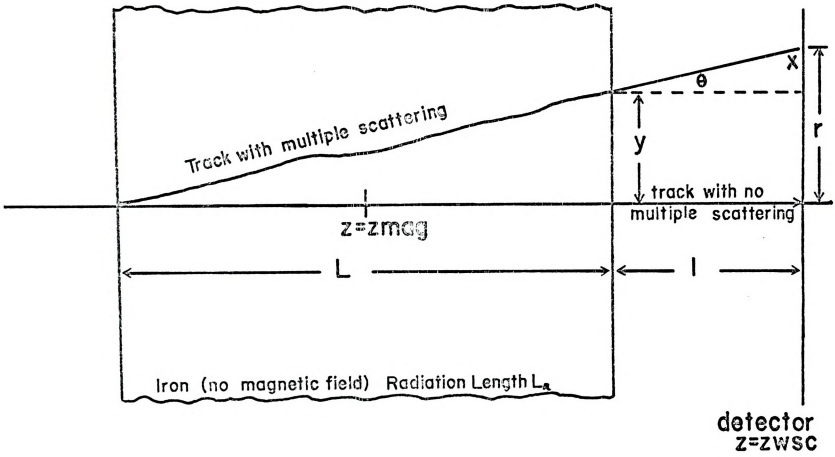

Figure B.4.--Geometry and Conventions for Calculating Multiple Scattering Effects in Iron.

Thus, the multiple scattering radius r_m at chamber n is

$$r_m = [r_x^2 + r_y^2]^{\frac{1}{2}} = \langle\theta\rangle[\sum_{i=1}^{n} (\Delta z_i + \text{zeff})^2]^{\frac{1}{2}}$$

The definition of the overall window, given the conventions used in Figure B.3 becomes:

$$r_o^2 = r_e^2 + r_m^2 (x/xmax)^2 = y_o^2 + (x-x_o)^2$$

where $x_{max}^2 = x_p^2 + y_p^2$

A spark is considered to be within the window if: (a) a real solution exists for x and (b) $-(x_{max} + r_m) \leq x \leq (x_{max} + r_m)$. The hourglass window has proven to be a very reliable and efficient algorithm for accepting only sparks consistent with real tracks and inhibiting the tendency to be pulled off by bad sparks.

Once sparks are found in at least two of the four views, they are matched to give true (x, y) coordinates with cuts made on the consistency of agreement between sparks found in x or y planes. This redundancy gives a final discrimination against the inclusion of accidental sparks on the track.

B.5 Momentum Fitting

Once the sparks on a muon track have been found, it is necessary to perform a global fit in order to determine the most likely values of momentum and upstream track parameters which would have given rise to those sparks. The results of this fit are then

used for all further kinematic calculations. The general strategy was mapped out in Chapter 3. Here I concentrate on the definition and minimization of the chi-squared function and specific improvements made to this algorithm for multimuon work.

In order to achieve the best fit, chi-squared had to be defined so as to account for correlations of multiple scattering and measurement errors between all of the chambers on the track. There was a natural distinction in the E319 apparatus between the front three chambers (labeled 8, 9, and 10), which were not within the magnetic part of the spectrometer, and the downstream seven chambers (labeled 1 through 7). Therefore, chi-squared (χ^2) was defined as

$$\chi^2 = \text{CHIF} + \text{CHIB}$$

where CHIF is the chi-squared of the upstream, and CHIB of the downstream portions of the track. The upstream chi-squared was defined by

$$\text{CHIF} = \sum_{k=8}^{10} \{[x_m - (\theta_x z_k + x_o)]^2 + [y_m - \theta_y z_k + y_o]^2\} / [\sigma_F^2 + \sigma_{ms}^2 k^2]$$

where (x_m, y_m) = measured spark coordinates at chamber k, $(\theta_x, \theta_y, x_o, y_o)$ = slopes and intercepts of the track exiting the target, σ_F = resolution of the upstream chamber k and σ_{ms} = error due to multiple scattering in the hadron shields at chamber k. The best fits were found with

$$\sigma_F = 0.2 \text{ cm and } \sigma_{ms} = \left\{ \begin{matrix} 3.6 \text{ cm for chamber 9} \\ 15.3 \text{ for chamber 8} \end{matrix} \right\}$$

The downstream chi squared is more complicated due to multiple scattering correlations:

$$CHIB = \sum_{i=1}^{7} \sum_{j=1}^{7} [x_m - x_p]_i \, y_{ij}^{-1} \, [y_m - y_p]_j$$

where y_{ij} is the matrix which correlates the positions at chambers i and j and (x_p, y_p) are the predicted positions from the algorithm described in Section B.2. The correlation matrix can be written

$$y_{ij} = \langle \theta_{ms}^2 \rangle \sum_{k=1}^{8} (z_i - zm_k)(z_j - zm_k) + \delta_{ij}\sigma^2$$

where zm_k is the z position of the kth magnet

σ is the resolution of the downstream chambers

$\langle \theta \rangle_{ms}$ is the RMS multiple scattering angle

neglecting the effect of energy loss.

This chi-squared is a function of five parameters:

$K = \frac{\alpha}{p}$, the inverse momentum

(θ_x, θ_y), the x and y slopes at the front of the spectrometer

(x_o, y_o), the x and y intercepts at the front of the spectrometer.

Miminizing χ^2 as a function of these five quantities will return their best fit values. This was done by expanding analytically in a Taylor series, keeping terms only through second order in k, and then differentiating with respect to each of the parameters twice to obtain the direction the parameters would have to be varied to reach minimum χ^2. Symbolically, this can be written

$$(xx)_i = \sum_{j=1}^{5} (zx)_{ij} \, (AP)_j$$

where xx = partial derivatives of χ^2

zx = matrix of second partials with respect to the 5 parameters

AP = variations in the five parameters.

We then solve for the variations

$$(AP)_i = \sum_{j=1}^{5} (zx)^{-1}_{ij} \, (xx)_j .$$

This requires the inversion of the 5 x 5 zx matrix, for which the CERN library routine SPXINV[3] was used. The procedure was numerically iterated until $\Delta k/k \leq 1\%$. We have verified that this actually does converge by plotting the χ^2curve for all different types of tracks.

Although the general form of this fitting procedure has supplied by the E26 callaboration (as described in their status report),[4] we have made several improvements. These include:

a. The development of a procedure to pull bad sparks from a track and refit it. (This was essential for the relatively high momentum leading particles of multimuons);

b. The requirement that the tracing routines consider each magnet as three bend points, instead of just one, which greatly improves the fits for low energy muons;

c. Minor corrections were made to the actual coding which was somewhat incorrect at the extremes of the momentum range.

These changes have significantly improved the performance of the fitting procedure, especially for the typical multimuon event with a high-energy, low-angle leading muon and a low-energy, wide-angle produced muon. Furthermore, this has allowed an extension of the kinematic range available to single muon analysis as well.

APPENDIX C

MONTE CARLO ALGORITHMS

APPENDIX C

MONTE CARLO ALGORITHMS

C.1 Introduction

This appendix describes a few useful techniques employed in the E319 Monte Carlo calculations to simulate the following physical processes: (a) muon energy loss; (b) multiple Coulomb scattering; (c) curvature of muons in the magnetic spectrometer; and (d) form factors used for coherent scattering process, such as the Bethe-Heitler trident diagrams. This information is applicable to virtually any experiment which attempts to simulate muon kinematics.

C.2 Muon Energy Loss

There are four principal mechanisms for energy loss by charged particles in matter: (a) ionization, or the interaction with atomic electrons; (b) bremsstrahlung, the radiation of real photons in the atomic or nuclear fields; (c) electron pair production; and (d) interactions with the nucleus or individual nucleons. These are given in the order of their importance for the average energy loss by muons in our energy range. However, none of these mechanisms gives a strictly symmetrical distribution of energy losses because they all result from statistically independent scattering events. Instead, each has the usual Landau tails, especially on the large energy loss end of the distribution. This "straggling" is particularly important

for bremsstrahlung because its differential cross section is inversely proportional to energy loss E. It is less relevant but still not negligible for ionization, which goes like $1/E^2$. At our energies, straggling can be ignored for pair production, since the cross section varies as $1/E^3$ and the overall probability is low. Even the average energy loss from nuclear interactions is negligible at energies less than about 300 GeV, so we ignored this mechanism completely. Thus, our energy loss simulation attempted to model the full distribution for ionization and bremsstrahlung and included the average energy loss from pair production.

The average ionization energy loss for particles heavier than the electron is given by the well-known Bethe-Bloch equation,[1] which has been modified to account for several small atomic effects. Ionization straggling was first studied by Landau[2] and later by Symon.[3] Their results are summarized by Rossi,[4] whose equations and graphs we have used. The idea is to define a most-probable energy loss from the Bethe-Bloch equation, and then use the distribution functions plotted in Figure 2.7.2 of Rossi. We fit these functions using a central Gaussian section and a combination of exponential and polynomial tails and used this as the throwing function for the Monte Carlo. Tables C.1 and C.2 compare our simulation with the calculations of Theriot.[5] Clearly, the average energy loss is well reproduced, although he gives no information on straggling.

Muon bremsstrahlung has already been discussed as the first part of the pseudotrident multimuon process. The principle reference is the very complete work of Tsai,[6] with additional help from

TABLE C.1.--Comparison of Muon Energy Loss Monte Carlo Calculations

Incident Energy (GeV)	Thickness of Target		Total Energy Loss (GeV)		Difference (%)
	(cm)	(g/cm^2)	"Theriot"	E319	
5	5	28.8	.054	.057	6.1
	100	575.9	1.071	1.142	6.6
	700	4031.3	>5.0	>5.0	---
10	100	575.9	1.135	1.189	4.8
20	100	575.9	1.209	1.259	4.1
50	100	575.9	1.348	1.380	2.4
100	100	575.9	1.555	1.580	1.6
150	5	28.8	.088	.085	-3.1
	100	575.9	1.751	1.776	1.4
	700	4031.3	12.255	12.390	1.1
270	5	28.8	.111	.110	-1.2
	100	575.9	2.229	2.233	0.2
	700	4031.3	15.601	15.492	-0.7

TABLE C.2.--Contributions of Individual Processes to Muon Energy Loss Calculations

Incident Energy (GeV)	Thickness of Target (cm)	(g/cm^2)	Percent of Total Due to: Ioniz.	Brems.	Pair Prod.	Nuclear
5	5	28.8	98.9	0.5	0.5	<0.1
	100	575.9	99.0	0.5	0.4	<0.1
	700	4031.3	99.0	0.5	0.4	<0.1
10	100	575.9	97.9	0.9	0.9	<0.3
20	100	575.9	95.8	1.8	2.2	<0.2
50	100	575.9	89.3	4.8	5.5	<0.3
100	100	575.9	79.6	9.3	10.2	0.9
150	5	28.8	71.8	13.0	14.0	1.2
	100	575.9	71.7	13.1	14.0	1.2
	700	4031.3	71.7	13.1	14.0	1.2
270	5	28.8	57.6	20.2	20.6	1.6
	100	575.9	57.4	20.2	20.6	1.8
	700	4031.3	57.4	20.2	20.6	1.8

Rossi and Tannenbaum.[7] If a muon with energy E radiates a photon of energy k, equation III.82 of Tsai supplies the differential cross section as a function of the fractional photon energy y = k/E:

$$\frac{d\sigma}{dy} = \frac{\alpha^3}{m^2 y} F(y)$$

where F(y) is a very complicated function involving details of the atomic properties of the target material. To obtain a total cross section, we cut off the spectrum at:

$$y_{max} = 1 - \frac{M_\mu}{E} \quad \text{and} \quad y_{min} = 1 \times 10^{-4}$$

to keep photon energies within reasonable bounds and prevent the cross section from diverging. Then, the probability of bremsstrahlung is the product of the total cross section and luminosity. The final algorithm to calculate energy loss from this process uses a polynomial fit to the energy dependence of the total cross section to determine when a non-zero energy loss should be generated (around 2% of the time). Then y is thrown by the differential cross section to yield the energy loss y · E. Again, the average energy loss is shown in Tables C.1 and C.2. At the lowest energies, the differences from Theriot grow as large as 20%, but the total contribution of bremsstrahlung to energy loss is still quite small.

The main features of electron pair production by high energy muons are well summarized by Tannenbaum,[7] who gives approximate forms of the cross section and discusses the similarity with bremsstrahlung.

However, we have used more recent formulae of Joseph[8] and Richard-Serre[9] to actually calculate the average energy loss for each energy. From Tables C.1 and C.2, it is obvious that Theriot has done the same. The overall energy loss we obtain agrees with his results to within 10% at all energies, with the largest difference being at very low energies and distances.

C.3 Multiple Coulomb Scattering

Multiple scattering refers to the net change of direction of charged particles due to many small-angle scatters from the Coulomb fields of nuclear matter. The phenomenon has been thoroughly described in the literature by Moliere[10] and Scott.[11] The resulting angular distribution is approximately Gaussian, but with tails due to straggling just as in the energy loss process. These represent less than 10% of the distribution for muons in our experiment and are ignored in the Monte Carlo. The average angular deflection is given by:[12]

$$\overline{\theta^2} = \frac{(.015\ \text{GeV/C})^2}{p^2\ \beta^2} \qquad \frac{L}{L_R} = \frac{\sigma_{ms}^2}{2}$$

where σ_{ms} is then taken to be the standard deviation of a Gaussian throwing distribution:

$$p(\theta) = \exp\left(\frac{-\theta^2}{\sigma_{ms}^2}\right)$$

One actually generates an angle θ in the standard manner:

$$\theta = (-\ln (\text{random \#}) \times \sigma_{ms}^{2})^{\frac{1}{2}}$$

within the interval from 0 to 1. This angle is then used to alter the direction cosines and the muon is traced on from there.

C.4 Curvature of Muons in the Magnetic Field

Due to the small step length (5 cm) used for tracing muons through the simulated E319 apparatus, and the desire to replace detailed reconstruction algorithms with simple resolution tables, the method for propagating muons through the magnetic spectrometer is simple. Ignoring small second order terms from field derivatives and energy loss, and using the standard formulae for the radius of curvature of a particle of momentum p in a locally constant magnetic field B yields the change in unit momentum vector:

$$\frac{\vec{dp}}{p} = R\,(\vec{dx} \times \vec{B})$$

Here $\vec{dx}$ represents the step vector and $\vec{B}$ the magnetic field direction. Since the field for E319 was azimuthally constant,

$$B_x = B\cos\phi \qquad B_y = B\sin\phi \qquad B_z = 0$$

Thus the direction cosines change in each step D by:

$$\Delta DCX = -\,RD\,\sin\phi\ DCZ$$

$$\Delta DCY = RD\,\cos\phi\ \ DCZ$$

$$\Delta DCZ = RD\,(\sin\phi\ DCX - \cos\phi\ DCY)$$

where DCX, DCY, and DCZ are the old direction cosines. The results are then renormalized to unity for the next step. Note that the apparatus resolution was then easily included by simply "wobbling" the generated kinematics, after each track is traced, by the actual measured widths of the momentum, angle and position distributions.

C.5 Nuclear Form Factors

In our consideration of elastic Bethe-Heitler tridents, we used form factors $F(q^2)$ to describe the complex charge structure of the nucleus as a whole. Recall that for a spherically symmetric charge density $\rho(r)$, one has:[13]

$$F(q^2) = \frac{4\pi}{q}\int_0^\infty \rho\,(r)\,\sin(qr)\,dr$$

where r is the radius, and q the momentum transfer to the nucleus. In the early days of electron scattering, the elastic form factors of nuclei were studied in detail by Hofstadter and many others.[14] The form factor of the proton was fit by the dipole form

$$F(q^2) = \left(1 + \frac{q^2}{.71 \times 10^6}\right)^{-2}$$

corresponding to an exponential charge density. Although similar form factors have been considered for heavier nuclei, better fits are obtained by using the Fermi charge distribution[15]

$$\rho(r) = \frac{\rho_o}{1 + \exp\left(\frac{r-c}{z}\right)}$$

where $c = \frac{1}{2}$ density radius $= 1.07A^{1/3}$

b = skin thickness$=4 \ln(3z) \simeq 2.4$ fm

a = RMS radius $= .82A^{1/3} + .58$

An approximate expression for the Fourier transform gives:[16]

$$F(q^2) = \frac{\exp\left(\frac{-b^2}{6}q^2\right)}{1 + \frac{c^2}{6}q^2}$$

where for iron $\frac{c^2}{6} = 71.6 \times 10^{-6} \frac{1}{\text{MeV}^2}$, $\frac{b^2}{6} = 24.6 \times 10^{-6} \frac{1}{\text{MeV}^2}$

This works well until the momentum transfer becomes so high that the individual nucleons are being explored. In that region one can revert to the form factors for the proton and neutron again. Thus, for coherent (Fe) tridents we have used the Fermi form factor, while for incoherent (p) tridents, we summed the dipole contributions from the 56 individual nucleons in the iron nucleus.

REFERENCES

REFERENCES--CHAPTER 1

[1]J. J. Thomson, Phil. Mag. 44, 312 (1897). Also see D. L. Anderson, The Discovery of the Electron (Van Nostrand, Princeton, New Jersey, 1964).

[2]C. D. Anderson, Phys. Rev. 43, 491 (1933).

[3]S. H. Neddermeyer and C. D. Anderson, Phys. Rev. 51, 884 (1937).

[4]W. Pauli in Collected Scientific Papers of Wolfgang Pauli (ed. R. Kronig and V. F. Weisskopf), pg. 1316.

[5]F. Reines and C. L. Cowan Jr., Phys. Rev. 113, 273 (1959).

[6]G. Danby et al., Phys. Rev. Letters 9, 36 (1962).

[7]M. L. Perl et al., Phys. Rev. Letters 35, 1489 (1975).

[8]See eg. D. I. Meyer et al., Phys. Letters 70B, 469 (1977); J. D. Bjorken and C. H. Llewellyn Smith, Phys. Rev. D7, 887 (1973); H. Georgi and S. L. Glashow, Phys. Rev. Letters 28, 1494 (1972).

[9]See eg. R. D. Feynman, Phys. Rev. Letters 23, 1415 (1969); J. D. Bjorken and E. A. Paschos, Phys. Rev. 185, 1975 (1969).

[10]M. Gell-Mann and Y. Ne'eman, The Eightfold Way (Benjamin Press, New York, 1964).

[11]J. E. Augustin et al., Phys Rev. Letters 33, 1406 (1974); J. J. Aubert et al., Phys. Rev. Letters 33, 1404 (1974); S. W. Herb et al., Phys. Rev. Letters 39, 252 (1977).

[12]See e.g., J. D. Jackson, Classical Electrodynamics (J. Wiley, New York, 1962).

[13]See e.g., J. J. Sakurai, Advanced Quantum Mechanics (Addison-Wesley, Reading, Massachusetts, 1967).

[14]P.A.M. Dirac, Proc. Roy. Soc. (London) A117, 610 (1928).

[15]See Selected Papers on Quantum Electrodynamics (ed. J. Schwinger, Dover, New York, 1958).

[16]S. J. Brodsky and S. D. Drell, Ann. Rev. Nucl. Sci. 20, 147 (1970).

[17]See e.g., C. D. Ellis and W. A. Wooster, Proc. Roy. Soc. (London) A117, 109 (1927).

[18]E. Fermi, Z. Physik 88, 161 (1934).

[19]See H. Frauenfelder and E. M. Henley, Subatomic Physics (Prentice-Hall, New Jersey, 1974), section 11.11.

[20]See e.g., M.A.B. Be'g and A. Sirlin, Ann. Rev. Nucl. Sci. 24, 1 (1974).

[21]S. Weinberg, Phys. Rev. Letters 19, 1264 (1967); A. Salam, in Elementary Particle Theory (8th Nobel Symposium), ed. N. Svantholm (Almqvist and Wiksell, Stockholm, 1968).

[22]An excellent review can be found in B. W. Lee, Proc. of the XVI International Conf. on High Energy Physics, NAL, 1973.

[23]See e.g., D. M. Brink, Nuclear Forces (Pergamon, New York, 1965).

[24]Frauenfelder and Henley, ibid., Chapter 12.

[25]M. Gell-Mann, Phys. Letters 8, 214 (1964); G. Zweig, CERN Report 8182/Th. 401 (1964).

[26]See e.g., H. D. Politzer, Phys. Reports 14C, 129 (1974).

[27]See e.g., D. J. Gross and F. Wilczek, Phys. Rev. D8, 3633 (1973); A. J. Buras and K. J. F. Gaemers, Nucl. Phys. B132, 249 (1978).

[28]See e.g., M. Gluck and E. Reya, Phys. Letters 79B, 453 (1978).

[29]Two excellent summaries of electron scattering experiments are: Electron Scattering and Nuclear and Nucleon Structure (ed. R. Hofstadter, Benjamin Press, New York, 1963); and J. I. Friedmen and H. W. Kendall, Ann. Rev. Nucl. Sci. 22, 203 (1972).

[30]C. Chang et al., Phys. Rev. Letters 39, 519 (1977).

[31]A. Benvenuti et al., Phys. Rev. Letters 41, 725 and 1204 (1978).

[32]H. J. Bhabba, Proc. Roy. Soc. (London) A152 , 559 (1935); G. Racah, Nuovo Cimento 4, 66 (1936); H. A. Bethe and W. Heitler, Proc. Roy. Soc. (London) A146, 83 (1934).

[33]E. G. Johnson Jr., Phys Rev. 140B, 1005 (1965); J. D. Bjorken and M. C. Chen, Phys. Rev. 154, 1335 (1967); G. Reading Henry, Phys. Rev. 154, 1534 (1967); S. J. Brodsky and S. C. C. Ting, Phys. Rev. 145, 1018 (1966).

[34]M. J. Tannenbaum, Phys. Rev. 167, 1308 (1968).

[35]J. J. Russell et al., Phys. Rev. Letters 26, 46 (1971); J. LeBritton et al., preprint entitled Trimuon and Dimuon Events Produced by 10.5 GeV/c μ^- on Lead to be published in Phys. Rev. D in 1980.

[36]K. W. Chen, Michigan State University preprint MSU-CSL-33 (May 1976) entitled Dimuon and Trimuon Production in Deep Inelastic Muon Interactions at 150 GeV.

[37]Y. S. Tsai, Rev. Mod. Phys. 46, 815 (1974). Also see V. Ganapathi and J. Smith, Phys. Rev. D19, 801 (1979).

[38]V. Barger et al., Phys. Rev. D20, 630 (1979).

[39]C. H. Albright and R. E. Shrock, Phys. Rev. D19, 2575 (1979).

[40]F. Wilczek and A. Zee, Phys. Rev. Letters 38, 531 (1977).

[41]R. W. Brown et al., Phys. Rev. Letters 33, 1119 (1974).

[42]A. R. Clark et al., Phys. Rev. Letters 43, 187 (1979).

[43]K. W. Chen and A. Van Ginneken, Phys. Rev. Letters 40, 1417 (1978).

[44]L. N. Chang and J. N. Ng, Phys. Rev. D16, 3157 (1977); C. H. Lai, FNAL PUB-78/18-THY.

[1]C. Chang, Ph.D. Thesis, Michigan State University (1975), unpublished; S. Herb, Ph.D. Thesis, Cornell University (1975), unpublished; Y. Watanabe, Ph.D. Thesis, Cornell University (1975), unpublished.

[2]Proc. Calorimeter Workshop, FNAL, Batavia, Illinois, 1975, (ed. M. Atac).

[3]V. K. Bharadwaj, Ph.D. Thesis, Oxford University (1977), unpublished; S. Pordes, Ph.D. Thesis, Harvard University (1976), unpublished.

[4]Multiwire Proportional Chambers (ed. W. M. Evans, Rutherford High Energy Lab, 1972).

[5]O. C. Allkofer, Spark Chambers (Verlag Karl Thiemig KG, Müchen, 1969).

[6]G. Giannelli et al., Nucl. Instr. Methods 47, 151 (1967).

[7]Fermilab proposals E203 and E391 and CERN SPS proposals NA2 and NA4.

[8]R. Ball, Ph.D. Thesis, Michigan State University (1979), unpublished.

[9]Fermilab Technical Memo TM-429 (2252).

[10]CERN Report CERN/SPSC/74-12 (5.2.1974).

[11]T. B. W. Kirk, private communication.

REFERENCES--CHAPTER 3

[1]Fermilab Proposal E319 and Agreement with Fermilab.

[2]CERN Computer 6000 Series Program Library, M420, 15.11.1971.

[3]E26 Status Report to Fermilab, June 1974.

[4]R. Ball, Ph.D. Thesis, Michigan State University (1979), unpublished.

[5]C. Chang, Ph.D. Thesis, Michigan State University (1975), unpublished; P. F. Schewe, Ph.D. Thesis, Michigan State University (1978), unpublished.

REFERENCES--CHAPTER 4

[1] E. D. Cashwell and C. J. Everett, Monte Carlo Methods (Pergamon Press, 1959).

[2] W. Y. Keung, private communication.

[3] S. J. Brodsky and S. C. C. Ting, unpublished.

[4] M. Tannenbaum, Phys. Rev. 167, 1308 (1968).

[5] V. Barger et al., Phys. Rev. D20, 630 (1979).

[6] Fermilab report FN-250 (1100).

[7] A. Van Ginneken, private communication.

[8] K. W. Chen and A. Van Ginneken, Phys. Rev. Letters 40, 1417 (1978).

[9] W. Bacino et al., Phys. Rev. Letters 43, 414 (1979).

[10] V. Barger et al., Charm Muoproduction with a Small-Angle Veto Univ. of Wisconsin Preprint COO-881-100, to be published in Phys. Rev. D in 1980.

REFERENCES--CHAPTER 5

[1]K. W. Chen and A. Van Ginneken, Phys. Rev. Letters 40, 1417 (1978).

[2]D. Bauer et al., Phys. Rev. Letters 43, 1551 (1979).

[3]C. H. Albright and R. E. Shrock, Phys. Rev. D19, 2575 (1979).

[4]Fermilab proposals E203 and E391.

[5]C. H. Albright and J. Smith, Fermilab-PUB-78/92-THY, Nov. 1978.

[6]D. I. Meyer et al., Phys. Letters 70B, 469 (1977).

[7]CERN SPS Proposals NA2 and NA4.

[8]K. J. Anderson et al., Phys. Rev. Letters 42, 944 (1979).

[9]A. R. Clark et al., Phys. Rev. Letters 43, 187 (1979).

[10]V. Barger et al., Univ. of Wisconsin Preprint COO-881-100 entitled Charm Muoproduction with a Small-Angle Veto to be published in Phys. Rev. D in 1980.

[11]J. J. Russell et al., Phys. Rev. Letters 26, 46 (1971); J. LeBritton et al., preprint entitled Trimuon and Dimuon Events Produced by 10.5 GeV/c μ^- on Lead to be published in Phys. Rev. D in 1980.

[12]V. Barger et al., Phys. Rev D19, 92 (1979).

REFERENCES--APPENDIX A

[1]See e.g., W. K. H. Schmidt et al., Phys. Rev. 184, 1279 (1969).

[2]Proc. Calorimeter Workshop, FNAL, Batavia, Illinois, 1975 (ed. M. Atac).

[3]See e.g., B. C. Barish et al., Nucl. Instr. Methods 130, 49 (1975).

[4]C. R. Kerns, Proc. Calorimeter Workship, ibid., p. 143.

[5]Private communication with members of Fermilab experiment E398.

[6]M. Holder et al., Nucl. Instr. Methods 151, 69 (1978).

[7]T. A. Gabriel and J. D. Amburgey, ORNL/TM-5615.

[8]C. Richard-Serre, CERN Report 71-18, 23 Sept., 1971.

REFERENCES--APPENDIX B

[1]Y. Watanabe, Ph.D. Thesis, Cornell Univ.,(1975), unpublished.

[2]Review of Particle Properties, Particle Data Group, Phys. Letters 75B, No. 1, April 1978, pg. 28.

[3]CERN Computer 6000 Series Program Library, F106, 1.3.1968.

[4]E26 Status Report to Fermilab, June 1974.

REFERENCES--APPENDIX C

[1]R. M. Sternheimer, Methods of Experimental Physics Vol. 5: Nuclear Physics (ed. L. Yuan and C. Wu, Academic Press, New York, 1961), Chapter 1.

[2]L. D. Landau, Journal of Physics U.S.S.R. 8, 201 (1949).

[3]K. R. Symon, Ph.D. Thesis, Harvard Univ. (1948). Also see R. M. Sternheimer, Phys. Rev. 91, 256 (1953) and Phys. Rev. 103, 511 (1956).

[4]B. Rossi, High Energy Particles (Prentice-Hall, New Jersey, 1952), Chapter 2.

[5]D. Theriot, NAL report TM-229, 1970.

[6]Y. S. Tsai, Rev. Mod. Phys. 46, 815 (1974).

[7]M. Tannenbaum, 1970 Summer Study, NAL, Batavia, Illinois, pg. 231.

[8]P. M. Joseph, Nucl. Instr. Methods 75, 13 (1969).

[9]C. Richard-Serre, CERN Report 71-18, Sept. 1971.

[10]C. Z. Moliere, Z. Physik 156, 318 (1959).

[11]W. T. Scott, Rev. Mod. Phys. 35, 231 (1963).

[12]Review of Particle Properties, Particle Data Group, Phys. Letters 75B, No. 1, April 1978, pg. 28.

[13]H. Frauenfelder and E. M. Henley, Subatomic Physics (Prentice-Hall, New Jersey, 1974), Section 6.4.

[14]R. Hofstadfer, Electron Scattering and Nuclear Structure, Rev. Mod. Phys. 28, 214 (1956); Electron Scattering and Nuclear and Nucleon Structure (ed. R. Hofstadfer, Benjamin Press, New York, 1963).

[15]R. C. Herman and R. Hofstadter, High Energy Electron Scattering Tables (Stanford Univ. Press, Stanford, California, 1960).

[16]Stein et al., SLAC-PUB-1528, Jan. 1975.